Nano Today 38 (2021) 101201

Contents lists available at ScienceDirect

Nano Today

journal homepage: www.elsevier.com/locate/nanotoday

Review

Tailoring nanostructured transition metal phosphides for high-performance hybrid supercapacitors

Quan Zong[a,b], Chaofeng Liu[b], Hui Yang[a], Qilong Zhang[a,*], Guozhong Cao[b,*]

[a] School of Materials Science and Engineering, State Key Lab Silicon Mat, Zhejiang University, Hangzhou 310027, PR China
[b] Department of Materials Science and Engineering, University of Washington, Seattle, WA, 98195, USA

ARTICLE INFO

Article history:
Received 14 October 2020
Received in revised form 17 April 2021
Accepted 16 May 2021
Available online 28 May 2021

Keywords:
Transition metal phosphides
Hybrid supercapacitors
Electrochemical properties
Nanostructures

ABSTRACT

Supercapacitors (SCs) have been gaining a great deal of interest as the appealing energy storage devices because of the outstanding power density and ultralong cycling features. Electrode materials as the active energy reservoir store the electrons and/or ions in the electrochemical process, determining the performance of the devices. Being the battery-type materials, transition metal phosphides (TMPs) have been studied extensively as high energy-density electrode materials in recent years, owing to their high electronic conductivities, and large theoretical capacity as well as tunable surface properties. However, TMPs electrode materials often suffer from sluggish reaction kinetics and volumetric expansion, resulting in inferior rate capability and cycling stability. In this review, basic reaction mechanisms of TMPs electrodes were first clarified. We reviewed the latest progress in tailoring the chemical composition and crystal and nanostructures of TMPs to attain desired and enhanced electrochemical properties as electrodes in hybrid capacitors. We discussed the design and various strategies for synthesis of various TMPs with improved electrochemical and transport properties. Much efforts and progresses have been made recently in designing and optimizing various synthesis processes, controlled elemental doping, fine tuning the chemical composition and nanostructures, and exploring composite materials.

Contents

---

* Corresponding authors.
E-mail addresses: mse237@zju.edu.cn (Q. Zhang), gzcao@uw.edu (G. Cao).

https://doi.org/10.1016/j.nantod.2021.101201

Introduction

Energy has played an irreplaceable role in the modern human society, pervasive in all aspects of our daily life and often being a bottleneck for many emerging technologies. The consumption of fossil fuel has caused increasingly serious environmental problems and the non-renewable attributes of fossil fuels endanger the sustainable development of the world [1–5]. To address these challenges, the development of clean energy technologies, such as harvesting solar, wind, and tidal energy, becomes an imperative task [6–8]. The intermittent characters of those renewable energy require the energy storage systems. Electrochemical energy storage devices, including rechargeable batteries [9–11] and supercapacitors (SCs) [12,13], are among the most widely studied and used in consumer electronics, electric vehicles, and potentially in smart grids. As compared in Fig. 1, rechargeable batteries working through redox reactions in the electrodes offer high energy density because of their large operating voltages and large capacities, but their power density is often restricted by mass diffusion kinetics [14]. While the conventional dielectric capacitors rely on the rapid charge separation and recombination at the interfaces of the dielectric materials and the metallic electrodes, presenting a low energy density but ultrahigh power output [15,16]. SCs bridge the gap between the batteries and conventional capacitors because of the exploration and introduction of the novel electrodes materials to improve both energy density and power density in the systems [17–20].

According to the charge storage mechanism of the electroactive materials, SCs can be divided into three categories: electric double-layer capacitors (EDLCs) [21,22], pseudo-capacitors [23,24], and hybrid supercapacitors (HSCs) [25,26]. The charge storage mechanisms, typical electrode materials and corresponding cyclic voltammetry (CV) plots are summarized in Fig. 2 [27–29]. EDLCs are based on the physical adsorption/desorption of ions in electrolytes at the electrode/electrolyte interfaces without the Faradaic process [30]. The discharge process is often finished in a very short period (less than 10 s), indicating the ultrahigh power density. The CV curve of EDLCs exhibits a rectangular shape. The capacitance of ELDCs can be calculated according to the following equation: $C = \varepsilon_r \varepsilon_0 A/d$, where ε_r is the electrolyte dielectric constant, ε_0 is the dielectric constant of the vacuum, A is the effective surface area, and d is the charge separation distance [31]. The specific surface areas and surface properties of electrode materials have crucial effects on the specific capacitance of EDLCs.

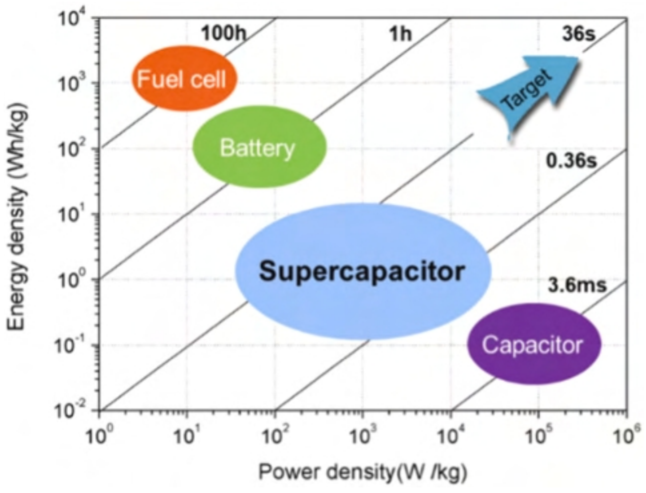

Fig. 1. Ragone plot of various energy storage devices. Batteries working through redox reactions in the electrodes present high energy density, while traditional capacitors exhibit ultrahigh power density. SCs bridges the gap between the batteries and conventional capacitors.

Pseudo-capacitors store charges by fast and reversible faradic reactions on the surface or near-surface of the electroactive materials [32]. The specific capacitance and energy density of pseudo-capacitors can be increased compared to conventional EDLCs. The pseudo-capacitive materials are usually divided into three types according to Faradaic mechanisms: underpotential deposition, surface redox pseudo-capacitance and intercalation pseudo-capacitance [33]. Underpotential deposition means a phenomenon of electro-deposition of a metal cation at a potential less negative than redox potential, which is due to the strong interaction between metal and substrate, such as Pd^{2+} on Au [34]. The working potential is very narrow because it must be below the cation redox potential. Surface redox pseudo-capacitance stores charges through faradaic redox reactions occurring on the surface of electrode materials, such as RuO_2, MnO_2, PANI and PPy [35–37]. The CV curve is a rectangular shape, similar to that of EDLCs. Intercalation pseudo-capacitive process involves reversible insertion/extraction of electrolyte cations into the structure of electrode materials rather than on the surface without any phase transition, such as V_2O_5 and Nb_2O_5 [38,39]. The CV curves exhibit redox peaks, but the kinetics is mainly controlled by the capacitive process. To clarify the electrochemical kinetics of these electrodes, low scan rate ($<1\ \text{mV s}^{-1}$) CV plots should be measured and investigated. The peak currents (i_p) and scan rates (v) can be fitted in the Eqs. (1) and (2) as follows [28,40,41]:

$$i_p = av^b \tag{1}$$

$$\log(i_p) = b\log(v) + \log(a) \tag{2}$$

where a and b are adjustable parameters. The b-value can be obtained from the slope of the plot of log (i_p) vs. log (v). To be more specific, a b-value of 0.5 indicates that the electrochemical process is dominated by the ion diffusion process while $b = 1$ represents a capacitive-controlled process [42,43]. The b-value of ~1 can be calculated from these three types of pseudo-capacitive materials [44].

HSCs are simply a mixture of half battery and half supercapacitor assembled by one capacitor-type electrode for high power density and long cycling lifespan and one battery-type electrode for high energy density [44–48]. Benefit from the utilization of the potential gap between two electrodes, the operating potential window of HSCs can be enlarged, resulting in high energy density compared to EDLCs and pseudo-capacitors as it is determined by the equation: $E = 1/2CV^2$ [49]. The driving force towards the development of HSCs

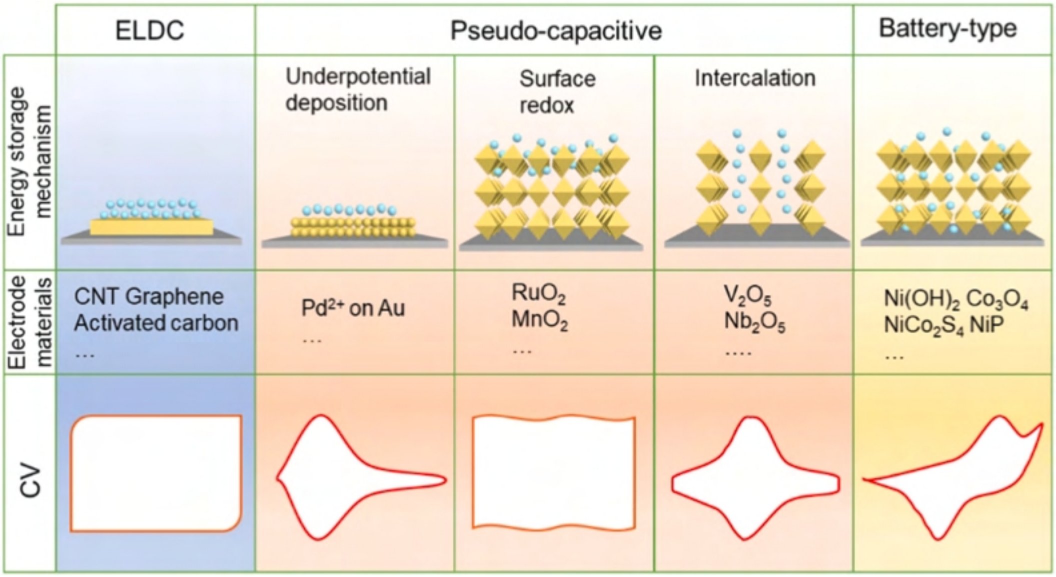

Fig. 2. Schematic illustration of the charge storage mechanism of three types of SCs, typical electroactive materials and corresponding CV curves.

is achieving excellent energy density, long cycling stability, low cost and good security. It is essential to match the mass ratio of positive and negative electrodes to utilize the electrochemical performance when assembling the device, in addition to the consideration of the nature of electrode materials playing a desirable roles on the electrochemical performances of HSCs [50]. The materials used as capacitor-type electrodes are activated carbon, graphene and metal oxides, etc [51]. The current battery-type materials include lithium intercalation compounds and transition metal compounds [52–54]. The CV plots of battery-type materials show apparent and intense oxidative and reductive peaks and the galvanostatic charge–discharge (GCD) curves demonstrate an obvious plateau during the charging and discharging process [55]. The *b*-value is often between 0.5 and 1 for battery-type materials, which means that the kinetics is a combination of capacitive behavior and diffusion-controlled progress accompanying phase-transformation during the charging/discharging process [56]. The ratios of capacitive ($k_1 v$) and diffusion-controlled ($k_2 v^{1/2}$) contribution can be quantitated by the current density (i) at a specific potential (V) and scan rate (v), based on the following equation [2,57,58]:

$$i\,(V) = k_1 v \; + \; k_2 v^{1/2} \tag{3}$$

The above equation can also be reformulated as:

$$i\,(V)/v^{1/2} = k_1 v^{1/2} \; + \; k_2 \tag{4}$$

It should be noted that the kinetics analysis for diffusion-controlled and surface capacitive charge storage can only provide a rough estimation [34].

Transition metal oxides (TMOs) have been investigated as electrode materials for supercapacitors due to their relatively high theoretical specific capacity [59–62]. However, the applications of TMOs are mainly restricted by their poor electrical conductivity and unsatisfactory rate capability because the band gap of TMOs implies the semiconductor properties [63,64]. To meet the requirements of practical applications, a large number of new materials, such as hydroxides, sulfides, selenides and phosphides, have been designed [65–67]. Transition metal phosphides (TMPs) comprised of the combination of phosphorus with one or several transition metal elements have been regarded as one of the most promising electrode materials for HSCs owing to the superior electrical conductivity, high electrochemical activity and metalloid properties [68,69]. Compared with TMOs, TMPs exhibit high specific capacity and excellent rate capability. The merits of phosphides derives from P that exhibits lower electronegativity (2.19 Pauling electronegativity of P to 3.44 Pauling electronegativity of O) and larger atomic radius of phosphorus (0.109 nm of P to 0.074 nm of O) in comparison with oxygen, exhibiting different physicochemical properties [70]. In addition, transition metal chalcogenides (TMCs, MX, X=S, Se) have also been extensively studied as electrodes in SCs. However, their electrochemical capacitance and energy density are humbled by their poor electrical conductivity due to large band gap, while transition metal phosphides are metallic with high electrical conductivity [71]. The bond length of metal-P is larger than those of metal-S and metal-Se due to the low electronegativity of P, contributing to high electrochemical activity [72]. Generally, TMPs materials possess desirable electrochemical properties as electrodes for SCs in comparison with their corresponding oxides, sulfides and selenides counterparts.

The nanostructured TMPs for batteries and SCs were presented in several reviews [69,70,73,74]. In 2015, Wang et al. discussed the relationship between nanostructures and electrochemical performances of metal phosphides-based materials for rechargeable batteries (lithium/sodium-ion batteries) and SCs, together with Li^+/Na^+ storage mechanisms [70]. In 2017, Li et al. summarized the synthesis methods of metal phosphides and phosphates as well as their electrodes for SCs [69]. Dinh et al. also overviewed the synthetic methodologies of metallic transition metal compounds including carbides, nitrides, phosphides, and borides as well as their applications in electrode materials and electrocatalysts in 2019 [73]. More recently, Li et al. briefly summarized the synthesis of metal phosphides and various nanostructures ranging from zero dimensions to three dimensions in rechargeable batteries [74]. However, comprehensive discussion on the impacts of various nanostructures, non-stoichiometric composition, and defects of TMPs on the redox reactions and transport properties for HSCs should be further discussed and elaborated. In this review, we focus on the most recent progress on the TMPs for HSCs with emphasis on the relationships between nanostructures, chemical composition, defects, electrochemical and transport properties as schematically illustrated in Fig. 3. We started with a brief overview of the basic characteristics of TMPs as electrodes for HSCs, and discussed the composition of TMPs studied for HSCs, followed by a detailed elaboration of nanostructures engineering including zero-, one-, two-, and

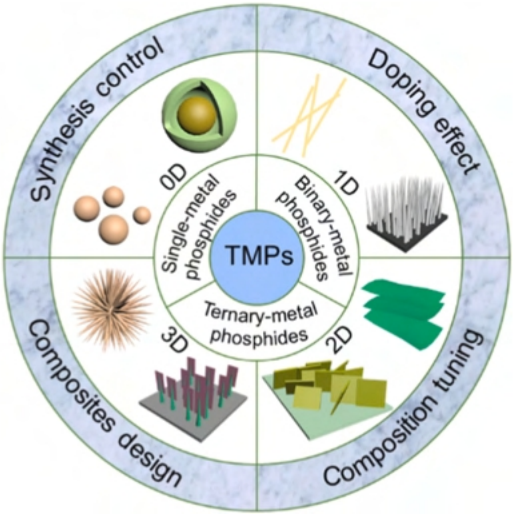

Fig. 3. Schematic illustration of the recent development of TMPs NAs materials such as various composition (single-metal, binary-metal, and ternary-metal phosphides), their dimensionalities (0D, 1D, 2D, and 3D), and strategies for the improvement of electrochemical properties including optimizing synthesis process, elemental doping, composition tuning and composites design.

three-dimensional TMPs synthesized by various synthesis methods. The challenges and prospects for further enhancing the electrochemical and transport properties of TMPs for better HSCs performance are discussed. This overview may offer some guidance for the design and engineering of TMPs and TMPs-based materials for HSCs.

Overview of electrode materials for SCs

Electrode materials for ELDCs and pseudo-capacitors

Carbonaceous materials, such as carbon nanotubes (CNTs), graphene and activated carbon, are often used as electrode materials for EDLCs because of their large specific surface areas [75]. However, due to the relatively low specific capacitance, the energy density of EDLCs based carbonaceous materials could only reach up to ~10 Wh kg^{-1} [30]. RuO_2 is the first reported as pseudo-capacitive materials and has been widely studied in the past several decades [35]. The theoretical specific capacitance of RuO_2 could reach up to more than 1450 F g^{-1}, but the high cost and the narrow voltage window hinder their wide applications [76]. MnO_2 has also been extensively studied as pseudocapacitive materials because they are abundant, nontoxic, and exhibit high theoretical capacitance of >1000 F g^{-1} [23]. However, the poor electrical conductivity (~10^{-5}–10^{-6} S cm^{-1}) of MnO_2 restricts electron transport and the phenomenon of dissolution in alkaline or neutral aqueous electrolyte destroys the whole structure [77]. Conducting polymers exhibit high conductivities, such as polyaniline (PANI, 0.01–5 S cm^{-1}) and polypyrrole (PPy, 0.3–100 S cm^{-1}), and fast charge–discharge kinetics [78]. However, conducting polymers often suffer from disappointing cycling stability due to the expansion and shrinkage during the charge/discharge progress [36]. Vanadium oxides have become competitive electrode materials for intercalation pseudo-capacitance owing to the multivalence state of vanadium ions from 5+ to 2+ and tunable layer structure with sufficient active sites for ions intercalation and deintercalation [39]. The issues exist in vanadium oxides including poor electronic conductivity (10^{-2}–10^{-3} S cm^{-1}) and poor stability [79]. Table 1 compared the advantages and disadvantages of typical electrode materials for ELDCs and pseudo-capacitors.

Electrode materials for HSCs

Battery-type materials, such as transition metal hydroxides, sulfides, selenides and phosphides, can react with OH^- in alkaline electrolyte [80–82]. These materials can be combined with capacitor-type materials to assemble HSCs. As mentioned before, the nature of battery-type materials is critical for the electrochemical performances of HSCs. Transition metal oxides/hydroxides, such as Ni/Co based oxides/hydroxides, have been regarded as battery-type materials due to phase transformation during electrochemical reaction. However, the metal hydroxides possess poor electrical conductivity and mechanical stability. For example, $Ni(OH)_2$ has been successfully used in HSCs because of its high theoretical capacitance (2082 F g^{-1}) and low cost [82]. Nevertheless, α-$Ni(OH)_2$ can be transformed into low conductive β-$Ni(OH)_2$ during electrochemical reaction, resulting in poor cycling performance [83]. Transition metal sulfides are another important family of battery-type materials due to their good electrochemical activity and various stoichiometric chemistry, such as Ni_3S_2, CoS, $Zn_{0.76}Co_{0.24}S$, etc [50,84,85]. Selenium is also the element of the chalcogen group, which has lower electronegativity and larger atomic radius than sulfur. Transition metal selenides are more conductive than their sulfides counterparts because the electrical conductivity of Se (10^{-3} S m^{-1}) is much higher than that of sulfur (5×10^{-28} S m^{-1}) [86,87]. Transition metal sulfides/selenides often suffer from the low rate capability and poor cycling performance because of the degradation of structures as well as the dissolution of sulfides/selenides [88]. In contrast, TMPs electrode materials exhibit outstanding electrochemical properties (capacity, rate capability and cycling stability) compared to their hydroxides, oxides or sulfides counterparts due to the high electrical conductivity and excellent electrochemical activity, such as Ni_xP_y, Zn-Ni-P, Ni-Fe-P and $Ni_xCo_{3-x}P_y$ (summarized in Table 2). The compositions and crystal structures of TMPs are complex because of the multiple valent states of transition metal cations and variable coordination number [79]. Therefore, the desired physicochemical properties of TMPs can be acquired by controlling their compositions and structures [67]. Fig. 4 gives four examples of crystal structures for metal phosphides (M_xP_y). Among them, MoP has the hexagonal WC-type structure with the stacked nonmetal-containing prisms. MnP, FeP, CoP and NiP belong to the orthorhombic structure, in which the phosphorus atoms form chains in MnP, FeP and CoP, while the phosphorus atoms form pairs in NiP [73]. A large number of metal-phosphorus bonds can be observed in Fe_2P-type structure including Ni_2P, Fe_2P and Mn_2P. Abundant metal-metal bonds and metal-phosphorus bonds in these structures make it possible for M_xP_y to be used as electrode materials for HSCs [43]. There are ionic, covalent, or metallic bonds in M_xP_y, depending on the stoichiometry and composition elements. P frameworks show high flexibility because phosphorus-phosphorus bonding angles and distances are various, which allow for various stoichiometries and crystal structures [89].

Metal-rich and phosphorous-rich phosphides used as electrode materials for HSCs exhibit different electrochemical performance. Metal-rich (M_xP_y, $x > y$) or mono-metal ($x = y = 1$) phosphides exhibit semiconducting and metallic character due to the plentiful metal-metal bonds and strong metal-phosphorus bonds, contributing to high electrical conductivity as well as good chemical and thermal stability [67]. In contrast, phosphorus-rich metal phosphides ($x < y$) with various phosphorus-phosphorus bonds exhibit unsatisfactory thermal stability because they are out of proportion to phosphorus at high temperatures [40]. Therefore, metal-rich phosphides show many free electrons for electrical conduction. The reaction mechanism of TMPs could be expressed as follows [93,95],

$$M_xP_y + xOH^- \leftrightarrow M_xP_y(OH)_x + xe^- \quad (5)$$

Table 1
Comparison of the advantages and disadvantages of typical electrode materials with different charge storage mechanisms.

Categories	Materials	Advantages	Disadvantages	Ref.
EDLCs	Activated carbon	Low cost High surface area High cycling stability	Low specific capacitance (<200 F g^{-1})	[21]
Pseudo-capacitors	RuO_2	High theoretical capacitance (1450 F g^{-1}) High cycling stability High electrical conductivity (~10^4 S cm^{-1})	High cost Rareness	[76]
	MnO_2	Nontoxic High theoretical capacitance (>1000 F g^{-1})	Poor electrical conductivity (~10^{-5}–10^{-6} S cm^{-1}) Dissolution in alkaline or neutral aqueous electrolyte Poor structural stability	[37]
	V_2O_5	Multiple oxidation states Various crystalline structures	Poor electronic conductivity (10^{-2}–10^{-3} S cm^{-1}) Dissolution in aqueous electrolyte	[79]
	PANI	Good mechanical properties Fast charge/ion transport High conductivity	Expansion and shrinkage of materials volume	[36]

$$M_xP_y(OH)_x + xOH^- \leftrightarrow M_xP_yO_x + xH_2O + xe^- \tag{6}$$

During the charging/discharging process, TMPs convert to several different phases when reacting with the OH^- ions [96]. The OH^- adsorption energy can reveal the redox reaction kinetics, which will greatly affect the ion transfer efficiency between electrodes and electrolyte [71].

For EDLCs, the amount of charge stored (C) is constant within a fixed potential window. $C = \Delta Q/\Delta U$, where ΔQ is the amount of charge stored and ΔU is the potential window [97]. Capacitance is the charge stored when the voltage window is 1 V and it is used to evaluate the capability of charge storage. For battery-type materials, the ratio of ΔQ to ΔV is not constant throughout the whole potential window [97]. The unit of F is still used in a large amount of literature [98–101], though, it is better to calculate capacity in the unit of C or mA h [29,44,102].

Synthesis methods of TMPs

During the past decades, the synthesis routes of TMPs have been greatly extended. In this section, we review some representative synthesis methods of nanostructured TMPs, including gas-solid method, solution-phase method and emerging method.

Gas-solid method has been extensively employed to pre pare TMPs, in which metal oxides, hydroxides or other precursor are phosphatized by phosphorus resources (NaH_2PO_2, $NH_4H_2PO_2$) through annealing treatment in inert gas. The mass ratio of precursor to phosphorus resources ranges from 1:10 to 1:40 [98,103]. During the annealing process, the NaH_2PO_2 in the upstream is decomposed with the release of PH_3 at a temperature over 250 °C. Then, the PH_3 gas reacts with metal precursor in the downstream to form TMPs, described as following equations [104].

$$2NaH_2PO_2 \xrightarrow{\Delta} Na_2HPO_4 + PH_3\uparrow \tag{7}$$

$$3yMO_x + 2xyPH_3 \rightarrow 3M_yP + 3xyH_2O + (2xy - 3)P\downarrow \tag{8}$$

$$3yM(OH)_x + xyPH_3 \rightarrow 3M_yP + 3xyH_2O + (xy - 3)P\downarrow \tag{9}$$

This method is feasible and efficient. It could also maintain the original morphology of precursor after phosphorization process, which is critical to the electrochemical properties of electrode materials. However, the gas-solid reaction process can cause a large waste of phosphorus resources and the release of poisonous PH_3 gas.

Another kind of methods is solution–phase reaction, such as hydrothermal/solvothermal method, thermal decomposition and electrochemical deposition. In the hydrothermal/solvothermal process, metal salt and phosphorus resources were dissolved in ultrapure water, ethanol or N,N-Dimethylformamide (DMF). The mixture was transferred to Teflon-lined autoclave and heated at high temperature [105]. To control the structure, surfactants also need to be added into the solution. The phosphorous sources can be white phosphorous and NaH_2PO_2. The phosphorization process of hydrothermal/solvothermal reaction can be described by Eqs. (9) and (10) [89]. In the thermal decomposition, metal acetylacetonates and TOP react in hot organic solvents under an inert atmosphere (Eq. 11) [106]. The chemical bonds in TOP are broken at the temperature over 300 °C and the P atoms connect with metal atoms to form TMPs. However, it is difficult to remove the flammable organic solvents and wash the products. In the electrodeposition process, TMPs can be directly deposited on the conductive substrates in the electrolyte containing metal ions and $H_2PO_2^-$ [107]. This method tends to obtain amorphous metal phosphides and the structure may be destroyed [105].

$$MCl_2 + P_4 \xrightarrow{\text{Temperature, Time}} MP_x \tag{10}$$

$$MCl_2 + NaH_2PO_2 \xrightarrow{\text{Temperature, Time}} MP_x \tag{11}$$

$$M(acac)_2 + C_{24}H_{51}OP \xrightarrow{\substack{\text{Temperature, Time,} \\ \text{octadecene}}} MP_x \tag{12}$$

Apart from the above strategies, TMPs converted from P-containing metal-organic-flamework (MOF) materials have attracted

Table 2
Comparison of electrochemical performances of the recently reported transition metal compounds.

TMPs (corresponding hydroxides/oxides/sulfides)	Specific capacity	Rate capability	Cycling stability (cycles)	Ref.
Ni_xP_y ($Ni(OH)_2$)	1272 C g^{-1} at 2 A g^{-1} 620 C g^{-1} at 2 A g^{-1}	64% retention at 15 A g^{-1} 87.3% retention at 15 A g^{-1}	90.9% (5000) 75.9% (5000)	[90]
Zn-Ni-P (Zn-Ni LDH, Zn-Ni-O)	384 mA h g^{-1} at 2 mA cm^{-2} 310 mA h g^{-1} at 2 mA cm^{-2} 215 mA h g^{-1} at 2 mA cm^{-2}	79.43% retention at 50 mA cm^{-2} 68.63% retention at 50 mA cm^{-2} 56.42% retention at 50 mA cm^{-2}	96.45% (10,000) 76.81% (10,000) 64.62% (10,000)	[91]
Ni-Fe-P (Ni-Fe-O)	1358 C g^{-1} at 5 mA cm^{-2} 416.6 C g^{-1} at 5 mA cm^{-2}	799 C g^{-1} at 50 mA cm^{-2} 190 C g^{-1} at 50 mA cm^{-2}	94.7% (10,000) 76.9% (10,000)	[92]
$Ni_xCo_{3-x}P_y$ ($NiCo_2S_4$)	492 mA h g^{-1} at 1 A g^{-1} 436.7 mA h g^{-1} at 1 A g^{-1}	68% retention at 20 A g^{-1} 62% retention at 20 A g^{-1}	96% (10,000) 91.7% (1000)	[93]

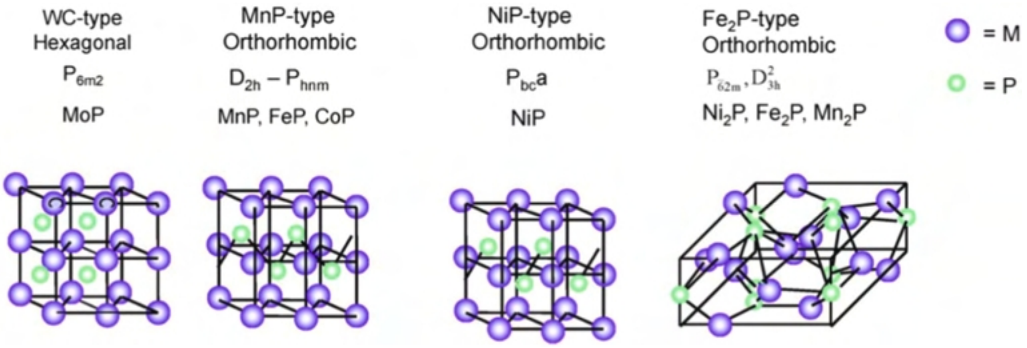

Fig. 4. Crystal structures of metal phosphides.
Copyright 2009 Elsevier. Reproduced from ref [94].

greatly attention in recent years. The metal ions can coordinate with organophosphorus to generate MOF. For example, the 1,3,5-triaza-7-phosphaadamantane (PTA, $C_6H_{12}N_3P$) and copper ions are used to construct Cu-metal-organic-flamework (Cu/PTA-MOFs) [108]. The Cu_3P/carbon nanosheet can be prepared by annealing the Cu/PTA-MOFs without other phosphorus resources. In addition, the Ni^{2+} could connect with H_3TPO to form $[Ni_2(TPO)_4/_3(dabco)]$ (BMM-10) [109]. After Fe^{3+} ions etching and carbonization treatment, hollow FeNiP/C nanoparticles were obtained. This method is ecofriendly without release of PH_3 and conductive to synthesize nanomaterials with high specific surface area and abundant pore structure.

TMPs composition chemistry

Generally, element P coordinates with many transition metals to form a series of TMPs. The metallic elements that are frequently used to design TMPs for HSCs are shown in Fig. 5. Most of them display multiple valent states. Herein, single-metal, binary-metal and ternary-metal phosphides used as electrode materials for HSCs are discussed below in detail.

Single-metal phosphides

Nickel and cobalt are the most frequently used to form TMPs. Nickel phosphides possess high theoretical capacitance while cobalt phosphides show good electrochemical stability [110–112]. As shown in Fig. 6a, the interconnected Ni_2P nanosheets were grown uniformly on the Ni foam surface, which can provide sufficient space for ion diffusion [113]. The active Ni and P with rich valences facilitate electron transfer and produce abundant active sites for redox reactions, enhancing the specific capacitance. The Ni_2P nanosheets show higher conductivity of 1.2×10^3 S cm^{-1} than that of $Ni(OH)_2$ (10 S cm^{-1}) which confirms the improved conductivity of metal phosphides. The Ni_2P nanosheets exhibit a specific capacitance of 3496 F g^{-1} at 2.5 A g^{-1}, which is higher than that of $Ni(OH)_2$ nanosheets (~1000 F g^{-1}) at the same current density, and maintain 1109 F g^{-1} at 83.3 A g^{-1}. When cycled at 10 A g^{-1}, a rapid capacitance fading can be observed before 2000 cycles which may be ascribed to the $Ni(OH)_2$ generated from the reaction of Ni_2P nanosheets and electrolyte. After 2000 cycles, the $Ni(OH)_2$ on Ni_2P could protect the whole structure and ensure good cycling stability (Fig. 6b). NiP_x nanoflakes consist of hexagonal Ni_2P phase, hexagonal Ni_5P_4 phase and tetragonal $Ni_{12}P_5$ phase as shown in Fig. 6c [114]. Benefiting from the outstanding electrical conductivity enhanced by the mixed-phase in NiP_x nanoflakes, an ultrahigh volumetric capacitance of 817 F cm^{-3} is achieved at 2 mA cm^{-2} and the capacitance retains 434 F cm^{-3} even at 100 mA cm^{-2}, exhibiting excellent rate capability. CoP nanoparticles were synthesized via a facile mechanical alloying method under argon protection (Fig. 6d) [111]. Pure CoP phase could be formed when annealing Co-P precursor at 200 °C and exhibit the best electrochemical performance (Fig. 6e). When the annealing temperature is increased to 500 °C, these small particles agglomerate together, leading to the decrease of specific surface area and active sites. The pure CoP electrode delivers specific capacitances of 447, 437, 421, 342, and 314 F g^{-1} at current densities of 1, 2, 4, 8, and 10 A g^{-1}, respectively. After 5000 cycles at 1 A g^{-1}, the specific capacitance maintains 84.3% of initial capacitance due to the stable crystal structure (Fig. 6f). Apart from nickel phosphides and cobalt phosphides, Cu_3P tube-like nanostructure was fabricated by electro-oxidation and phosphorization on copper foil [115]. The electrode delivers a specific capacitance of 301 F g^{-1} at 2.5 mA cm^{-2}, while the capacitance decreases to 130 F g^{-1} at 4.5 mA cm^{-2}, which is due to the large IR drop from high resistance. This problem can also be found in one dimension MoP, which exhibits specific capacitance of 470 and 122 F g^{-1} at 2 and 15 A g^{-1}, respectively (Fig. 6g) [116]. The poor rate capability was not carefully discussed in this paper. However, the MoP electrode shows excellent long-term cycling stability of 92% after 10,000 cycles (Fig. 6h).

Fig. 5. Elements that are used to form TMPs for supercapacitors.

Binary-metal phosphides

Most single-metal phosphides often suffer from either low electrical conductivity or poor structural stability, which result in poor rate capability and poor long-term cycling stability as discussed in Section 3.1 [111,117,118]. Compared to single metal phosphides, binary-metal phosphides usually have better electrochemical reactivity, higher electronic conductivity and richer redox reactions, which are ascribed to the synergistic effects of various transition metal elements [71,119]. On the one hand, both metal cations participate in the redox reaction and contribute to the charge storage, such as Ni-Co phosphides [93,95], Ni-Fe phosphides [92] and Co-Mn phosphides [120]. The multiple oxidation states of different metals could provide higher capacity than single-metal phosphides [121]. On the other hand, one metal cation participates in the redox reaction to provide capacity, while another not related to redox reaction promotes the electrochemical activity and stabilizes the structure during the cycling process [122], including Ni-Mo phosphides [123], Co-Mo phosphides [124], and Zn-Ni phosphides [91].

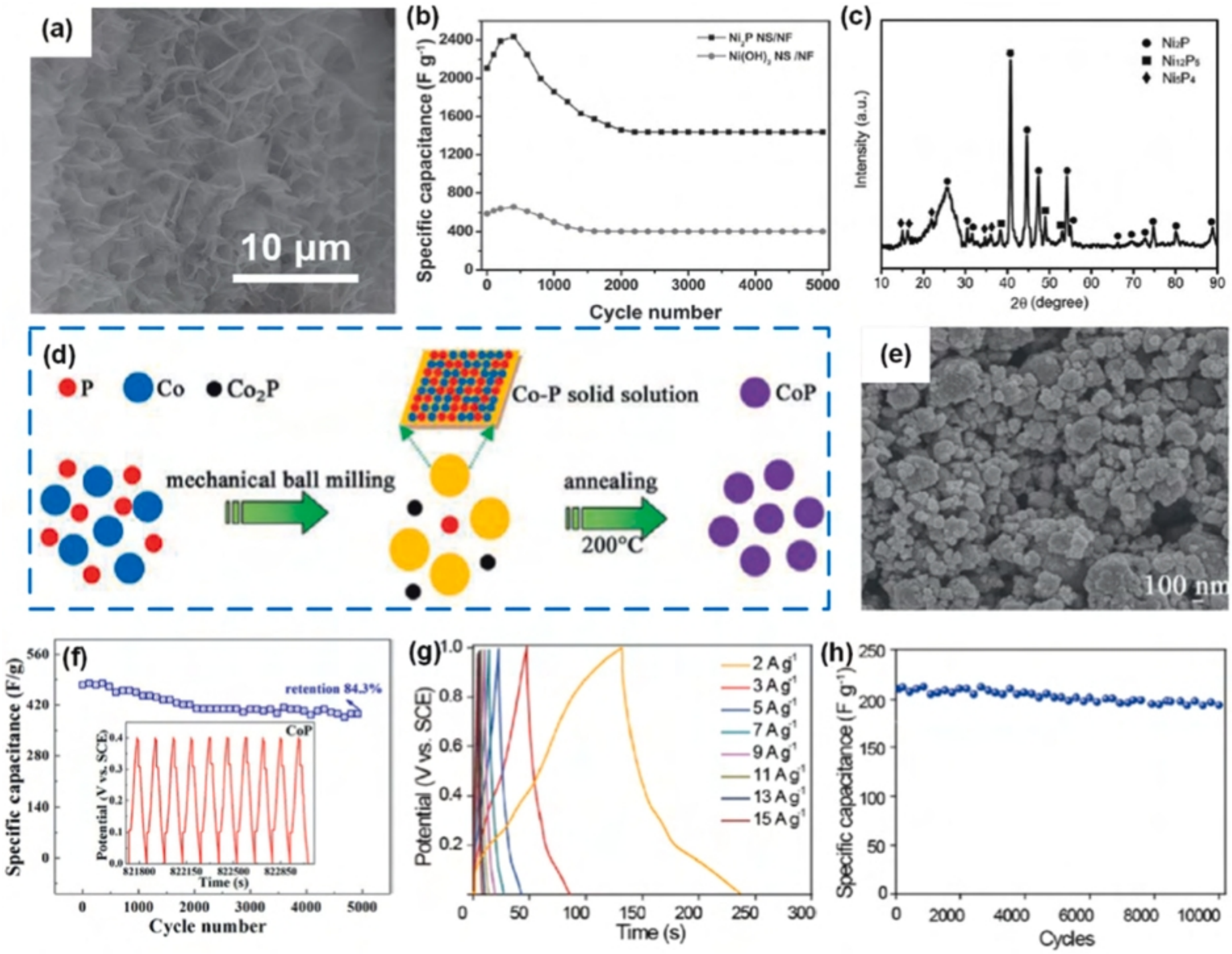

Fig. 6. (a) SEM picture of Ni_2P NS/NF. (b) Cycling stability of the Ni_2P and $Ni(OH)_2$. (c) XRD pattern of NiP_x. (d) Schematic illustration of the formation mechanism of the CoP nanoparticles. (e) SEM image of CoP nanoparticles. (f) Cycling stability. (g) GCD plots, and (h) Cycling performance of MoP.
(a, b) Reproduced from ref [113]. Copyright 2015 Wiley-VCH. (c) Reproduced from ref [114]. Copyright 2016 Royal Society of Chemistry. (d–f) Reproduced from ref [111]. Copyright 2017 Elsevier. (g, h) Reproduced from ref [116]. Copyright 2020 American Chemical Society.

Among various binary-metal phosphides, nickel cobalt phosphides (NiCoP) are paid wide attention on. The typical crystal structure of NiCoP is shown in Fig. 7a [125], which has the Fe_2P-type structure. Partial Ni atoms are substituted by Co atoms in Ni_2P structure without changing the crystal structure. NiCoP possesses both covalent and metallic metal-phosphorus bonds in which covalent bonds can store charges through faradaic redox reactions to provide capacity while metallic bonds offer free electrons to enhance the electrical conductivity [110]. For instance, hollow NiCo-P nanocages derived from MOFs possess synergistic effects between Ni and Co ions and high electrical conductivity after phosphorization treatment as shown in Fig. 7b [71]. The NiCo-P nanocages present low OH^- adsorption energy, indicating facile OH^- adsorption on the electrode materials during electrochemical reactions and fast reaction kinetics compared to the corresponding single metal counterparts (Fig. 7c). In addition, NiCo-P without a band gap is metallic, further indicating the superior electrical conductivity (Fig. 7d) [71]. The NiCo-P nanocages deliver a high specific capacity of 894 C g^{-1} at 1 A g^{-1} with a capacity retention of 72.4% even at 40 A g^{-1}. Free-standing amorphous nanoporous Ni-Co-P was synthesized by an electrochemical dealloying process [119]. In this amorphous phase, the coordination numbers of Ni-Ni, Ni-P and Co-P are lower than theoretical values, indicating abundant Ni and P vacancies, which provide a large number of active sites. New phases such as $Ni_xCo_{1-x}OOH$ and $(Ni_yCo_{1-y})_2P_2O_7$ are formed during the electrochemical activation process, which increase the species of redox reactions. The amorphous np-Ni-Co-P exhibits a capacity of 171.4 mA h cm^{-3} at 1 A cm^{-3}, which is higher than that of np-Ni-P (102 mA h cm^{-3}) and np-Co-P (64.4 mA h cm^{-3}). Even at a high current density of 100 A cm^{-3}, np-Ni-Co-P still shows a capacity of 108.5 mA h cm^{-3} with a capacity retention of 63.2% (Fig. 7e). After 20,000 cycles, a capacitance retention of 84% is presented by np-Ni-Co-P. The NiCoP nanosheets grown on Ni foam exhibit a higher specific capacitance of 2143 F g^{-1} at 1 A g^{-1} than that of $NiCoO_2$ (775 F g^{-1} at 1 A g^{-1}), with an outstanding rate capability (1615 F g^{-1} at 20 A g^{-1}) due to the high electrical conductivity [126]. However, a poor cycling stability (73% after 2000 cycles) of NiCoP nanosheets is not explained compared to the $NiCoO_2$ electrode without phosphorization treatment (Fig. 7f).

Beyond bimetallic nickel cobalt phosphides, other binary-metal phosphides are also investigated. For example, compared to Co^{2+}, Zn^{2+} possesses higher redox reaction kinetics and stronger coordination capability, which could boost the electrochemical properties [91]. The high value of the potential gap between anodic and cathodic peaks in Zn-Ni-P (~186 mV) demonstrates the quasi-reversible reaction kinetics. In addition, the charge-transfer resistance

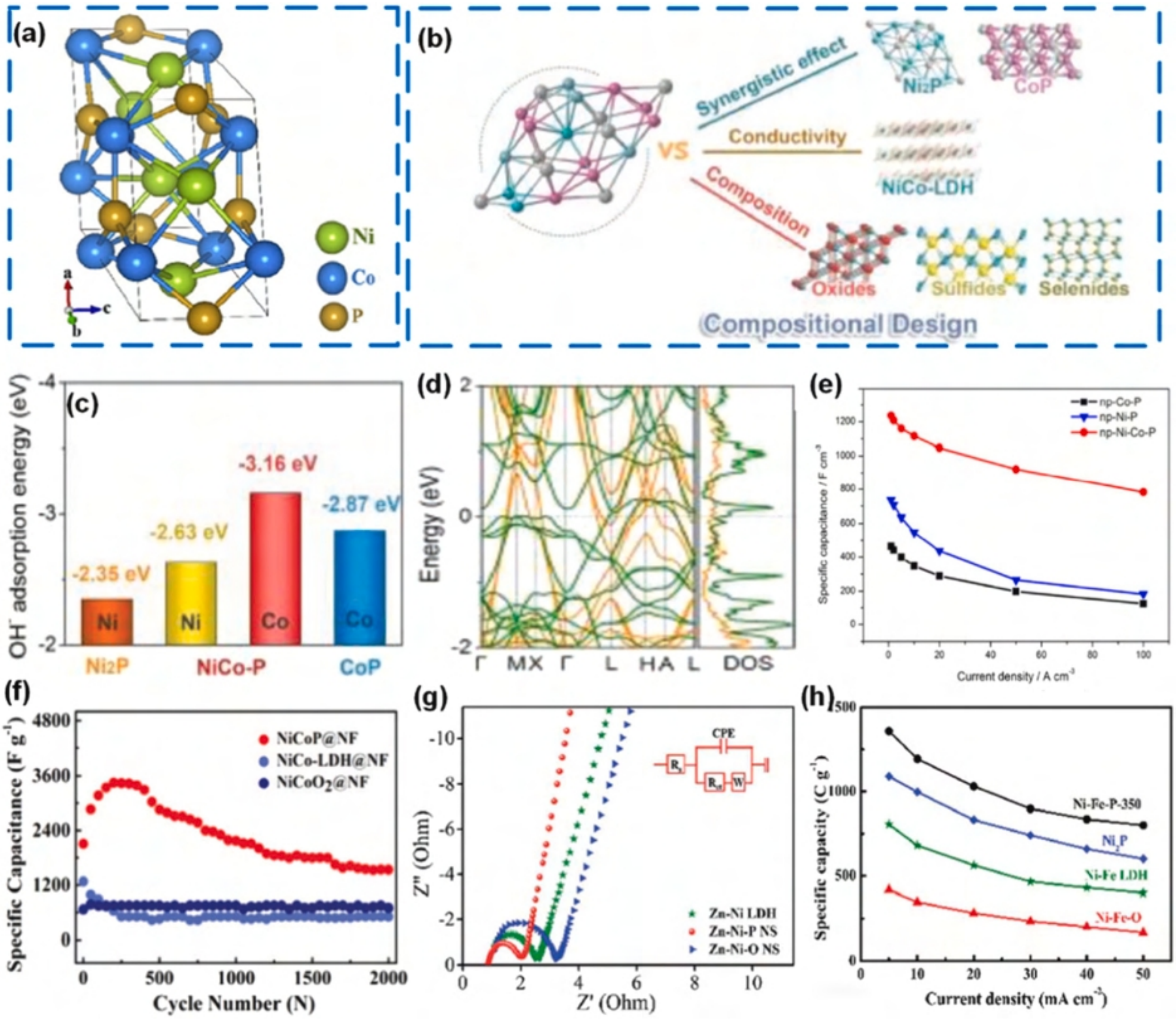

Fig. 7. (a) Crystal structure of NiCoP. (b) Compositional design of NiCo-P. (c) OH^- absorption energy. (d) Densities of states. (e) Rate capability. (f) Cycling stability of NiCoP@NF, NiCo-LDH@NF and $NiCoO_2$@NF. (g) EIS of Zn–Ni LDH, Zn–Ni–O, and Zn–Ni–P electrodes. (h) Specific capacity at different current densities.
(a) Reproduced from ref [125]. Copyright 2020 Elsevier. (b–d) Reproduced from ref [71]. Copyright 2019 Wiley-VCH. (e) Reproduced from ref [119]. Copyright 2019 Elsevier. (f) Reproduced from ref [126]. Copyright 2018 Royal Society of Chemistry. (g) Reproduced from ref [91]. Copyright 2018 Royal Society of Chemistry. (h) Reproduced from ref [92]. Copyright 2019 Royal Society of Chemistry.

of Zn-Ni-P is smaller than that of Zn-Ni LDH and Zn-Ni-O as shown in the Nyquist plots (Fig. 7g), ensuring fast electron transport. Zn-Ni-P nanosheets exhibit a high specific capacity of 384 mA h g^{-1} at a current density of 2 mA cm^{-2} and outstanding cycling stability (retaining 96% after 10,000 cycles) [91]. After repeated charging/discharging process, the morphology of Zn-Ni-P and porous structure can still be maintained, ensuring the good cycling performance. The surface composition of Zn-Ni-P is slightly changed to NiOOH and ZnOOH due to the electrochemical oxidation. Ni–Fe phosphides nanosheets are also considered as one kind of promising binary transition metal phosphides for HSCs. The conductivity of Ni-Fe-P is increased compared with that of Ni_2P because of the strong internal bonding of Fe-P and the excess electrons distribute near the Fermi level [92]. The Ni–Fe–P electrode exhibits a specific capacity of 1358 C g^{-1} at 5 mA cm^{-2}, which is higher than that of Ni_2P (1100 C g^{-1}), Ni-Fe-LDH (805 C g^{-1}) and Ni-Fe-O (417 C g^{-1}), with excellent rate capability (799 C g^{-1} at 50 mA cm^{-2}) (Fig. 7h). The 3D architecture of Ni-Fe-P and porous nanosheets are not much affected during the cycling test. In addition, the small content of metal oxides/hydroxides are formed on the surface of metal phosphides. The metal phosphides act as core materials which are protected by the oxidation layer, contributing to the electrochemical properties.

Ternary-metal phosphides

Ternary-metal phosphides may offer more redox active sites and higher conductivity than their corresponding single-metal and binary-metal phosphides because of the synergistic effects, multiple phase and abundant structural defects introduced by the incorporation of multi-metal ions, which are beneficial to the electrochemical energy storage [127,128].

ZnNiCo-P nanosheets were grown on Ni foam via a facile chemical bath deposition process and phosphorization treatment (Fig. 8a–c) [129]. Zn ions possess high chemical activity and good electrical conductivity as mentioned before and Ni ions could produce more polarons, thus increasing electrical conductivity [55,130–133]. More active sites and redox reaction species are introduced due to the increase of Co^{3+} after the introduction of Zn and Ni ions. ZnNiCo-P presents large charge density around the Fermi level and Ni and Co become more active compared with pristine

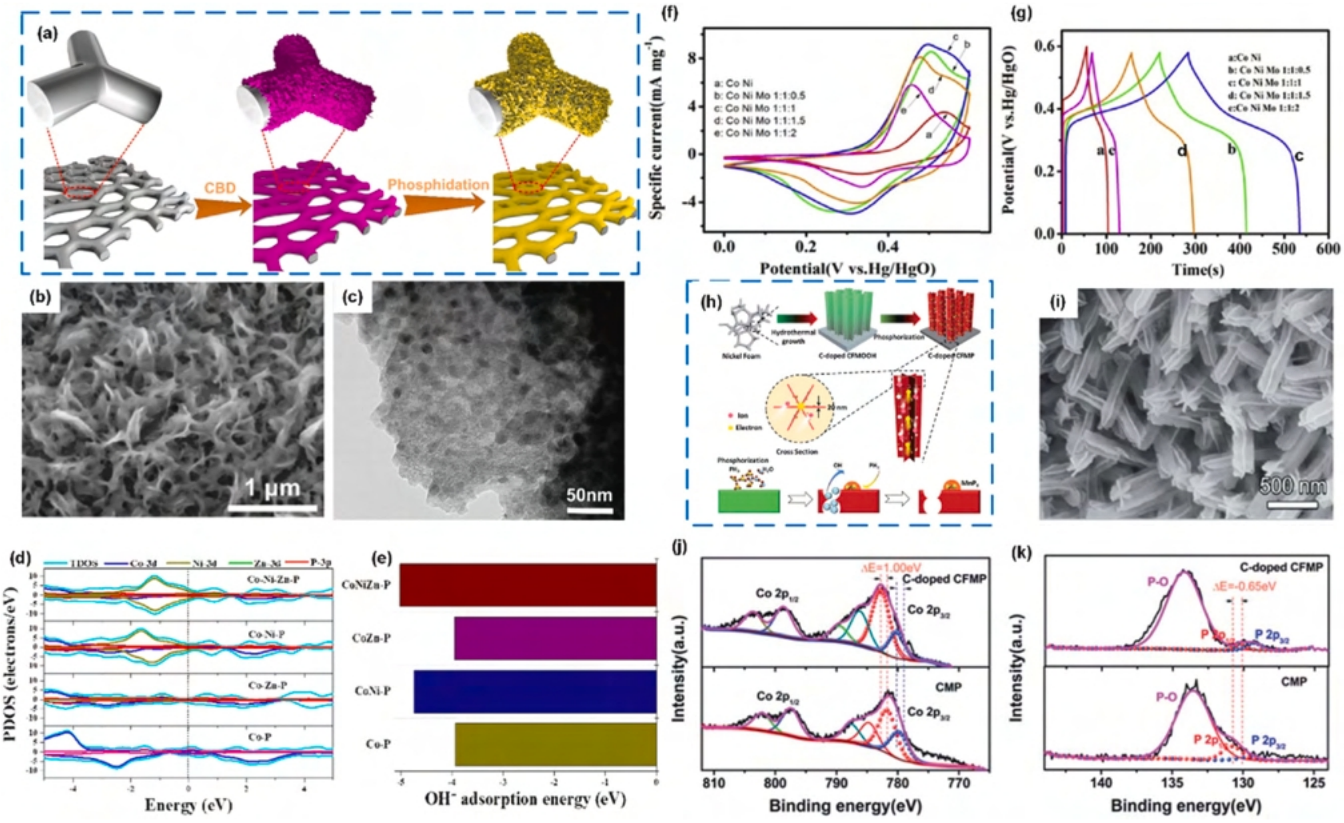

Fig. 8. (a) Schematic illustration of the formation of ZnNiCo-P nanosheets. (b) SEM and (c) TEM of ZnNiCo-P nanosheets. (d) DOS of Co-P nanowire, NiCo-P nanowire, ZnCo-P nanosheet and ZnNiCo-P nanosheet electrodes. (e) Adsorption energies of OH^- on Co-P, NiCo-P, ZnCo-P and ZnNiCo-P. (f and g) CV plots and GCD curves. (h) Schematic illustration of the formation of CCMFP. (i) SEM image. XPS spectra of (j) Co 2p and (k) P 2p.
(a–e) Reproduced from ref [129]. Copyright 2020 Elsevier. (f, g) Reproduced from ref [134]. Copyright 2020 Elsevier. (h–k) Reproduced from ref [135]. Copyright 2019 Royal Society of Chemistry.

Co_2P, NiCo-P and ZnCo-P, which provide more charge carriers for the redox reactions (Fig. 8d). In addition, the OH^- absorption energy of ZnNiCo-P is the lowest because all cations can serve as OH^- adsorption sites, indicating a fast OH^- adsorption/desorption process and rapid reaction kinetics (Fig. 8e). When cycled 6000 cycles at 20 A g^{-1}, the electrode retains 90% of initial capacity. The whole nanosheets can be well preserved while the surface becomes rough and agglomerate during the cycling test. The ZnNiCo-P nanosheets show the highest specific capacity of 958 C g^{-1} at 1 A g^{-1} and a considerable rate capability (787 C g^{-1} at 20 A g^{-1}) than NiCo-P nanowires, ZnCo-P nanosheets and Co-P nanowires. Another similar work also reports that Zn-Ni-Co-P nanowires deliver high specific capacities of 1269 C g^{-1} at 3 A g^{-1} and 920 C g^{-1} at 20 A g^{-1}, respectively, much higher than that of ZNCO [133]. The introduction of zinc ions could adjust the band gap to modify electronic properties, and produce lattice defects, which result in the increased electron-conduction channels for electrochemical reactions.

Nickel-cobalt-molybdenum ternary phosphide with different mole ratios of Mo is another system to have been investigated [134]. Fig. 8f shows the CV curves of different NCMP@CC electrodes. The electrodes with the introduction of Mo resulted in a larger integral area of the CV curves compared with NiCoP@CC electrode, which is possibly attributed to the improved electrical conductivity. The electrode with the ratio of 1:1:1 attained the highest specific capacitance of 508 F g^{-1} at a current density of 0.2 A g^{-1} (Fig. 8g). Carbon doped Co–Mn–Fe hexagonal prism arrays have also been studied (Fig. 8h and i); the addition of Fe enhanced electrical conductivity [135]. As shown in Fig. 8j and k, the $Co2p_{3/2}$ peaks in carbon doped Co–Mn–Fe phosphides move towards higher binding energy, while the P2p peaks shift to lower binding energy compared with the corresponding peaks in Co–Mn phosphides. Some Co^{2+} are converted into Co^{3+} after the introduction of iron, resulting in an enhanced electrical conductivity. The electrode demonstrated a high specific areal capacitance (4.36 F cm^{-2} at 2 A cm^{-2}) compared to Co–Mn phosphides (~3 F cm^{-2} at 2 A cm^{-2}).

Nanostructures of TMPs electrodes

The property of battery-type materials associates with ion diffusion rate, electron transport path and active sites of redox reactions [136]. Nanomaterials, compared with bulk materials, show good prospects in high-performance HSCs due to the large surface area and high chemical activity [137]. The nanostructures can make it easy to contact with the electrolyte and reduce diffusion distances. The capacity can be increased by 2–4 times compared with the conventional structured materials because of the nanoscale effect [49]. In this section, various nanostructured TMPs including zero-, one-, two- and three-dimensional structures will be discussed in detail.

Zero-dimensional TMPs

Zero-dimension (0D) structures are commonly nanoparticles and spherical materials [18]. In addition, particles with the size of ~1 μm are also regarded as 0D materials [138]. The small particles can provide large surface areas, increase the contact areas and reduce diffusion distance between active materials and electrolyte [137,139]. Solid and hollow 0D structures used as electrodes are considered in this section. For example, the amorphous Ni-P nanoparticles with a uniform size of 50–100 nm were fabricated via a

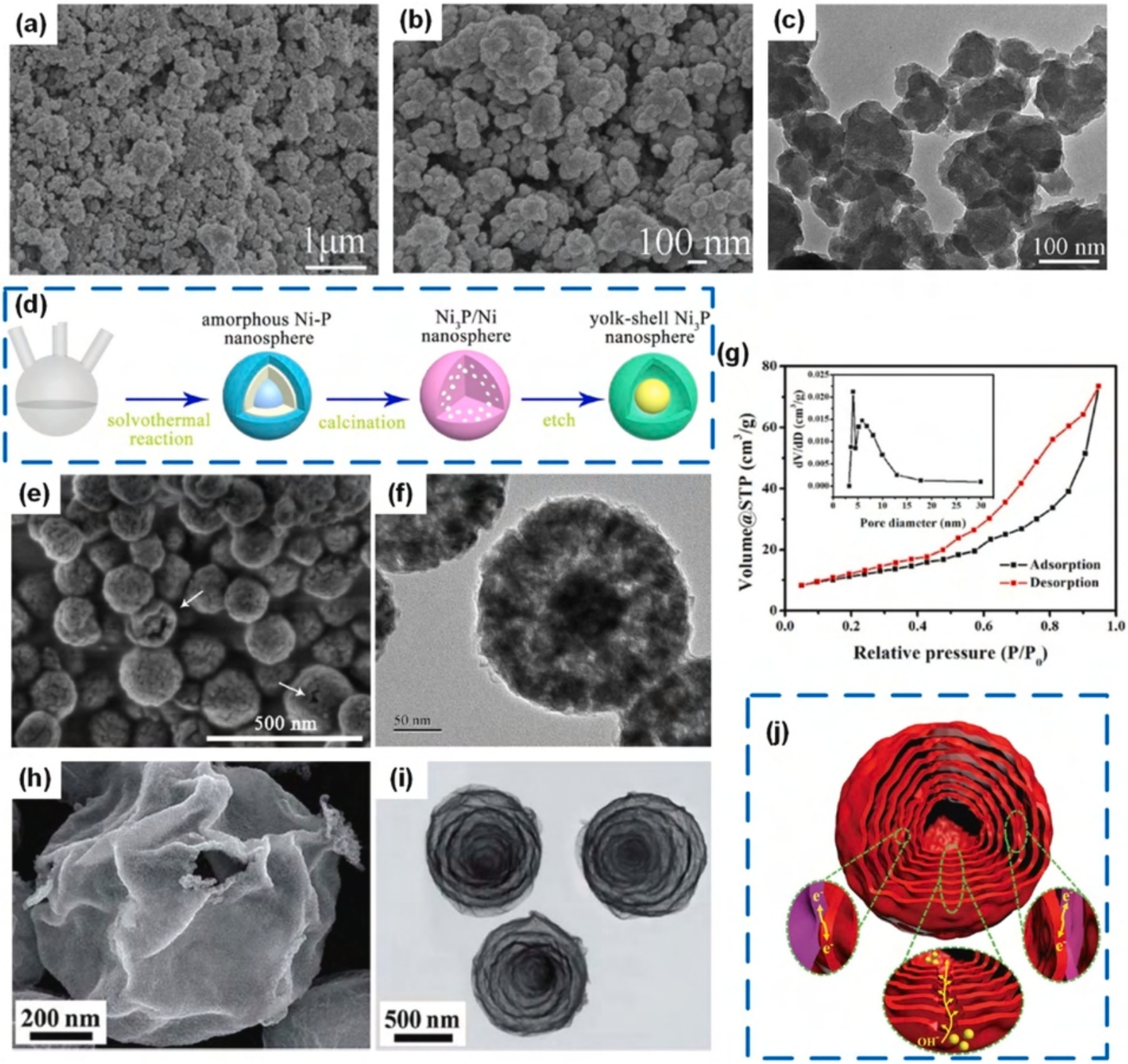

Fig. 9. (a and b) SEM and (c) TEM images of Ni-P nanoparticles. (d) Schematic illustration of the formation mechanism of yolk-shell Ni_3P nanospheres. (e) SEM and (f) TEM images of yolk-shell Ni_3P nanospheres. (g) N_2 adsorption-desorption isotherm and pore size distribution curve. (h) SEM and (i) TEM images of multi-shelled copper cobalt phosphide hollow spheres. (j) Schematic illustration of multi-shelled nanoporous CuCoP hollow microspheres.
(a–c) Reproduced from ref [118]. Copyright 2015 Elsevier. (d–g) Reproduced from ref [143]. Copyright 2020 Elsevier. (h–j) Reproduced from ref [144]. Copyright 2017 Royal Society of Chemistry.

facile solvothermal method [118]. The loose structure and nanosized particles (Fig. 9a, b and c) are in favor of the effective contact between nanoparticles and electrolyte. The amorphous Ni-P delivers high specific capacitances of 1597 F g^{-1}, 1338 F g^{-1},1119 F g^{-1}, 964 F g^{-1}, and 800 F g^{-1} at current densities of 0.5 A g^{-1},1 A g^{-1}, 2 A g^{-1}, 4 A g^{-1}, and 8 A g^{-1}, respectively. However, when cycled Ni-P electrode at 4 A g^{-1}, 26.2% capacitance loss occurs during the first 100 cycles, which is due to the irreversible faraday reactions and degradation of the structure. After 100 cycles, the electrode shows good cycling stability. Yolk-shell and multi-shelled particles often possess short ions/electrons transfer paths, high shell-permeability and abundant active sites [140,141]. In addition, the energy density can be enhanced by increasing the weight fraction of the electroactive materials in the hollow interior space [142]. The yolk-shell Ni_3P nanospheres were fabricated via a solvothermal method following by selective etching (Fig. 9d) [143]. The as-synthesized yolk-shell nanospheres (diameter ~130 nm) consist of many small nanoparticles (Fig. 9e and f), thus the electrolyte can easily penetrate through the shell for efficient redox reactions. The BET analysis shows that the yolk-shell Ni_3P nanospheres have a high specific surface area of 62 m^2 g^{-1} (Fig. 9 g), which provides ample contact areas between electrode and electrolyte to facilitate the electrochemical reaction. The yolk-shell Ni_3P delivers high specific capacities of 750 C g^{-1} and 476 C g^{-1} at the current densities of 1 A g^{-1} and 10 A g^{-1}, respectively. Another multi-shelled copper cobalt phosphide hollow spheres were prepared by a facile template-free method (Fig. 9 h) and exhibited a high specific capacitance of 1946 F g^{-1} at 5 mA cm^{-2} with excellent rate capability even at 150 mA cm^{-2} (retaining 61% of its capacitance) [144]. After 6000 cycles, the electrode retains 92.7% of initial capacitance, indicating excellent cycling stability. The outstanding properties are attributed to the ultrathin shells (~20–30 nm) (Fig. 9i) and high surface area

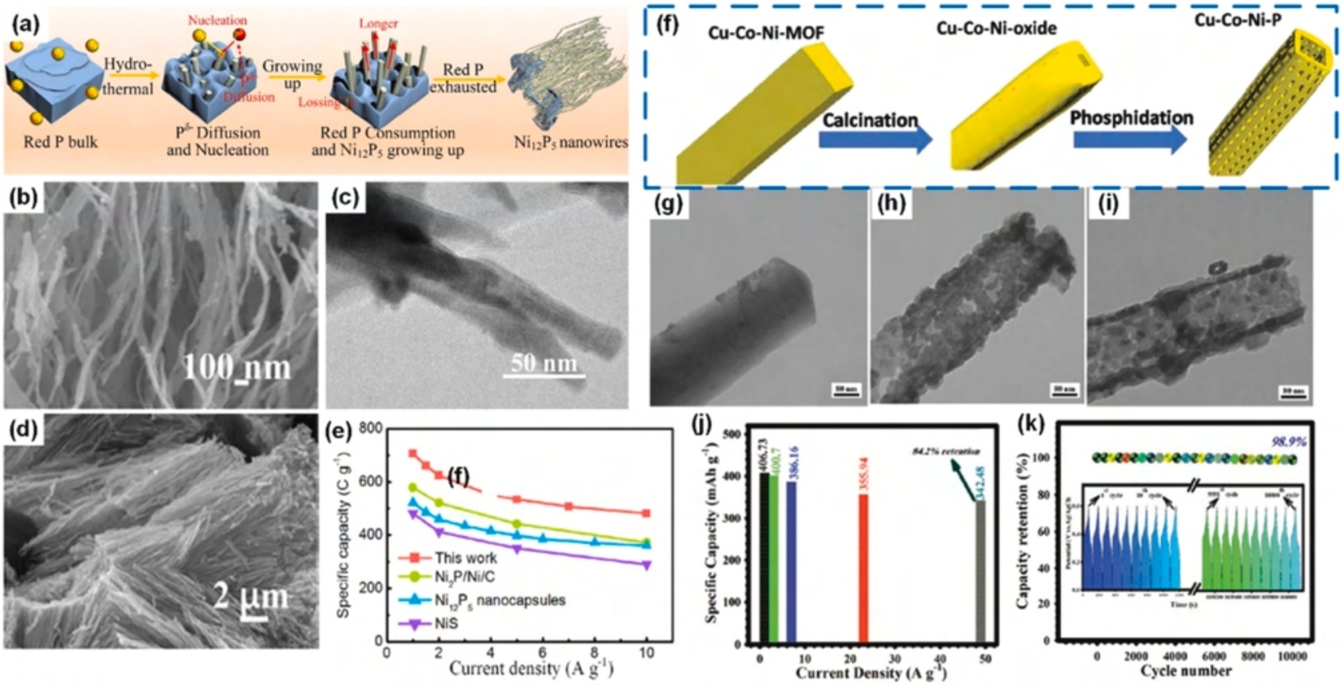

Fig. 10. (a) Schematic illustration of the formation of $Ni_{12}P_5$ nanowires. (b and d) SEM and (c) TEM images of $Ni_{12}P_5$ nanowires. (e) Rate capability. (f) Schematic illustration of the formation of Cu-Co-Ni-P nanotubes. TEM of (g) Cu-Co-Ni-MOF, (h) Cu-Co-Ni-oxide and (i) Cu-Co-Ni-P nanotubes. (j) Rate capability. (k) Cycling stability of Cu-Co-Ni-P nanotubes. (a–e) Reproduced from ref [146]. Copyright 2020 Elsevier. (f–k) Reproduced from ref [149]. Copyright 2020 Royal Society of Chemistry.

($54\ m^2\ g^{-1}$), which provide short transport pathways for electron transfer, resulting in fast reaction kinetics. The abundant space between the shells act as reservoirs for electrolyte, improving the accessibility of electrolyte throughout the whole structure, thereby ensuring sufficient electrochemical reaction (Fig. 9j).

One-dimensional TMPs

0D materials often suffer from the agglomeration of nanoparticles which restricts the sufficient use of surface areas and the single morphology cannot provide special active sites to further facilitate the redox reactions [74]. One-dimensional (1D) nanomaterials have attracted increasing interest in energy-related applications due to their unique physical and chemical characteristics, such as high length-to-diameter ratio and 1D electronic pathways [145]. In addition, 1D nano-architectures possess the “highway” for charge transport along the axial direction and high ion-accessible surface area [27,139]. 1D $Ni_{12}P_5$ nanowires were synthesized using a one-step facile hydrothermal method [146]. The formation process of $Ni_{12}P_5$ nanowires is the reaction of $P^{\delta-}$ on the surface of red P and Ni^{2+} ions in aqueous solution with the consumption of red P (Fig. 10a). With the increase of reaction time, the length of $Ni_{12}P_5$ nanowires becomes longer with the width of ~20 nm (Fig. 10b, c and d) and the structure becomes more stable according to the stronger diffraction peaks around 50–60° in XRD patterns. The nanowires possess a large specific surface area of ~$60\ m^2\ g^{-1}$ and exhibit a high conductivity of $13.8\ S\ cm^{-1}$. The $Ni_{12}P_5$ nanowires show specific capacities of $707\ C\ g^{-1}$ and $481\ C\ g^{-1}$ at the current densities of $1\ A\ g^{-1}$ and $10\ A\ g^{-1}$ (68% of retention rate), respectively, which is ascribed to the large lattice gap, providing more lattice attachment sites and ion channels (Fig. 10e). However, the cycling stability of $Ni_{12}P_5$ nanowires is unsatisfactory (only 53% after 1000 cycles).

Binder-free 1D nanoarrays such as nanowires, nanotubes and nanorods also show good perspective because of the improved electrical conductivity of electrode materials without additional polymer binder and conductive agent [130,147]. These unique 1D structures provide high specific surface areas for electrode–electrolyte contact and expose more active sites for redox reaction [148]. For example, the MOF-derived Cu–Co–Ni–P nanotube arrays grown on Ni foam possess large surface area ($125.6\ m^2\ g^{-1}$) and present mesoporous character (~2.3 nm) (Fig. 10f–i), which are beneficial for the penetration of the electrolyte ions [149]. The abundant pores in the nanotube provide more active sites and sufficient contact, which promote the redox reaction and boost the capacity. The CuCoNi-P nanotubes deliver specific capacities of 406, 400, 386, 355, and $342\ mA\ h\ g^{-1}$ at 2, 4, 8, 24, and $50\ A\ g^{-1}$, respectively (Fig. 10j). It is worth noting that 98.9% of its initial capacity still remains after 10,000 cycles at $24\ A\ g^{-1}$(Fig. 10k) because the nanotube structures could alleviate the volume strain.

Two-dimensional TMPs

Two-dimensional materials have attracted increasing interest in energy storage and conversion due to their considerable mechanical stability and short ion transfer paths [150]. Compared to 1D materials, the ultra-thin 2D nanosheets can enhance the rate capability by alleviating the phenomenon of electrode materials pulverization at high current densities and improve cycle lifespan by accommodating the volume change during the cycling test [151]. A sheet-like NiCoP structure was synthesized via a hydrothermal method and phosphorization treatment (Fig. 11a) [152]. The porous and sheet-like structure (Fig. 11b and c) is in favor of the diffusion of electrolyte and transmission of electrons. The S-NiCoP electrode with a mass loading of $4\ mg\ cm^{-2}$ shows a specific capacitance of $1206\ F\ g^{-1}$ at $1\ A\ g^{-1}$, much higher than that of Ni–Co precursor ($566\ F\ g^{-1}$), CoP-300 ($404\ F\ g^{-1}$) and NiP-300 ($436\ F\ g^{-1}$). Even at a high current density of $20\ A\ g^{-1}$, the S-NiCoP electrode can retain a discharge capacitance of $612\ F\ g^{-1}$ (Fig. 11d). When the mass loading is increased to $13.5\ mg\ cm^{-2}$, the S-NiCoP sample still shows a high capacitance of $1095\ F\ g^{-1}$, and the areal capacitance is increased from $4.9\ F\ cm^{-2}$ to $14.8\ F\ cm^{-2}$. The improvement of areal capacitance may be assigned to the dense and stacked sheet-like structure, which could facilitate

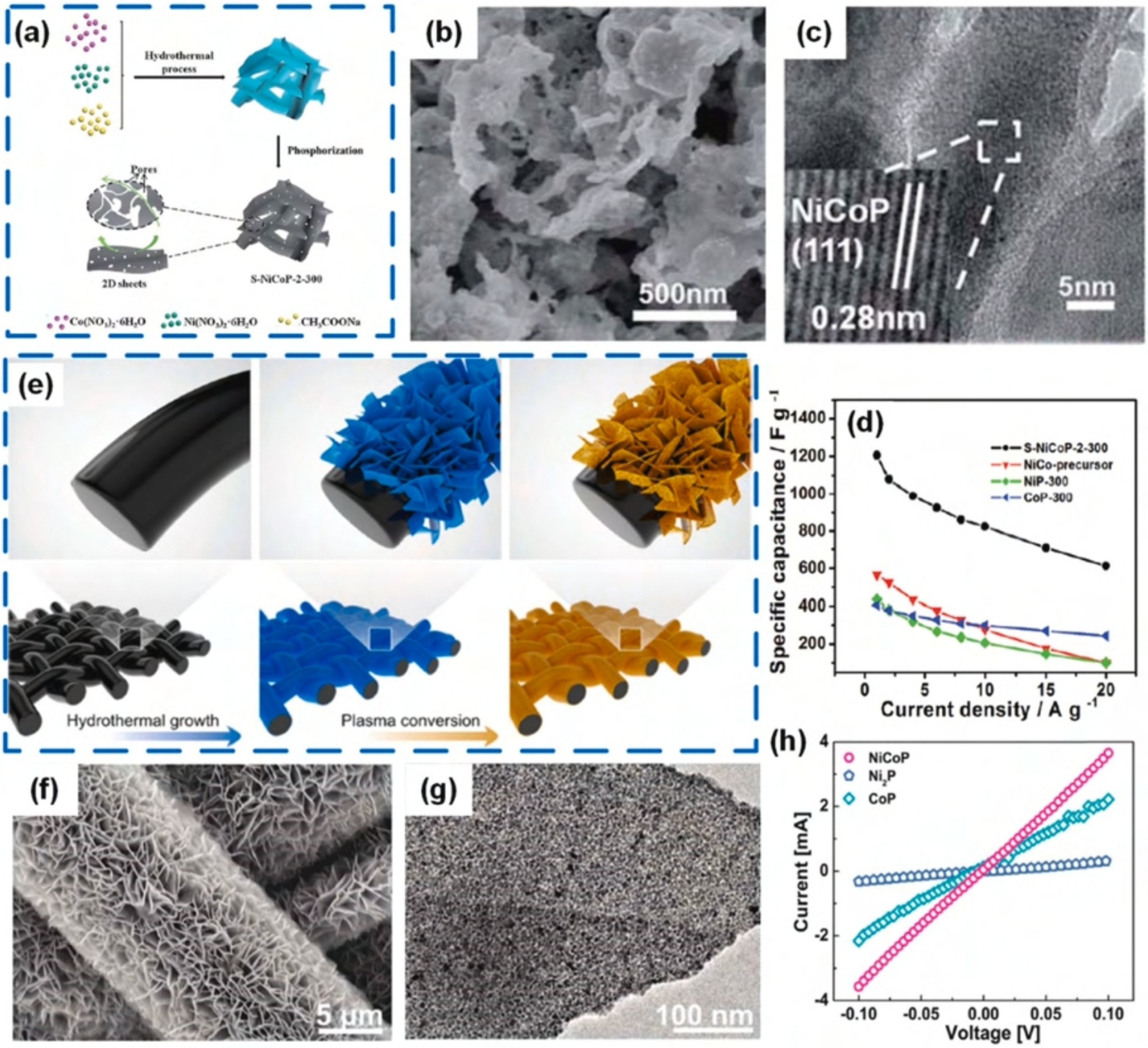

Fig. 11. (a) Schematic fabrication process of S-NiCoP. (b) SEM and (c) TEM image of S-NiCoP. (d) Rate capability of S-NiCoP. (e) Schematic illustration of the formation of NiCoP nanoplates. (f) SEM and (g) TEM images of NiCoP nanoplates. (h) I-V characteristics of NiCoP, Ni_2P and CoP single nanoplates.
(a–d) Reproduced from ref [152]. Copyright 2018 Royal Society of Chemistry. (e–h) Reproduced from ref [153]. Copyright 2017 Elsevier.

the electrons transfer from the electrode surface to the current collector even at high mass loading.

To avoid the restacking of 2D nanomaterials, which could restrict the electron and mass transport and reduce the utilization of electrode materials, the 2D nanomaterials are directly grown on a conductive substrate [151]. Low temperature PH_3 plasma was employed to fabricate 2D NiCoP nanoplates grown on carbon cloth (Fig. 11e-g) [153]. The conductivity of NiCoP (909 S cm^{-1}) could be achieved from the linear I-V characteristics indicative of ohmic contact behavior, which is higher than that of CoP (370 S cm^{-1}) and Ni_2P (244 S cm^{-1}) (Fig. 11h). In addition, the DOS of NiCoP is closer to the Fermi level, which suggests that NiCoP is intrinsically more reactive and have better electrochemical activity. The NiCoP electrodes can deliver an excellent specific capacity of 194 mA h g^{-1} at 1 A g^{-1}, which is higher than that of Ni_2P (166 mA h g^{-1}) and CoP (108 mA h g^{-1}). After increasing the current density to 10 A g^{-1}, a specific capacity of 169 mA h g^{-1} is maintained with a high rate capability of 87%. When cycled at 20 A g^{-1}, 81% of the initial capacity is achieved for NiCoP after 5000 cycles. After the cycling test, the nanoplates are well preserved while some nanoparticles are formed on the surface. The surface of NiCoP has been oxidized with the generation of CoOOH and $Ni(OH)_2$. The better cycling stability of NiCoP than that of Ni_2P (10% capacity retention after 1000 cycles) is attributed to the Co hydroxides act as a protective layer that prevents Ni from being oxidized and thus maintains the whole structure.

Three-dimensional TMPs

The effective surface areas between electrode materials and electrolyte can be enlarged and more active sites can be exposed in the electrolyte via increasing the dimensionality. Three-dimension architectures often possess a continuous conductive network for the high-speed electron/ion transfer and abundant voids to alleviate the volume change and self-aggregation during the charge storage process [15]. Rational design of 3D structures and synthesis of novel 3D architectures show new promising for enhancing electrochemical performance. Self-assembly three-dimension nanostructures exhibit high surface area, more active sites and synergistic effects. Three-dimension micro flower-like Ni–Co–P is assembled by crosslinked porous nanoplates as shown in Fig. 12a [95]. The micro flowers assembled by crosslinked thin nanoplates (~70–150 nm) (Fig. 12b and c) provide multi-dimensional channels for ion/electron transport,

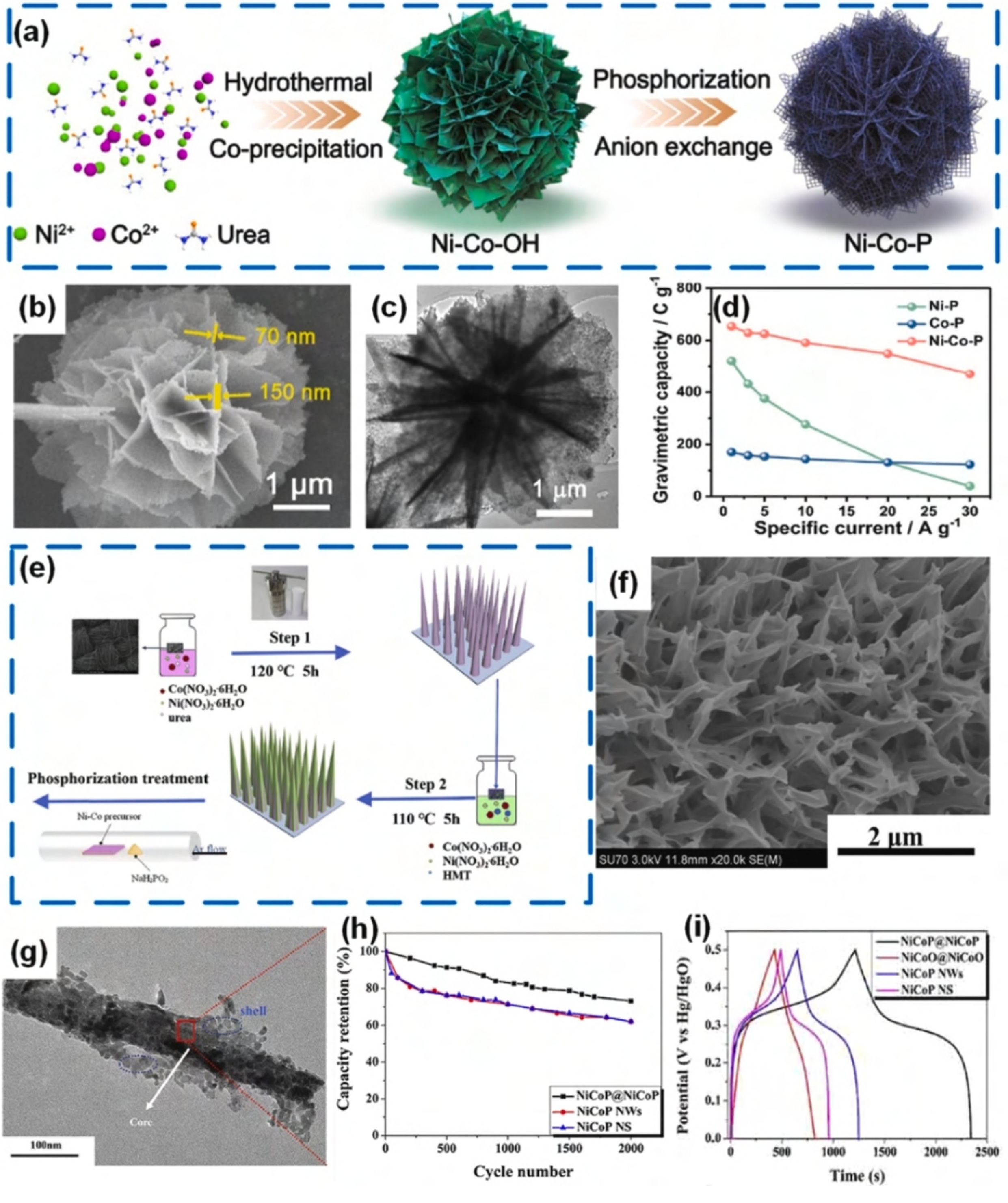

Fig. 12. (a) Schematic fabrication process of micro flower-like NiCoP. (b) SEM and (c) TEM of micro flower-like NiCoP. (d) Rate capability. (e) Schematic fabrication process of 3D NiCoP@NiCoP arrays. (f) SEM picture and (g) TEM image of NiCoP@NiCoP arrays. (h) Cycling stability of three different electrodes. (i) GCD curves of different electrodes. (a–d) Reproduced from ref [95]. Copyright 2020 Elsevier. (e–i) Reproduced from ref [154]. Copyright 2019 Elsevier.

enlarge the electrolyte-electrode interface, ensure sufficient penetration of electrolyte, and enhance the mechanical stability, which contribute to rapid kinetics and long lifespan of Ni–Co–P. The porous structure with large specific surface area (22.97 m^2 g^{-1}) and high pore volume (0.135 cm^3 g^{-1}) provides relatively high accessible area and short ion transport pathway, which significantly improve redox reactions. The Ni–Co–P electrode delivers a specific capacity of 653 C g^{-1} at 1 A g^{-1}, much higher than that of Ni–P (520 C g^{-1}) and Co–P (169 C g^{-1}). Even at a high current density of 30 A g^{-1}, it still shows a capacity of 470 C g^{-1} (Fig. 12d).

The 3D core–shell or hierarchical nanoarchitectures have shown significantly electrochemical improvement due to large surface areas, abundant surface redox reactions and fast transport of ions or electrons [41]. The core acts as both the backbone of core-shell structure and highway for charge transfer. The shell grown on the core would increase the contact area with the electrolyte, leading to

Table 3
Summary of the electrochemical properties of the recent TMPs.

Electrode materials	Nanostructures	Electrolyte	Specific capacity	Rate capability	Retention (cycles)	Ref.
Ni_2P	Nanoplates	3 M KOH	$1032\,C\,g^{-1}$ at $1\,A\,g^{-1}$	$774\,C\,g^{-1}$ at $15\,A\,g^{-1}$	88% (10,000)	[155]
Ni_xP_y	Nanosheets	3 M KOH	$1272\,C\,g^{-1}$ at $2\,A\,g^{-1}$	$814\,C\,g^{-1}$ at $20\,A\,g^{-1}$	90.9% (5000)	[90]
NiP_x	Nanoflakes	6 M KOH	$817\,F\,cm^{-3}$ at $2\,mA\,cm^{-2}$	$434\,F\,cm^{-3}$ at $100\,mA\,cm^{-2}$	NA	[114]
Ni_2P	Nanosheets	6 M KOH	$3496\,F\,g^{-1}$ at $2.5\,A\,g^{-1}$	$1109\,F\,g^{-1}$ at $83.3\,A\,g^{-1}$	NA	[113]
$Ni_{12}P_5$	Nanowires	6 M KOH	$707\,C\,g^{-1}$ at $1\,A\,g^{-1}$	$482\,C\,g^{-1}$ at $10\,A\,g^{-1}$	53% (1000)	[146]
CoP	Nanowires	1 M KOH	$674\,F\,g^{-1}$ at $5\,mV\,s^{-1}$	$214\,F\,g^{-1}$ at $200\,mV\,s^{-1}$	86% (10,000)	[156]
CoP	Nanoparticles	6 M KOH	$447.5\,F\,g^{-1}$ at $1\,A\,g^{-1}$	$314.5\,F\,g^{-1}$ at $10\,A\,g^{-1}$	84.3% (5000)	[111]
Co_2P	Nanoflowers	6 M KOH	$413\,F\,g^{-1}$ at $1\,A\,g^{-1}$	$267\,F\,g^{-1}$ at $10\,A\,g^{-1}$	124.7% (10,000)	[112]
MoP/NPC	Nanosheets	1 M H_2SO_4	$544\,F\,g^{-1}$ at $0.5\,A\,g^{-1}$	$122\,F\,g^{-1}$ at $15\,A\,g^{-1}$	90% (1000)	[157]
Cu_3P	Nanotubes	1 M H_2SO_4	$301\,F\,g^{-1}$ at $2.5\,mV\,cm^{-2}$	$130\,F\,g^{-1}$ at $4.5\,mV\,cm^{-2}$	NA	[115]
NiCoP	Nanoplates	1 M KOH	$194\,mA\,h\,g^{-1}$ at $1\,A\,g^{-1}$	$169\,mA\,h\,g^{-1}$ at $10\,A\,g^{-1}$	81% (5000)	[153]
NiCoP	Nanosheets	2 M KOH	$9.2\,F\,cm^{-2}$ at $2\,mA\,cm^{-2}$	$5.97\,F\,cm^{-2}$ at $50\,mA\,cm^{-2}$	67% (2000)	[158]
NiCoP	Nanosheets	6 M KOH	$2143\,F\,g^{-1}$ at $1\,A\,g^{-1}$	$1615\,F\,g^{-1}$ at $20\,A\,g^{-1}$	73% (2000)	[126]
NiCoP	Nanowalls	2 M KOH	$1861\,F\,g^{-1}$ at $1\,A\,g^{-1}$	$1070\,F\,g^{-1}$ at $10\,A\,g^{-1}$	NA	[159]
NiCoP	Nanorods	1 M KOH	$273\,\mu A\,h\,cm^{-2}$ at $1\,mA\,cm^{-2}$	$234\,\mu A\,h\,cm^{-2}$ at $10\,mA\,cm^{-2}$	82.1% (4000)	[160]
NiCoP	Microspheres	1 M KOH	$761\,C\,g^{-1}$ at $1\,A\,g^{-1}$	$693\,C\,g^{-1}$ at $20\,A\,g^{-1}$	80.0% (5000)	[161]
Zn–Ni–P	Nanosheets	2 M KOH	$384\,mA\,h\,g^{-1}$ at $2\,mA\,cm^{-2}$	$305\,mA\,h\,g^{-1}$ at $50\,mA\,cm^{-2}$	96.45% (10,000)	[91]
Ni–Fe–P	Nanosheets	6 M KOH	$1358\,C\,g^{-1}$ at $5\,mA\,cm^{-2}$	$799\,C\,g^{-1}$ at $50\,mA\,cm^{-2}$	94.7% (10,000)	[92]
CuCoP	Nanospheres	3 M KOH	$1946\,F\,g^{-1}$ at $5\,mA\,cm^{-2}$	$1187\,F\,g^{-1}$ at $150\,mA\,cm^{-2}$	92.7% (7000)	[144]
ZnNiCo-P	Nanosheets	6 M KOH	$958\,C\,g^{-1}$ at $1\,A\,g^{-1}$	$787\,C\,g^{-1}$ at $20\,A\,g^{-1}$	90% (6000)	[129]
Zn–Ni–Co–P	Nanowires	3 M KOH	$1269\,C\,g^{-1}$ at $3\,A\,g^{-1}$	$920\,C\,g^{-1}$ at $20\,A\,g^{-1}$	NA	[133]
C-doped Co-Mn-Fe-P	Nanoflakes	1 M KOH	$4.36\,F\,cm^{-2}$ at $2\,mA\,cm^{-2}$	$2.85\,F\,cm^{-2}$ at $20\,mA\,cm^{-2}$	100% (5000)	[135]
Cu-Co-Ni-P	Nanotubes	6 M KOH	$406\,mAh\,g^{-1}$ at $2\,mA\,cm^{-2}$	$342\,mAh\,g^{-1}$ at $50\,mA\,cm^{-2}$	98.9% (10,000)	[149]
NiCoMoP	Nanosheets	6 M KOH	$508\,F\,g^{-1}$ at $0.2\,A\,g^{-1}$	$433\,F\,g^{-1}$ at $1\,A\,g^{-1}$	NA	[134]

sufficient redox reaction, and help to alleviate the structural damage caused by volume change during the cycling test, resulting in an improved cycling stability [62]. Fig. 12e shows the NiCoP@NiCoP core-shell arrays directly grown on carbon cloth via a two-step hydrothermal method and phosphorization treatment [119]. The core-shell nanoarrays shorten the ionic diffusion distance from the external electrolyte to the interior core, and the outer ultrathin NiCoP nanosheets improve the contact area with the electrolyte and facilitate the infiltration of OH^- and charge transfer (Fig. 12 f and g). The NiCoP@NiCoP arrays exhibit a higher specific capacity of $1125\,C\,g^{-1}$ ($312\,mAh\,g^{-1}$) at $1\,Ag^{-1}$ and better cycling stability with 71.8% retention after 2000 cycles than single NiCoP nanowires and NiCoP nanosheets (Fig. 12h and i). Table 3 summarizes the recent representative TMPs electrode materials for HSCs applications.

Strategies for the improvement of TMP electrodes

Although pristine TMPs exhibit outstanding physicochemical properties, their practical applications for HSCs are still limited by some shortcomings: 1) the volume expansion leads to poor cycling stability, 2) sluggish reaction kinetics of active materials hinder capacity as well as rate capability [96], 3) unstable phase is easy to be formed in strong alkaline electrolytes, such as metal hydroxides, 4) oxygen evolution reaction often occurs on the electrode surface. Therefore, staggering voltage hysteresis, side reactions and volume expansion are some serious issues that need to be addressed [49]. Herein, we summarize four effective strategies that can significantly improve the specific capacity, rate capability, and cycling stability of TMPs for HSCs, including 1) optimizing synthesis processes, 2) doping elements, 3) tuning composition, and 4) designing composites.

Synthesis design

Most of TMPs are fabricated by annealing precursors (hydroxides or oxides) in inter gas using NaH_2PO_2 as the phosphorus source [99,162,163]. The annealing temperature, annealing time, and P source dosages could have different effects on the nanostructures and composition of electrode materials, which in turn determine the electrochemical properties [98,111].

Some TMPs nanostructures consist of enormous interconnected nanoparticles, which could be attributed to the release of CO_2 and H_2O during the heat treatment of precursor [164]. Annealing temperate has a crucial effect on the growth and crystalline of particles. The low annealing temperature may decrease the crystalline, while a high temperature could result in the aggregation of nanoparticles, reducing the surface areas. Fig. 13a-c illustrate the morphologies of Ni-Fe-P nanosheets phosphatized at different temperatures [92]. At a low temperature (300 °C), few small pores appeared on the nanosheets because of the decomposition of the precursors. With the increasing temperature, the pores became larger due to the grain growth process accompanied by the growth of pores and the phase transition process from Ni–Fe LDH to Ni-Fe-P [153]. The porous structures possess micropores, mesopores, and macropores at the different annealing temperature. The Ni–Fe–P-350 nanosheets possess a superior specific surface area of $75\,m^2\,g^{-1}$ in comparison with that of Ni–Fe–P-300 ($61\,m^2\,g^{-1}$) and Ni–Fe–P-400 ($65\,m^2\,g^{-1}$), providing more efficient paths for the ion/electron transmission and effective contact between electrode and electrolyte. The Ni–Fe–P-350 electrode delivers a highest capacity of $1358\,C\,g^{-1}$ at $5\,mA\,cm^{-2}$, which is higher than other two metal phosphide electrodes.

The phosphating process is a gas-solid reaction. During this process, a hollow structure could be formed due to unequal ions diffusion rate which is described as the nanoscale Kirkendall effect [140]. The nanoscale Kirkendall effect can be divided into three types including gas-solid, liquid-solid and solid-solid processes [165]. In the gas-solid process, the solid component that acts as the precursor is exposed in a flowing gas. When the reactants from the gas phase react with atoms/ions on the precursor surface, a new layer of the reaction product is formed on the surface [166]. This new layer works as a barrier to restrict the inward diffusion of the reactants from the gas. If this barrier layer is in favor of the outward diffusion of the solid core, hollow nanostructures will finally form with the solid core gradually decreased [167]. For example, the formation mechanism of hollow-structured NiCoP nanorods is shown in Fig. 13d [160]. At the beginning of the phosphating process, a thin layer of NiCoP is formed on the surface due to the reaction of $NiCo_2O_4$ and PH_3. The NiCoP layer acts as a barrier for the reaction of PH_3 with $NiCo_2O_4$. Meanwhile, the Ni and Co ions move outwardly to react with phosphorus, producing many voids in the center of nanorods and resulting in the formation of hollow nanorods. The

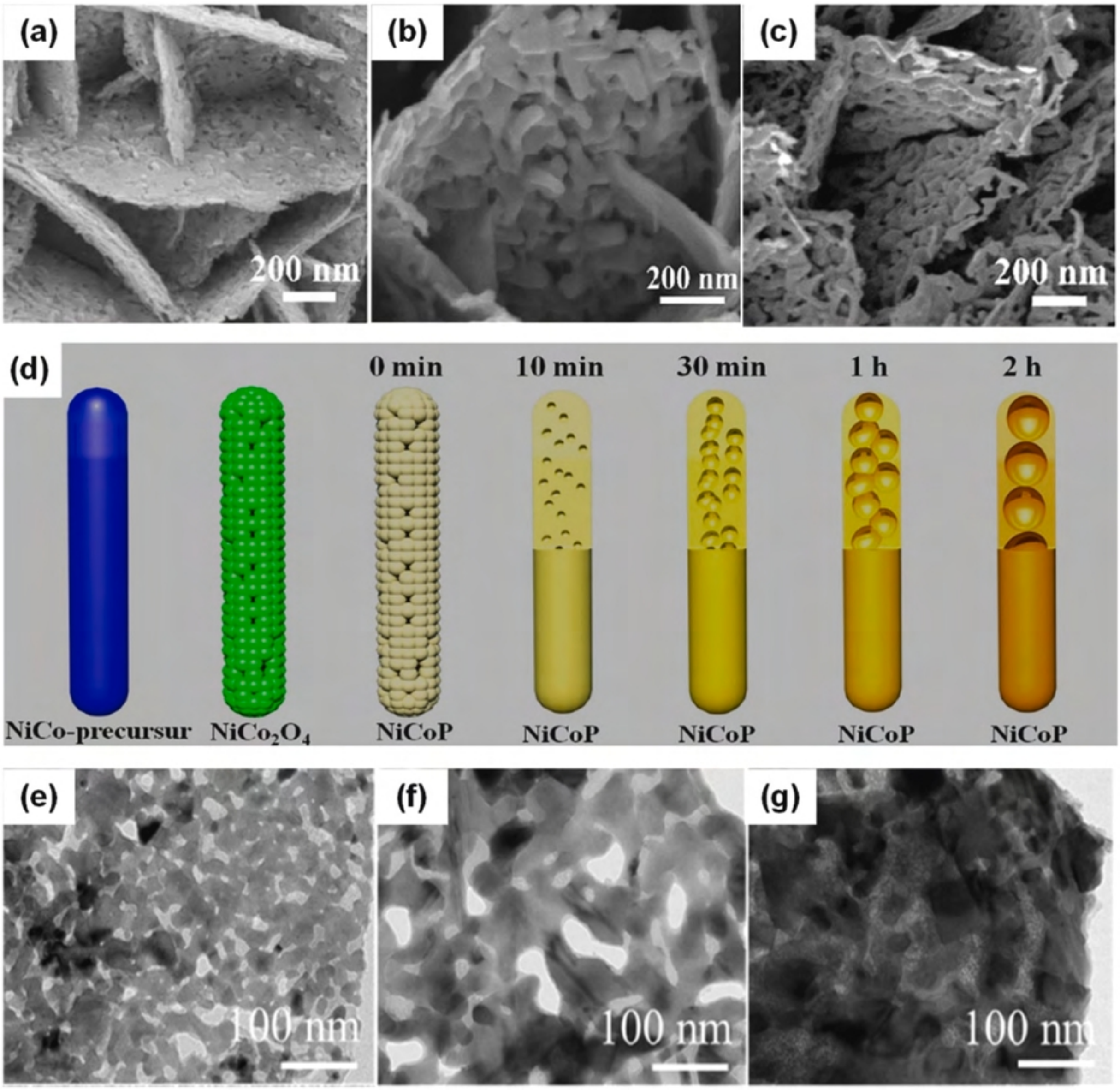

Fig. 13. SEM images of (a) Ni–Fe–P-300, (b) Ni–Fe–P-350 and (c) Ni-Fe-P-400 networks. (d) Schematic illustration of the formation mechanism of hollow NiCoP nanorods. (e-g) TEM images of the Ni_xP_y nanosheets phosphatized by different amounts of phosphorus source.
(a–c) Reproduced from ref [92]. Copyright 2019 Royal Society of Chemistry. (d) Reproduced from ref [160]. Copyright 2020 Elsevier. (e–g) Reproduced from ref [90]. Copyright 2017 American Chemical Society.

hollow NiCoP nanorods exhibit a capacity of 273.4 μAh cm^{-2} at a current density of 1 mA cm^{-2}, higher than that of NiCo-precursor (190.4 μAh cm^{-2}), and $NiCo_2O_4$ (209.3 μAh cm^{-2}). The enhanced specific capacity is attributed to the hollow nanorods providing large electrode/electrolyte contact area, more active sites and shorten charge transport channel. After 4000 cycles, the NiCoP nanorods maintain 82% of its initial capacity because the hollow structure could accommodate the volumetric change during cycling test.

Vacancies can be introduced by adjusting the content of P source in the phosphorization process, which produce more active sites and increase surface reactivity, resulting in the enhanced capacity [168]. For example, the introduction of oxygen vacancies into $CoMoO_4$ crystal lattices by using different P source dosages shows an improved electrochemical property. After the oxygen vacancies are introduced, the P-$CoMoO_{4-x}$-3 shows higher electrical conductivity (3.9×10^{-2} S m^{-1}) than pristine $CoMoO_4$ (5.7×10^{-3} S m^{-1}), which facilitates electron transport, resulting in fast reaction kinetics [124]. In addition, P incorporation decreases the Co–O bond energy, resulting in high surface redox activity, and forms Mo ions with lower valence state (Mo^{5+} or Mo^{4+}), increasing redox reaction species. The P-$CoMoO_{4-x}$-3 exhibits a higher specific capacity of 1368 C g^{-1} at 2 A g^{-1} than that of pristine $CoMoO_4$ (651 C g^{-1}). The obtained capacity exceeds the theoretical Faradaic capacity value, which is possibly attributed to the P-$CoMoO_{4-x}$ nanostructure contributing to both Faradaic and non-Faradaic processes. The structure and morphology also reflect the effect of the amount of P source. With the increase of phosphorus source, the interconnected nanoparticles show an increase in size and the interspace between nanoparticles was blocked gradually as shown in Fig. 13e-g, which may originate from the lattice expansion to form Ni_xP_y [90]. The Ni_xP_y-2 nanosheets exhibit a specific capacity of 1272 C g^{-1} at 2 A g^{-1} and excellent cycling stability (90.9% after 5000 cycles) due to the large surface-to-volume ratio and the abundant interspace between the interconnected particles, which provide abundant active sites and

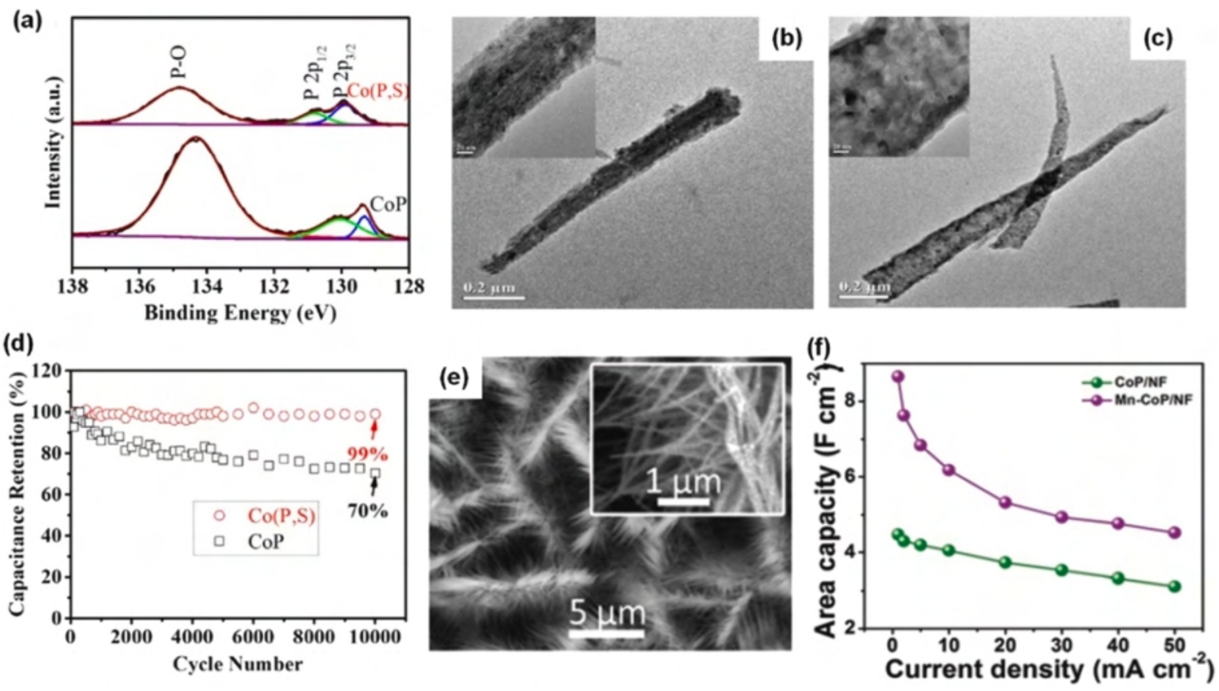

Fig. 14. (a) High-resolution XPS spectra of P 2p of CoP and Co(P,S) nanoarrays. SEM images of (b) CoP nanowires, (c) Co(P,S) nanotubes. (d) Cycling stability of CoP and Co(P,S) nanoarrays. (e) SEM pictures of Mn-CoP/NF. (f) Areal capacity of CoP/NF and Mn-CoP/NF electrodes at different current densities.
(a–d) Reproduced from ref [171]. Copyright 2017 Elsevier. (e,f) Reproduced from ref [120]. Copyright 2018 Royal Society of Chemistry.

accommodate the volumetric expansion. After repeated charge/discharge, the initial structure can be maintained except for a slight aggregation, resulting in the degradation of capacity to some extent.

Elemental doping

Doping is an effective way to improve the rate capability and cycling stability of electrode materials because foreign atoms could change the physical and chemical character of original materials, such as nanostructures and the strength of chemical bonds, and introduce defects as well as rebuild electron density, which could enhance the ionic or electronic conductivity and increase electrochemically active sites, enabling fast redox reaction kinetics [169,170]. The elemental doped TMPs could be divided into anions doped TMPs (O, S, Se ions, etc), cations doped TMPs (Mo, Mn, Fe, Zn ions, etc) and anions and cations dual-doped TMPs. For example, after the introduction of sulfur into the CoP, the P to P-O ratio is increased as shown in Fig. 14a, leading to the decrease of surface passivation layers of CoP and the increase of metallicity of Co, which could increase the conductivity [171]. The porous nanowires in CoP are converted into nanotube structures in sulfur-doped CoP (Fig. 14b and c). The formation mechanism of nanotubes could be explained by the nanoscale Kirkendall effect as mentioned before. S^{2-} first reacts with CoP to form a thin layer of Co(P,S) on the surface. The Co (P,S) layer could restrict outward S^{2-} reacting with the inward CoP. As the CoP core moves outwardly to react with S^{2-}, voids are formed at the center of the nanowire, resulting in the formation of Co(P,S) nanotubes. The Co(P, S) nanotubes show a higher specific capacity of 296 $mA\,h\,g^{-1}$ at 1.0 $A\,g^{-1}$ than CoP (166 $mAh\,g^{-1}$) due to the increased active sites by S ion and short electron transfer pathway of nanotube structure. The Co(P, S) nanoarrays illustrate excellent cycle stability with 99% capacity retention after 10,000 cycles, which is much better than CoP alone (70% after 10,000 cycles) (Fig. 14d). After cycling test, CoP is largely converted to CoOOH, leading to the reduction of conductivity. In contrast, most Co(P, S) phase can be well preserved, indicating improved cycling performance after the introduction of S. Beyond anion doping, cations doping, such as Mn-doped cobalt phosphide nanowires, has also been investigated [120]. The morphology of the nanowire grown on nanosheet arrays can be observed in Mn-CoP (Fig. 14e), while only nanowires are found in CoP. This is because Mn incorporation is in favor of the generation of the Co(OH)F nanosheets. As a result, the Mn–Co(OH)F nanosheets are firstly grown on the Ni foam. Due to a small number of Mn ions, the nanowires are formed subsequently and grown on the surface of the nanosheets. Mn–CoP exhibits a superior areal capacitance of 8.66 $F\,cm^{-2}$ at 1 $mA\,cm^{-2}$, which is ~2 times higher than that of CoP (Fig. 14f). In another system, Zn ions and S ions are introduced into Ni–P nanosheets together [172]. The Zn doping could improve electrical conductivity, accelerate electron transmission and promote redox kinetics due to the high chemical activity of Zn and the narrow band gap. The strong interactions between the new phase of Ni_3S_2 and intrinsic Ni_2P optimize the electronic structure to facilitate electrons transfer and enhance reaction activity. The values of Rct for ZNPS, ZNP and ZNS are 0.09, 0.13 and 0.12, respectively, suggesting that ZNPS electrode shows enhanced reaction kinetics and electrical conductivity compared with ZNP and ZNS. The ZNPS nanosheets demonstrate a specific capacity of 1180 $C\,g^{-1}$ at 2 $A\,g^{-1}$ and maintain high capacity of 780 $C\,g^{-1}$ at 20 $A\,g^{-1}$.

Composition tuning

Controlling the ratio of different elements is an effective strategy to tune the composition of electroactive materials away from stoichiometry [86,100]. Adjusting different metal ions with an appropriate ratio can increase the number of electronic states near the Fermi level and promote Faradaic charge transfer, thus increasing the capacity [68]. Additionally, the cyclic stability could achieve considerable improvement because the structure could avoid collapse and aggregation during the charge storage process by making full use of the characteristics of different metal ions [67,173]. For nickel cobalt phosphides, the ratio of Ni/Co has a significant effect on the specific capacity and cycling stability [174]. The molar ratio of Ni^{2+} and Co^{2+} can be adjusted because of the similar solubility constant (K_{sp}) of $Co(OH)_2$ (2.5×10^{-16}) and $Ni(OH)_2$ (2.8×10^{-16}) at

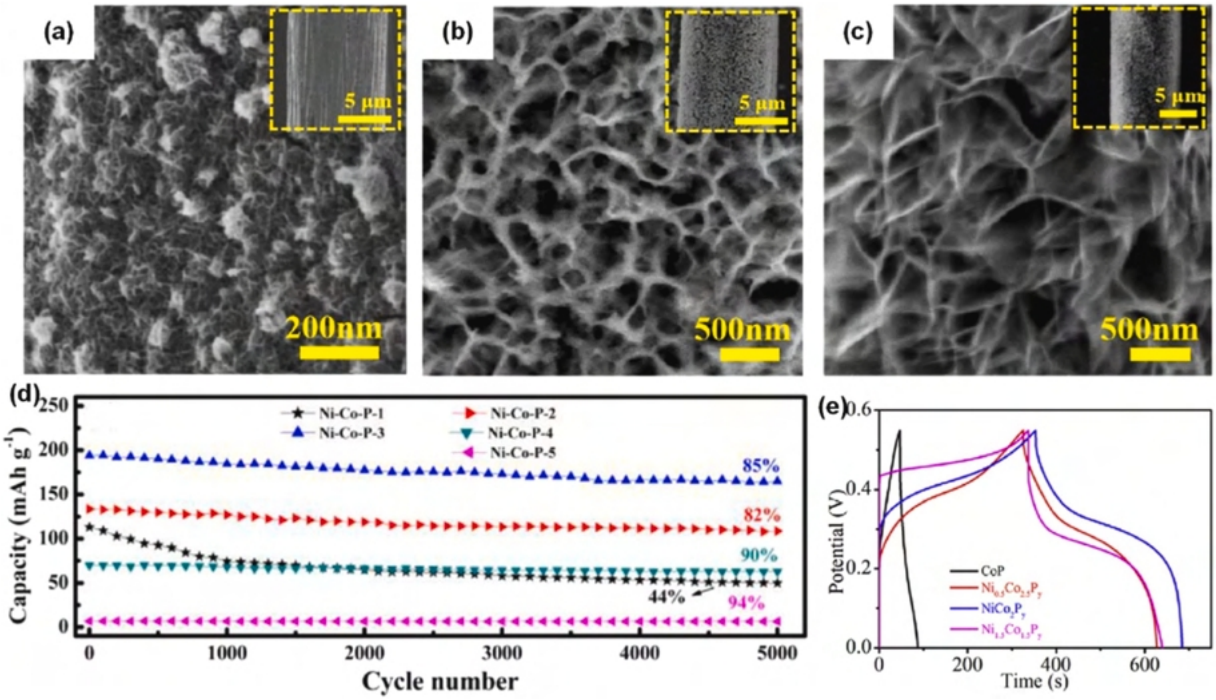

Fig. 15. SEM images of (a) Ni-Co-P-1, (b) Ni-Co-P-3, (c) Ni-Co-P-5. (d) Cycling stability of five electrodes. (e) GCD curves at current density of 3 A g^{-1}.
(a–d) Reproduced from ref [110]. Copyright 2020 Elsevier. (e) Reproduced from ref [174]. Copyright 2019 Elsevier.

25 °C [110]. As shown in Fig. 15a-c, the interconnected Ni-Co-P nanosheets provide abundant interspaces for the diffusion of electrolyte and active sites for redox action. The size and thickness of nanosheets are increased with the increase of cobalt content, which result in large surface areas and good structural stability [110]. The thin and rough Ni-Co-P-1(Ni_2P) nanosheets show a high specific capacity of 125 mA h g^{-1}, while the Ni-Co-P-5 (CoP) nanosheets exhibit excellent cycling stability (94% after 5000 cycles) (Fig. 15d). The Ni-Co-P-3 nanosheets with optimal Ni/Co ion ratio provide a higher specific capacity of 213 mA h g^{-1} than that of Ni-Co-P-5 and better cycling performance (85% after 5000 cycles) than Ni-Co-P-1 because of the electron interaction between Ni_2P and CoP as well as the full integration of advantages of Ni_2P and CoP. A similar change of electrochemical performance can be observed in $NiCo_2P_y$ nanoneedle arrays [174]. The discharge time becomes longer with the increase of Ni/Co ratio and reaches up to the maximum value of $NiCo_2P_y$ due to the enhanced electrical conductivity. As the Ni/Co ratio is further increased, the discharge time decreases, which could be attributed to the increased charge transfer resistance (Fig. 15e).

Composites exploration

Designing composite materials has been regarded as an effective strategy to improve the property of matrix materials. Composites not only own the advantages of different components, but also achieve the synergistic (1 + 1 > 2) performance [175]. Moreover, the interfaces between different components possess a large number of defects, which provide abundant active sites for redox reaction. The composites design should consider the following principles, including 1) high specific surface area and desirable electroactive sites, which are related to the specific capacity, 2) high electronic conductivity, which is beneficial to the rate capability, 3) high thermal stability and chemical stability, which are crucial to the cyclic stability [176]. In this section, composite materials based TMPs are classified into four types: 1) TMPs and carbon-based materials composites, 2) TMPs and conductive polymers composites, 3) TMPs and transition metal hydroxides composites, 4) TMPs and transition metal sulfides/selenides composites.

TMPs and carbon-based materials composites

Carbon-based materials, such as amorphous carbon, graphene and carbon nanotubes, have been extensively adopted to improve the performance of electrode materials [13,177,178]. Carbon-based materials possess high electrical conductivity and good chemical stability, which are in favor of fast charge transportation and storage, protecting the whole structure and thus enhancing the cycling performance [147,179]. To fabricated amorphous carbon coating electrode materials, the as-synthesized sample is dipped in the glucose solution and subsequently put into a tube furnace by carbonization in inert gas at high temperature [179,180], and the synthesized carbon layer is ultrathin as shown in Fig. 16a [181]. After coating amorphous carbon, NiCoOP@C showed a high specific capacitance of 2638 F g^{-1} and excellent cycling stability (increased from 57% to 84% after 3000 cycles) (Fig. 16b) [178]. The enhanced cycling performance can be attributed to the increased mechanical strength by the efficient coating of the carbon layer. Beyond the carbon layer, carbon nanoparticles could also provide sufficient active sites, shorten the ion transfer path and prevent the mechanical distortion through filling the interspaces of nanoarrays. Fig. 16c shows that carbon nanoparticles are deposited on the 3D porous nickel phosphides nanosheets and fill the voids between nanosheets. Due to the incorporation of carbon particles, the Ni_2P-C shows a higher surface area of 29.7 m^2 g^{-1} than Ni_2P (17.7 m^2 g^{-1}), increasing active sites and accessibility of electrolyte ions, thereby leading to an enhanced specific capacity of 498 mAh g^{-1}. In addition, owing to the suspending carbon nanoparticle, which alleviates the volume change of Ni_2P nanoarrays, the capacity retention was increased from 80% to 94% compared to pristine Ni_2P nanoarrays after 2000 cycles (Fig. 16d).

One-dimensional carbon nanotubes (CNTs) are also used to improve the electrochemical performance due to the excellent electronic and mechanical properties [182]. Fig. 16e shows the synthesis process of the novel NiCoP nanoflake-surrounded CNT nanoarrays, in

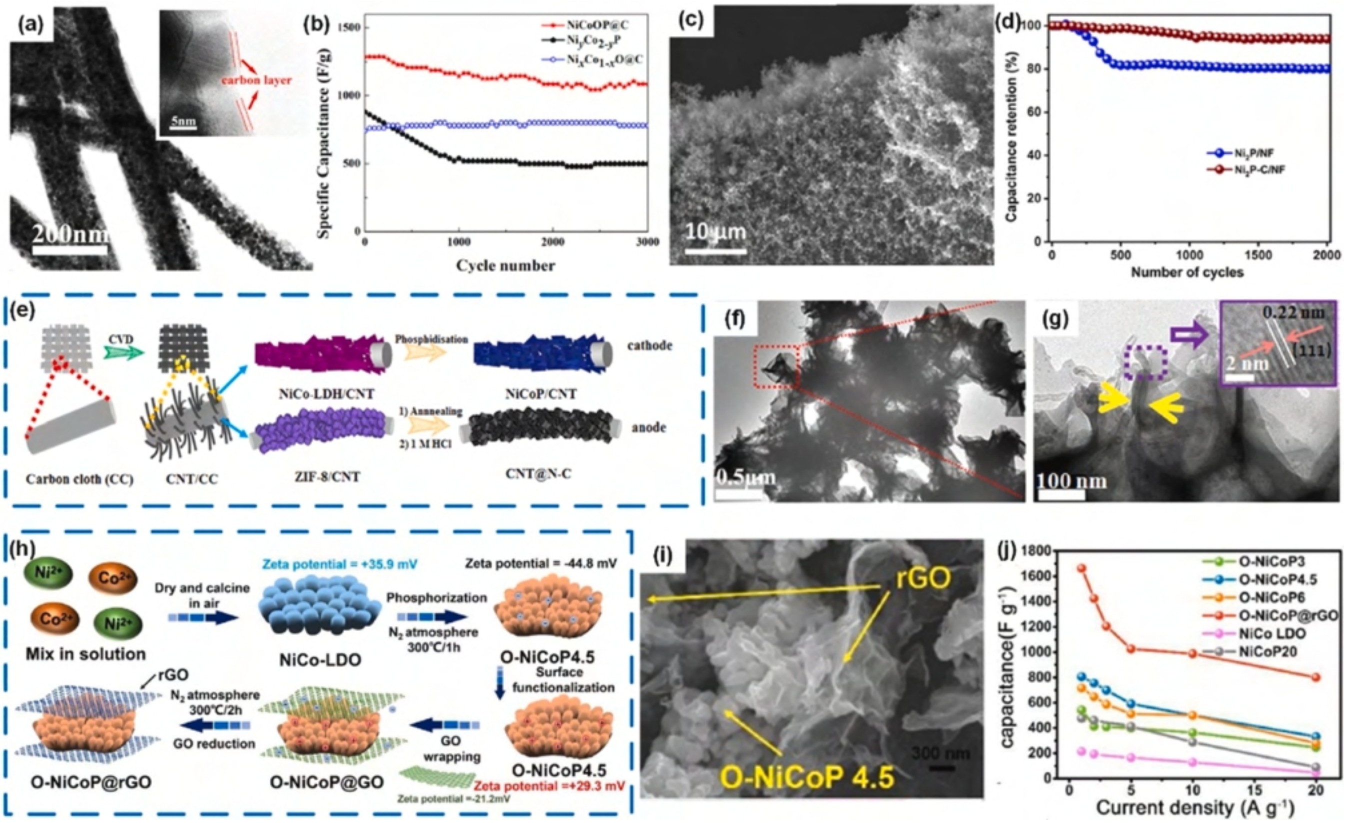

Fig. 16. (a) TEM images of NiCoP@C NAs. (b) Cycling stability. (c) SEM image of Ni_2P-C. (d) Cycling stability. (e) Schematic illustration for the synthesis of NiCoP/CNT/CC and CNT@N-C/CC. (f and g) TEM images of NiCoP/CNT/CC. (h) Schematic illustration for the synthesis of O-NiCoP@rGO. (i) TEM images. (j) Rate capability.
(a) Reproduced from ref [181]. Copyright 2019 Elsevier. (b) Reproduced from ref [178]. Copyright 2016 American Chemical Society. (c, d) Reproduced from ref [186]. Copyright 2019 American Chemical Society. (e–g) Reproduced from ref [183]. Copyright 2020 Elsevier. (h–j) Reproduced from ref [168]. Copyright 2020 Elsevier.

which CNT nanoarrays are helpful to improve the electrical conductivity and provide extra electron transfer channels [183]. In addition, CNT network provides enlarged specific surface area for the growth of NiCoP nanoarrays, which ensures the enhanced cyclic stability (Fig. 16f and g). The NiCoP/CNT delivers a high specific capacity of 215.6 mA h g^{-1} at 5 mA g^{-1} and an outstanding rate performance (57.4% of the original capacity at a current density of 30 mA g^{-1}). In another study, the nanostructured Ni-CoP@C were anchored on the surface of CNTs to promote effective electron transfer [177]. Due to the existence of CNTs, a crosslinked conductive network was built to shorten the ions transfer paths. The amorphous carbon in the Ni-CoP@C ensured a close and strong contact between Ni-CoP@C and CNTs. Thus, the interconnected Ni-CoP@C@CNTs show better specific capacitance and rate capability compared to Ni-CoP@C.

Two-dimensional reduced graphene oxide (RGO) has huge application prospects in energy storage, owing to its unique physical and chemical properties such as large surface area, superior electronic properties and excellent mechanical stability [184]. The electrode combining graphene sheets with Ni_2P exhibited a higher specific capacitance of 1912 F g^{-1} at 5 mA cm^{-2} than that of Ni_2P (1568 F g^{-1}) and the capacitance retention was increased from 68.8% to 77.1% [185]. The improved electrochemical performance is due to the GS matrix with high electrical conductivity which can host the nanosized Ni_2P and enable nanosized Ni_2P well exposed to the electrolyte, leading to fast electron and ion transfer. The Ni_2P nanoparticles on the surface of GS act as spacer to prevent the restacking of sheets, avoiding the loss of active surface. The O–NiCoP materials modified with PDDA to achieve positive Zeta potential are combined with GO nanosheets with negative surface charge via a facile self-assembly way in solution to synthesis O–NiCoP@rGO composites (Fig. 16h) [168]. The surface area of O–NiCoP@rGO has been increased dramatically from 23.4 m^2 g^{-1} to 284.4 m^2 g^{-1}. The active charge transfer in the composite is significantly promoted because more charge can be found near graphene that confirms the improved electrical conductivity with the introduction of rGO. When the current density is increased from 1 A g^{-1} to 20 A g^{-1}, the specific capacitance of O–NiCoP@rGO decreases from 1663 F g^{-1} to 800 F g^{-1}, indicating a good rate capability, which is attributed to the conductive network of rGO (Fig. 16i and j). After 3000 cycles, the capacitance retention of O–NiCoP@rGO is increased from 43.8% to 84.1% compared to O–NiCoP due to the excellent mechanical stability of rGO.

TMPs and conductive polymers composites

In the TMPs/conductive polymers composite materials, conductive polymers coating is applied to improve the electrical conductivity and mechanical stability, which in turn promotes electrode kinetics and stabilizes the structure of TMPs, respectively [187]. Conductive polymers can not only be coated on the surface of nanoarrays, but also interconnect the neighboring nanoparticles to improve the whole electrical conductivity and ion diffusion ability [188]. For example, the thin PEDOT layer is coated on the surface of FeP nanorods without destroying the structure via an in-situ polymerization method (Fig. 17a and b)[189]. The FeP/PEDOT electrode shows a lower Rct of 5.8 Ω compared to that of FeP electrode (7 Ω), which demonstrates that the highly conductive PEDOT coating would promote the charge transfer in the electrode/electrolyte interface and improve the electrode conductivity, resulting in the enhanced capacitance. The pristine FeP nanoarrays exhibit poor stability of only 24% retention after 5000 cycles. After PEDOT coating, the stability can be greatly increased up to 82% because

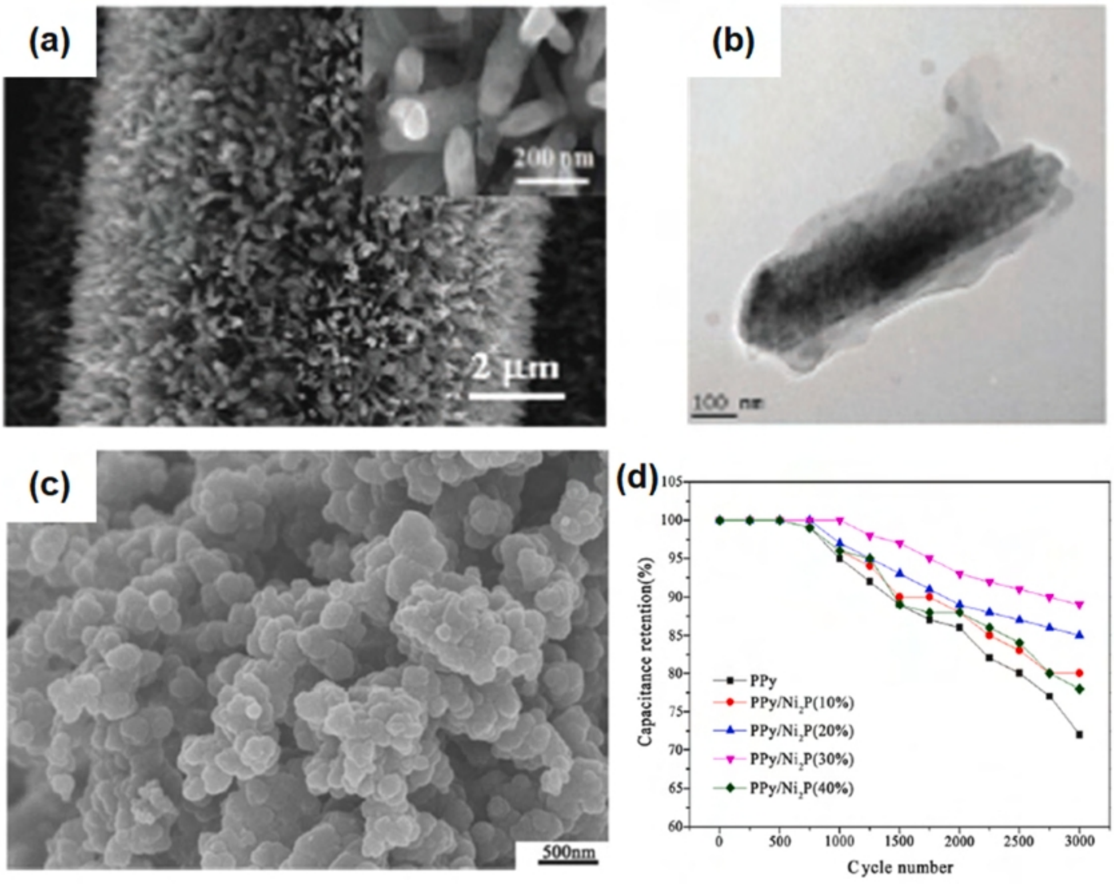

Fig. 17. (a) SEM and (b) TEM images of FeP/PEDOT nanorod. (c) SEM image of PPy/Ni_2P. (d) Cycling performance.
(a, b) Reproduced from ref [189]. Copyright 2018 Royal Society of Chemistry. (c, d) Reproduced from ref [191]. Copyright 2019 Springer Nature.

PEDOT serving as a protection layer to enhance the mechanical stability of FeP nanorods. Apart from PEDOT, PPy has high electrical conductivity (10–100 S cm^{-1}), which can undoubtedly improve electron transport in TMPs [190]. PPy/Ni_2P was prepared via a facile polymerization reaction in which Ni_2P particles were uniformly dispersed on the surface of PPy (Fig. 17c) [191]. The strong interaction between PPy and Ni_2P facilitates ion diffusion and the pore structure provides large surface areas for fast charge transfer. PPy/Ni_2P (30%) composite delivers a discharge capacitance of 477 F g^{-1} at a current density of 1 Ag^{-1}. Comparing the cycling stability of different electrodes, PPy/Ni_2P (30%) composite maintains about 89% of its initial capacitance after 3000 cycles (Fig. 17d) because the Ni_2P nanoparticles prevent the expansion and shrinkage of PPy.

TMPs and transition metal hydroxides composites

Transition metal hydroxides are promising electrode materials because of their low cost, abundance and high theoretical specific capacity [192]. The layered transition metal hydroxides can enlarge specific surface areas significantly and facilitate the ion diffusion from electrolytes to active materials, resulting in a high specific capacity [193]. Many transition metal hydroxides, such as α-$Ni(OH)_2$, β-$Ni(OH)_2$ and $Co(OH)_2$ [194–196], have been employed to enhance the ability of electric energy storage. Fig. 18a shows that the $Ni(OH)_2$ nanosheets are directly gown on the NiCoP@C nanowires and nanoflakes uniformly [181]. The NiCoP@C@$Ni(OH)_2$ nanoarrays deliver a higher specific capacitance of 2300 F g^{-1} at 1 A g^{-1} and better rate capability with 72% retention at 20 A g^{-1} than those of NiCoP@C (Fig. 18b). The enhanced electrochemical performance is attributed to ultrathin $Ni(OH)_2$ nanosheets which provide numerous active sites for redox reactions and make it easy for the diffusion of electrolyte. The $Co(OH)_2$ nanosheets were grown on NiCoP nanoarrays via hydrothermal method because $Co(OH)_2$ possesses high theoretical capacitance (3460 F g^{-1}) and controllable structure [197]. The ultrathin $Co(OH)_2$ nanosheets possess narrow bandgap and enhanced electrical conductivity due to the much increased density-of-states near the Fermi level [194]. As shown in Fig. 18c, the interconnected $Co(OH)_2$ nanosheets form plentiful voids, which contribute to short ion-transport pathways and effective electrolyte accessibility. The NiCoP/$Co(OH)_2$ nanoarrays show a high specific capacity of 304 mA h g^{-1} at 1 A g^{-1} compared with 230 mA h g^{-1} of NiCoP (Fig. 18d).

In addition, transition metal layered double hydroxides (LDHs) with a general formula of $[M^{II}_{1-x}M^{III}_{x}(OH)_2]^{x+}[A^{n-}]_{x/n}\cdot mH_2O$, where M^{II} and M^{III} are divalent and trivalent metal cations, and A^{n-} represents the charge balancing anions [198–200], have been chosen to synthesize composites with TMPs. The specific capacity and rate capability could be improved because of the large surface area, special layered structure and tunable element composition of LDHs, which could expose abundant electroactive sites and accelerate ion/electron transport [65]. Moreover, the inherent high stability of LDHs can accommodate the volume expansion during the repeated charging/discharging process, thus enhancing the cycling stability of matrix materials [201]. For instance, FeNiP nanosheets act as a second substrate for the growth of CoNi-LDH to form the nanosheet on nanosheet hybrid (Fig. 18e) [202]. The two organized nanosheets provide plentiful voids between the interconnected nanosheets, which provide more active sites for the redox reactions, offer enough space for the diffusion of electrolyte, and accommodate the volume change. The specific capacitance of FeNiP@CoNi-LDH nanosheets could reach up to 2280 F g^{-1} at 1 A g^{-1}, and the electrode shows good

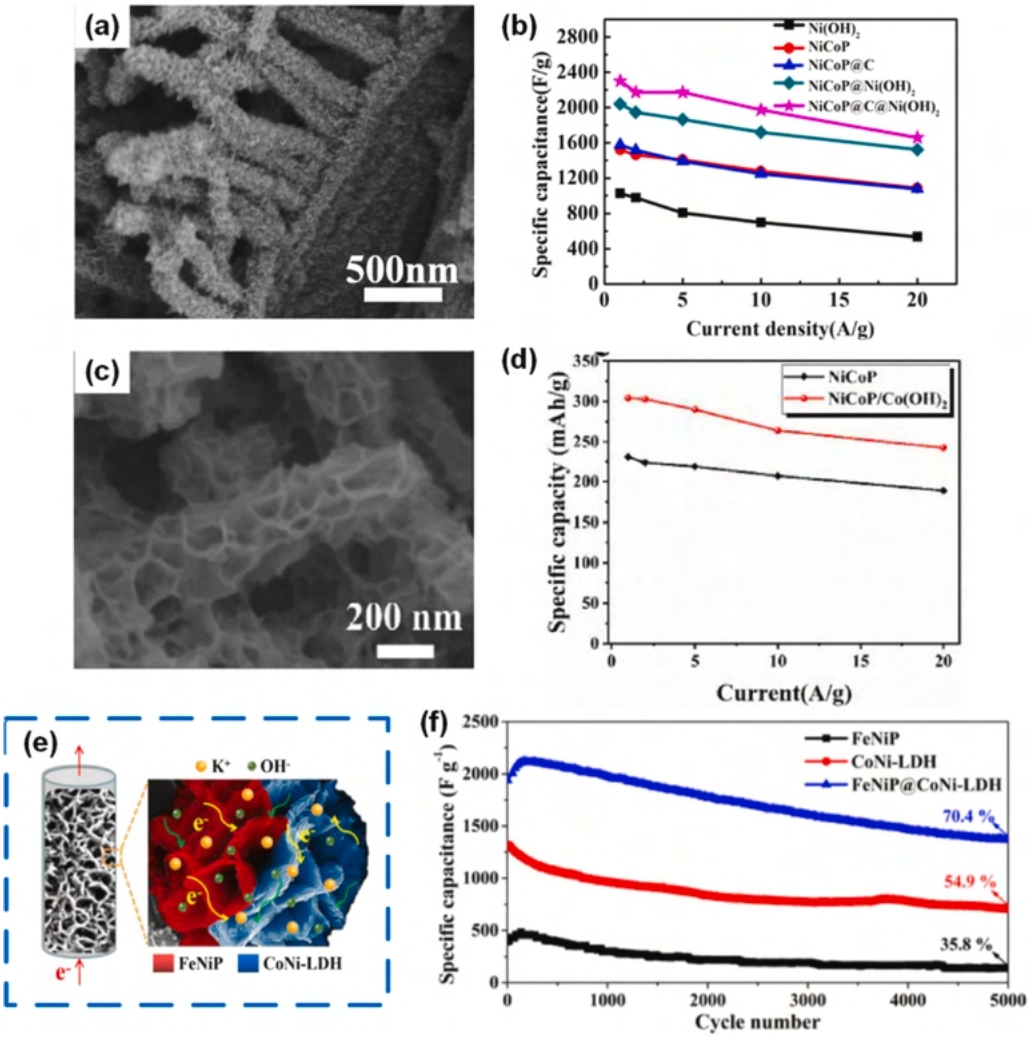

Fig. 18. (a) SEM image of NiCoP@C@Ni(OH)$_2$ NAs. (b) Rate capability. (c) SEM picture of NiCoP@Co(OH)$_2$ NAs. (d) Specific capacities at different current densities. (e) Schematic of charge transport of the FeNiP@CoNi-LDH nanosheets. (f) Cycling performances at 5 A g^{-1}.
(a, b) Reproduced from ref [181]. Copyright 2019 Elsevier. (c, d) Reproduced from ref [194]. Copyright 2019 Elsevier. (c) Reproduced from ref [202]. Copyright 2020 Elsevier.

cycling stability (70.4% of the initial capacitance after 5000 cycles) compared to FeNiP (35.8%) and CoNi-LDH (54.9%) (Fig. 18f), due to the electrochemical activity and good stability of CoNi-LDH coating layer. In addition, other LDHs, such as NiMn LDH [203], NiFe LDH [204] and CoAl LDH [205], have also been reported to improve the electrochemical performance of TMPs.

TMPs and transition metal sulfides/selenides composites

Beyond hydroxides, transition metal sulfides can also be used to design composites with TMPs, due to their large theoretical capacity (~1000 mA h g^{-1}), high electric conductivity, high electrochemical activity, and rich redox reactions [64,206]. In addition, they have a narrow band gap during anion exchange reactions, which could enhance the electron transport efficiency compared to transition metal hydroxides [207,208]. For example, the well-designed interconnected NiCo$_2$S$_4$ nanosheets coating on NiFeP nanosheets provide abundant open pore channels and accessible 2D surface, which could facilitate the electrolyte ion/electron transfer and alleviate the volume expansion of electrode material during repeated charging/discharging test [209]. The movements of Ni *2p* and Co *2p* peaks indicate the strong chemical bond between NiFeP nanosheets and NiCo$_2$S$_4$ nanosheets, which might promote charge transfer at the interface and improve electrical conductivity. The NiFeP@NiCo$_2$S$_4$ electrode shows a high specific capacity of 874 C g^{-1} at a current density of 1 A g^{-1}, which is 3.4 times of pristine NiFeP nanosheets (Fig. 19a). After 5000 charging/discharging cycles at 5 A g^{-1}, NiFeP@NiCo$_2$S$_4$ exhibits capacity retention of 85.6%, higher than that of NiFeP (64.9%) and NiCo$_2$S$_4$ (67.8%), due to the stable heterostructure (Fig. 19b). NiVS/NiCuP/CW was synthesized by electrodeposition and hydrothermal method in which the NiVS nanoparticles were grown on the NiCoP film [210]. The oxidation and reduction diffusion coefficients for NiCuP/CW are 1.7×10^{-5} and 1.4 × 10^{-5} cm^2 s^{-1} and for c-NiVS/NiCuP/CW are 2.39 × 10^{-5} and 2.52 × 10^{-5} cm^2 s^{-1}, respectively (Fig. 19c). The higher diffusion coefficients for c-NiVS/NiCuP/CW indicate the faster OH$^-$ ion mobility, which results in fast redox reactions. According to the Trasatti analysis, the charges stored on the inner and outer surfaces are 18.5 C cm^{-2} and 2.8 C cm^{-2}, respectively, indicating abundant active sites in the inner surfaces of c-NiVS/NiCuP/CW. The c-NiVS/NiCuP/CW electrode shows a specific capacitance of 13.4 F cm^{-2} at 4 mA cm^{-2}, which is higher than that of NiV-LDH/NiCuP/CW (11.9 F cm^{-2}), NiCuP/CW (3.8 F cm^{-2}) and c-NiVS/CW (0.6 F cm^{-2}). Even at a high current density of 80 mA cm^{-2}, a high specific capacitance retention of ~70% can be obtained for c-NiVS/NiCuP/CW (Fig. 19d).

Selenides, similar to sulfides, possess excellent electrical conductivity and electrochemical activity due to the weak metal-selenium bonding and narrow band gap [211]. Layer MoSe$_2$ nanosheets are studied for energy storage due to the large interplanar spacing,

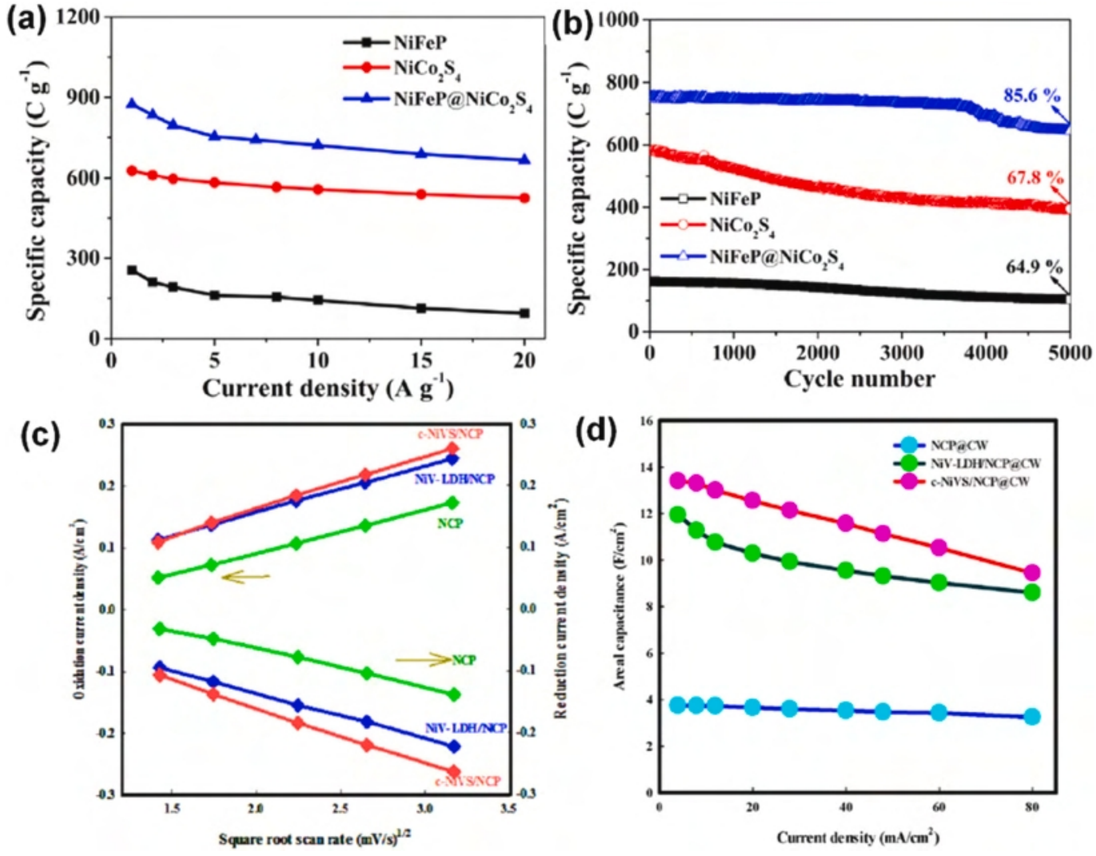

Fig. 19. (a) Rate capability of three samples. (b) Cycling stability at 5 A g^{-1} after 5000 cycles. (c) Oxidation and reduction peak current as a function of the square root of scan rate. (d) Rate capability.
(a, b) Reproduced from ref [209]. Copyright 2020 Elsevier. (c, d) Reproduced from ref [210]. Copyright 2020 Elsevier.

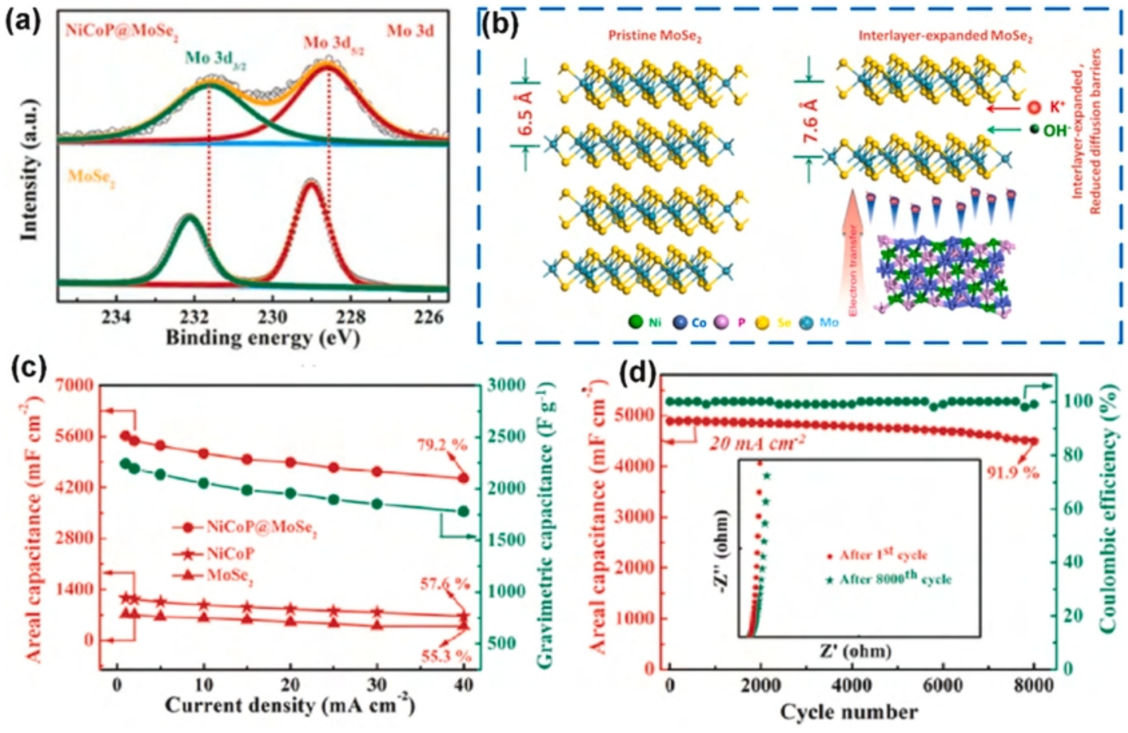

Fig. 20. (a) XPS spectra of Mo 3d. (b) The interaction model between the MoSe$_2$ and NiCoP to expand interlayer of MoSe$_2$. (c) Rate capability of MoSe$_2$, NiCoP and NiCoP@MoSe$_2$. (d) Cycling performance of NiCoP@MoSe$_2$ after 8000 cycles.
Reproduced from ref [213]. Copyright 2020 Elsevier.

rich redox reactions and small band gap [212]. When anchoring $MoSe_2$ nanosheets on NiCoP nanowires, the interplanar spacing of $MoSe_2$ nanosheets could be increased from 6.5 Å to 7.6 Å and the number of the layers is decreased from >15–2–3 due to the interaction between NiCoP and $MoSe_2$ [213]. As shown in Fig. 20a, the peaks of NiCoP@$MoSe_2$ shift to low binding energies compared to $MoSe_2$, indicating the electron transfer from NiCoP to $MoSe_2$, similar as metal sulfides above. Due to the electron transfer process, the D-orbital electron state density of Mo and Se is increased, which results in an expansion of interplanar spacing. Few layers and large interlayer spacing can provide more active sites and accelerate the diffusion of electrolyte ions, and 3D open heterostructure offers abundant mass transfer channels, contributing to rapid redox kinetics (Fig. 20b). The NiCoP@$MoSe_2$ electrode exhibits a high areal capacitance of 5613 mF cm^{-2} at a current density of 1 mA cm^{-2}, and retains 79.3% of initial capacitance at 40 mA cm^{-2}, which is better than that of NiCoP (57.6%) and $MoSe_2$ (55.3%) (Fig. 20c). After 8000 cycles at 20 mA cm^{-2}, 91.9% retention can be achieved (Fig. 20d) because of the strong interaction between two components, which improves the stability of electrode.

Summary and outlook

TMPs have been recognized as attractive electrode materials for SCs because of their unique metalloid character, outstanding electronic conductivity and excellent electrochemical activity. In particular, differentiating from EDLCs and pseudo-capacitors, TMPs show phase transformation that is the feature of battery-type electrodes during charge storage process. Both simple and complex transition metal phosphides have been studied as electrode materials for hybrid supercapacitors. Various nanostructured TMPs synthesized via different methods have demonstrated much improved electrochemical and transport properties. However, the sluggish reaction kinetics and volumetric expansion during charging /discharging progress remain as a bottleneck hindering the rate capability and cycling stability of TMPs capacitors. Optimizing synthesis process, doping, tailoring composition away from stoichiometry and designing composites have been representing approaches to improve the electrochemical performance: 1) properly designed and synthesized nanostructures benefit electrolyte penetration, ion diffusion and electron transfer, 2) doping tunes the electronic structure, and introduces defects, promoting electron transfer and facilitating redox reactions, 3) tailoring the composition away from stoichiometry could make full use of the nature characteristics of transition metal components, and 4) synergistically mixing of different phases to form composites has demonstrated to improve electrochemical properties. In spite of all the great progresses made, many challenges remain to be addressed in the synthesis, characterization further property improvement, and fundamental understanding of TMPs.

1) Most TMPs are synthesized through phosphorization of precursors (hydroxides and oxides) in inert gas using an excessive amount of P, such as NaH_2PO_2, which means a severe waste of phosphorus resources. Typical phosphorization releases flammable poisonous gaseous PH_3. Recently, other synthesis/processing methods, such as electrodeposition and hydrothermal reaction, have been studied, though attaining or retaining of desired morphologies remained unfinished tasks [214]. Gas-solid phosphating method is another way to synthesize TMPs; though easy to operate, it is difficult to control composition of the final products or the degree of phosphorization. Desirable eco-friendly and adjustable phosphorization process is still to be developed [108].
2) Metal foams, metal foils, and carbon clothes are commonly used as conductive substrates for the growth of TMPs. The performance of TMPs hybrid capacitors are strongly affected by the density, electrical conductivity and hydrophilicity of substrates. Metallic substrates are easily oxidized and corroded during the hydrothermal synthesis and thermal annealing. The oxides between metal foams or substrates as current collectors and TMPs active materials destroy the mechanical stability and energy storage performance of the hybrid capacitors. Carbon cloth, on the other hand, often suffers from low electrical conductivity in comparison with metallic substrates. New substrates with large specific surface areas, outstanding mechanical property and excellent electrical conductivity, such as 3D graphene foam [215,216] and melamine formaldehyde resin foam [25,217], are promising for the further improvement of the performance of TMPs hybrid capacitors.
3) Alkaline aqueous solution, such as KOH, is commonly used as electrolyte in TMPs hybrid capacitors. Oxygen evolution reaction (OER) is easy to occur in strong alkaline. Further work is required to develop new electrolytes, such as organic electrolyte, water-in-salt electrolyte and all-solid-state electrolyte. Appropriate electrolytes may broaden the potential window of TMPs and further enhance the energy density of SCs.
4) Complex phase transformation and structure reconstruction of TMPs often occur during the charge and discharge process when used as electrodes in hybrid capacitors. Advanced in-situ or *ex-situ* characterization techniques may be able to shed some light for a better understanding of the electrochemical behaviors during the charging-/discharging process. Theoretical calculation and models are another way to analyze redox reactions in electrode materials.

CRediT authorship contribution statement

Quan Zong: Conceptualization, Writing - original draft, Writing - review & editing. **Chaofeng Liu:** Conceptualization, Writing - review & editing. **Hui Yang:** Supervision, Funding acquisition. **Qilong Zhang:** Conceptualization, Supervision, Funding acquisition. **Guozhong Cao:** Conceptualization, Writing - review & editing, Supervision.

Declaration of Competing Interest

The authors declare that they have no known competing financial interests or personal relationships that could have appeared to influence the work reported in this paper.

Acknowledgements

This work was supported by National Natural Science Foundation of China (Grant No. 51772267), the National Key R&D Program of China (Grant No. 2016YFB0401501), the Key R&D Program of Zhejiang Province (Grant No. 2020C01004), and the National Science Foundation (CBET-1803256). The author acknowledges the financial support from China Scholarship Council (No. 201906320198) and 2019 Zhejiang University Academic Award for Outstanding Doctoral Candidates.

References

[1] W. Raza, F. Ali, N. Raza, Y. Luo, K.-H. Kim, J. Yang, S. Kumar, A. Mehmood, E.E. Kwon, Recent advancements in supercapacitor technology, Nano Energy 52 (2018) 441–473.
[2] F. Wang, X. Wu, X. Yuan, Z. Liu, Y. Zhang, L. Fu, Y. Zhu, Q. Zhou, Y. Wu, W. Huang, Latest advances in supercapacitors: from new electrode materials to novel device designs, Chem. Soc. Rev. 46 (2017) 6816–6854.
[3] S. Liu, L. Kang, J.M. Kim, Y.T. Chun, J. Zhang, S.C. Jun, Recent advances in vanadium-based aqueous rechargeable zinc-ion batteries, Adv. Energy Mater. 10 (2020) 2000477.

[4] D. Wei, M.R. Scherer, C. Bower, P. Andrew, T. Ryhanen, U. Steiner, A nanostructured electrochromic supercapacitor, Nano Lett. 12 (2012) 1857–1862.

[5] S.-W. Zhang, B.-S. Yin, X.-X. Liu, D.-M. Gu, H. Gong, Z.-B. Wang, A high energy density aqueous hybrid supercapacitor with widened potential window through multi approaches, Nano Energy 59 (2019) 41–49.

[6] W. Liu, M.S. Song, B. Kong, Y. Cui, Flexible and stretchable energy storage: recent advances and future perspectives, Adv. Mater. 29 (2017) 1603436.

[7] C.V.V. Muralee Gopi, R. Vinodh, S. Sambasivam, I.M. Obaidat, H.-J. Kim, Recent progress of advanced energy storage materials for flexible and wearable supercapacitor: From design and development to applications, J. Energy Storage 27 (2020) 101035.

[8] A. Konarov, N. Voronina, J.H. Jo, Z. Bakenov, Y.-K. Sun, S.-T. Myung, Present and future perspective on electrode materials for rechargeable zinc-ion batteries, ACS Energy Lett. 3 (2018) 2620–2640.

[9] V. Palomares, P. Serras, I. Villaluenga, K.B. Hueso, J. Carretero-González, T. Rojo, Scientific challenges for the implementation of Zn-ion batteries, Energy Environ. Sci. 5 (2012) 5884–5901.

[10] L.E. Blanc, D. Kundu, L.F. Nazar, Scientific challenges for thE IMPLEmentation of Zn-Ion batteries, Joule 4 (2020) 771–799.

[11] H. Li, L. Ma, C. Han, Z. Wang, Z. Liu, Z. Tang, C. Zhi, Advanced rechargeable zinc-based batteries: recent progress and future perspectives, Nano Energy 62 (2019) 550–587.

[12] J. Yan, S. Li, B. Lan, Y. Wu, P.S. Lee, Rational design of nanostructured electrode materials toward multifunctional supercapacitors, Adv. Funct. Mater. 30 (2019) 1902564.

[13] Y.B. Tan, J.-M. Lee, Graphene for supercapacitor applications, J. Mater. Chem. A 1 (2013) 14814–14843.

[14] X. Jia, C. Liu, Z.G. Neale, J. Yang, G. Cao, Active materials for aqueous zinc ion batteries: synthesis, crystal structure, morphology, and electrochemistry, Chem. Rev. 120 (2020) 7795–7866.

[15] D.R. Rolison, J.W. Long, J.C. Lytle, A.E. Fischer, C.P. Rhodes, T.M. McEvoy, M.E. Bourg, A.M. Lubers, Multifunctional 3D nanoarchitectures for energy storage and conversion, Chem. Soc. Rev. 38 (2009) 226–252.

[16] A. González, E. Goikolea, J.A. Barrena, R. Mysyk, Review on supercapacitors: technologies and materials, Renew. Sustain. Energy Rev. 58 (2016) 1189–1206.

[17] D.P. Dubal, O. Ayyad, V. Ruiz, P. Gomez-Romero, Hybrid energy storage: the merging of battery and supercapacitor chemistries, Chem. Soc. Rev. 44 (2015) 1777–1790.

[18] Z. Yu, L. Tetard, L. Zhai, J. Thomas, Supercapacitor electrode materials: nanostructures from 0 to 3 dimensions, Energy Environ. Sci. 8 (2015) 702–730.

[19] K. Naoi, S. Ishimoto, J.-i Miyamoto, W. Naoi, Second generation 'nanohybrid supercapacitor': Evolution of capacitive energy storage devices, Energy Environ. Sci. 5 (2012) 9363–9373.

[20] P. Simon, Y. Gogotsi, Perspectives for electrochemical capacitors and related devices, Nat. Mater. 19 (2020) 1151–1163.

[21] F. Cheng, X. Yang, S. Zhang, W. Lu, Boosting the supercapacitor performances of activated carbon with carbon nanomaterials, J. Power Sources 450 (2020) 227678.

[22] O. Yanshyna, H. Weissman, B. Rybtchinski, Recyclable electrochemical supercapacitors based on carbon nanotubes and organic nanocrystals, Nanoscale 12 (2020) 8909–8914.

[23] V. Gupta, A.M. Kannan, S. Kumar, Graphene Foam (GF)/Manganese Oxide (MnO$_2$) Nanocomposites for High Performance Supercapacitors, J. Energy Storage 30 (2020) 101575.

[24] Y.-J. Gu, W. Wen, J.-M. Wu, Wide potential window TiO$_2$@carbon cloth and high capacitance MnO$_2$@carbon cloth for the construction of a 2.6 V high-performance aqueous asymmetric supercapacitor, J. Power Sources 469 (2020) 228425.

[25] Y. Huang, F. Cui, J. Bao, Y. Zhao, J. Lian, T. Liu, H. Li, MnCo$_2$S$_4$/FeCo$_2$S$_4$ "lollipop" arrays on a hollow N-doped carbon skeleton as flexible electrodes for hybrid supercapacitors, J. Mater. Chem. A 7 (2019) 20778–20789.

[26] Q. Zhang, Z. Liu, B. Zhao, Y. Cheng, L. Zhang, H.-H. Wu, M.-S. Wang, S. Dai, K. Zhang, D. Ding, Y. Wu, M. Liu, Design and understanding of dendritic mixed-metal hydroxide nanosheets@N-doped carbon nanotube array electrode for high-performance asymmetric supercapacitors, Energy Storage Mater. 16 (2019) 632–645.

[27] J. Sun, L. Guo, X. Sun, J. Zhang, L. Hou, L. Li, S. Yang, C. Yuan, One-dimensional nanostructured pseudocapacitive materials: design, synthesis and applications in supercapacitors, Batter. Supercaps 2 (2019) 820–841.

[28] C. Choi, D.S. Ashby, D.M. Butts, R.H. DeBlock, Q. Wei, J. Lau, B. Dunn, Achieving high energy density and high power density with pseudocapacitive materials, Nat. Rev. Mater. 5 (2019) 5–19.

[29] Y. Gogotsi, R.M. Penner, Energy storage in nanomaterials - capacitive, pseudocapacitive, or battery-like? ACS Nano 12 (2018) 2081–2083.

[30] Y. Deng, Y. Xie, K. Zou, X. Ji, Review on recent advances in nitrogen-doped carbons: preparations and applications in supercapacitors, J. Mater. Chem. A 4 (2016) 1144–1173.

[31] J. Jiang, Y. Zhang, P. Nie, G. Xu, M. Shi, J. Wang, Y. Wu, R. Fu, H. Dou, X. Zhang, Progress of nanostructured electrode materials for supercapacitors, Adv. Sustain. Syst. 2 (2018) 1700110.

[32] X. Yu, S. Yun, J.S. Yeon, P. Bhattacharya, L. Wang, S.W. Lee, X. Hu, H.S. Park, Emergent pseudocapacitance of 2D nanomaterials, Adv. Energy Mater. 8 (2018) 1702930.

[33] S. Fleischmann, J.B. Mitchell, R. Wang, C. Zhan, D.E. Jiang, V. Presser, V. Augustyn, Pseudocapacitance: from fundamental understanding to high power energy storage materials, Chem. Rev. 120 (2020) 6738–6782.

[34] F. Yu, T. Huang, P. Zhang, Y. Tao, F.-Z. Cui, Q. Xie, S. Yao, F. Wang, Design and synthesis of electrode materials with both battery-type and capacitive charge storage, Energy Storage Mater. 22 (2019) 235–255.

[35] S. Trasatti, G. Buzzanca, Ruthenium dioxide: a new interesting electrode material. Solid state structure and electrochemical behaviour, J. Electroanal. Chem. Interfacial Electrochem. 29 (1971) A1–A5.

[36] H. Wang, J. Lin, Z.X. Shen, Polyaniline (PANi) based electrode materials for energy storage and conversion, J. Sci. Adv. Mater. Dev. 1 (2016) 225–255.

[37] T. Zhai, S. Xie, M. Yu, P. Fang, C. Liang, X. Lu, Y. Tong, Oxygen vacancies enhancing capacitive properties of MnO$_2$ nanorods for wearable asymmetric supercapacitors, Nano Energy 8 (2014) 255–263.

[38] Z. Tong, S. Liu, Y. Zhou, J. Zhao, Y. Wu, Y. Wang, Y. Li, Rapid redox kinetics in uniform sandwich-structured mesoporous Nb$_2$O$_5$/graphene/mesoporous Nb$_2$O$_5$ nanosheets for high-performance sodium-ion supercapacitors, Energy Storage Mater. 13 (2018) 223–232.

[39] B. Saravanakumar, K.K. Purushothaman, G. Muralidharan, Interconnected V$_2$O$_5$ nanoporous network for high-performance supercapacitors, ACS Appl. Mater. Interfaces 4 (2012) 4484–4490.

[40] H.S. Kim, J.B. Cook, H. Lin, J.S. Ko, S.H. Tolbert, V. Ozolins, B. Dunn, Oxygen vacancies enhance pseudocapacitive charge storage properties of MoO$_{3-x}$, Nat. Mater. 16 (2017) 454–460.

[41] X. Wang, Y. Fang, B. Shi, F. Huang, F. Rong, R. Que, Three-dimensional NiCo$_2$O$_4$@NiCo$_2$O$_4$ core–shell nanocones arrays for high-performance supercapacitors, Chem. Eng. J. 344 (2018) 311–319.

[42] S.J. Patil, N.R. Chodankar, R.B. Pujari, Y.-K. Han, D.W. Lee, Core-shell heteronanostructured 1D transition metal polyphosphates decorated 2D bimetallic layered double hydroxide for sustainable hybrid supercapacitor, J. Power Sources 466 (2020) 228286.

[43] B. Huang, H. Wang, S. Liang, H. Qin, Y. Li, Z. Luo, C. Zhao, L. Xie, L. Chen, Two-dimensional porous cobalt–nickel tungstate thin sheets for high performance supercapattery, Energy Storage Mater. 32 (2020) 105–114.

[44] Y. Jiang, J. Liu, Definitions of pseudocapacitive materials: a brief review, Energy Environ. Mater. 2 (2019) 30–37.

[45] Y. Li, X. Han, T. Yi, Y. He, X. Li, Review and prospect of NiCo$_2$O$_4$-based composite materials for supercapacitor electrodes, J. Energy Chem. 31 (2019) 54–78.

[46] H. Lv, Q. Pan, Y. Song, X.-X. Liu, T. Liu, A review on nano-/microstructured materials constructed by electrochemical technologies for supercapacitors, Nano-Micro Lett. 12 (2020) 118.

[47] B.Y. Guan, A. Kushima, L. Yu, S. Li, J. Li, X.W. Lou, Coordination polymers derived general synthesis of multishelled mixed metal-oxide particles for hybrid supercapacitors, Adv. Mater. 29 (2017) 1605902.

[48] T. Ling, P. Da, X. Zheng, B. Ge, Z. Hu, M. Wu, X.-W. Du, W.-B. Hu, M. Jaroniec, S. Qiao, Atomic-level structure engineering of metal oxides for high-rate oxygen intercalation pseudocapacitance, Sci. Adv. 4 (2018) eaau6261.

[49] D. Tie, S. Huang, J. Wang, J. Ma, J. Zhang, Y. Zhao, Hybrid energy storage devices: advanced electrode materials and matching principles, Energy Storage Mater. 21 (2019) 22–40.

[50] H. Hu, B.Y. Guan, X.W. Lou, Construction of complex CoS hollow structures with enhanced electrochemical properties for hybrid supercapacitors, Chem 1 (2016) 102–113.

[51] A. Muzaffar, M.B. Ahamed, K. Deshmukh, J. Thirumalai, A review on recent advances in hybrid supercapacitors: design, fabrication and applications, Renew. Sustain. Energy Rev. 101 (2019) 123–145.

[52] H. Dan, K. Tao, Y. Hai, L. Liu, Y. Gong, (Co, Mn)-Doped NiSe$_2$-diethylenetriamine (dien) nanosheets and (Co, Mn, Sn)-doped NiSe$_2$ nanowires for high performance supercapacitors: compositional/morphological evolution and (Co, Mn)-induced electron transfer, Nanoscale 11 (2019) 16810–16827.

[53] Q. Liu, X. Hong, X. You, X. Zhang, X. Zhao, X. Chen, M. Ye, X. Liu, Designing heterostructured metal sulfide core-shell nanoneedle films as battery-type electrodes for hybrid supercapacitors, Energy Storage Mater. 24 (2020) 541–549.

[54] N. Zhang, J. Xu, B. Wei, J. Li, I. Amorim, R. Thomas, S.M. Thalluri, Z. Wang, W. Zhou, S. Xie, L. Liu, Mille-crêpe-like metal phosphide nanocrystals/carbon nanotube film composites as high-capacitance negative electrodes in asymmetric supercapacitors, ACS appl. Energy Mater. 3 (2020) 4580–4588.

[55] Q. Zhang, B. Zhao, J. Wang, C. Qu, H. Sun, K. Zhang, M. Liu, High-performance hybrid supercapacitors based on self-supported 3D ultrathin porous quaternary Zn-Ni-Al-Co oxide nanosheets, Nano Energy 28 (2016) 475–485.

[56] W. Zuo, R. Li, C. Zhou, Y. Li, J. Xia, J. Liu, Battery-supercapacitor hybrid devices: recent progress and future prospects, Adv. Sci. (Weinh) 4 (2017) 1600539.

[57] Y. Shao, M.F. El-Kady, J. Sun, Y. Li, Q. Zhang, M. Zhu, H. Wang, B. Dunn, R.B. Kaner, Design and mechanisms of asymmetric supercapacitors, Chem. Rev. 118 (2018) 9233–9280.

[58] Y. Wang, Y. Song, Y. Xia, Electrochemical capacitors: mechanism, materials, systems, characterization and applications, Chem. Soc. Rev. 45 (2016) 5925–5950.

[59] G. Zhang, X.W. Lou, General solution growth of mesoporous NiCo$_2$O$_4$ nanosheets on various conductive substrates as high-performance electrodes for supercapacitors, Adv. Mater. 25 (2013) 976–979.

[60] S. Liu, D. Ni, H.-F. Li, K.N. Hui, C.-Y. Ouyang, S.C. Jun, Effect of cation substitution on the pseudocapacitive performance of spinel cobaltite MCo$_2$O$_4$(M = Mn, Ni, Cu, and Co), J. Mater. Chem. A 6 (2018) 10674–10685.

[61] Y. Huang, C. Yan, X. Shi, W. Zhi, Z. Li, Y. Yan, M. Zhang, G. Cao, Ni$_{0.85}$Co$_{0.15}$WO$_4$ nanosheet electrodes for supercapacitors with excellent electrical conductivity and capacitive performance, Nano Energy 48 (2018) 430–440.

[62] X. Wu, Z. Han, X. Zheng, S. Yao, X. Yang, T. Zhai, Core-shell structured Co_3O_4@$NiCo_2O_4$ electrodes grown on flexible carbon fibers with superior electrochemical properties, Nano Energy 31 (2017) 410–417.

[63] C. Li, J. Balamurugan, N.H. Kim, J.H. Lee, Hierarchical Zn-Co-S nanowires as advanced electrodes for all solid state asymmetric supercapacitors, Adv. Energy Mater. 8 (2018) 1702014.

[64] W. Chen, X. Zhang, L.-E. Mo, Y. Zhang, S. Chen, X. Zhang, L. Hu, $NiCo_2S_4$ quantum dots with high redox reactivity for hybrid supercapacitors, Chem. Eng. J. 388 (2020) 124109.

[65] X. Li, H. Wu, C. Guan, A.M. Elshahawy, Y. Dong, S.J. Pennycook, J. Wang, Multimaterials: microtopography-guided radial gradient circle array film with nanoscale resolution, Small 15 (2019) 1803895.

[66] J. Zhang, J. Lin, J. Wu, R. Xu, M. Lai, C. Gong, X. Chen, P. Zhou, Excellent electrochemical performance hierarchical Co_3O_4@Ni_3S_2 core/shell nanowire arrays for asymmetric supercapacitors, Electrochim. Acta 207 (2016) 87–96.

[67] H. Chen, L. Hu, M. Chen, Y. Yan, L. Wu, Nickel–cobalt layered double hydroxide nanosheets for high-performance supercapacitor electrode materials, Adv. Funct. Mater. 24 (2014) 934–942.

[68] N. Zhang, Y. Li, J. Xu, J. Li, B. Wei, Y. Ding, I. Amorim, R. Thomas, S.M. Thalluri, Y. Liu, G. Yu, L. Liu, High-performance flexible solid-state asymmetric supercapacitors based on bimetallic transition metal phosphide nanocrystals, ACS Nano 13 (2019) 10612–10621.

[69] X. Li, A.M. Elshahawy, C. Guan, J. Wang, Metal phosphides and phosphates-based electrodes for electrochemical supercapacitors, Small 13 (2017) 1701530.

[70] X. Wang, H.-M. Kim, Y. Xiao, Y.-K. Sun, Nanostructured metal phosphide-based materials for electrochemical energy storage, J. Mater. Chem. A 4 (2016) 14915–14931.

[71] Z. Liang, C. Qu, W. Zhou, R. Zhao, H. Zhang, B. Zhu, W. Guo, W. Meng, Y. Wu, W. Aftab, Q. Wang, R. Zou, Synergistic effect of Co-Ni hybrid phosphide nanocages for ultrahigh capacity fast energy storage, Adv. Sci. (Weinh) 6 (2019) 1802005.

[72] D. Guo, Y. Zhang, W. Sun, D. Chu, B. Li, L. Tan, H. Ma, H. Pang, X. Wang, L. Zhang, Facile dual-ligand modulation tactic toward nickel-cobalt sulfides/phosphides/selenides as supercapacitor electrodes with long-term durability and electrochemical activity, ACS Appl. Mater. Interfaces 11 (2019) 41580–41587.

[73] K.N. Dinh, Q. Liang, C.-F. Du, J. Zhao, A.I.Y. Tok, H. Mao, Q. Yan, Nanostructured metallic transition metal carbides, nitrides, phosphides, and borides for energy storage and conversion, Nano Today 25 (2019) 99–121.

[74] Z. Li, Y. Zheng, Q. Liu, Y. Wang, D. Wang, Z. Li, P. Zheng, Z. Liu, Recent advances in nanostructured metal phosphides as promising anode materials for rechargeable batteries, J. Mater. Chem. A 8 (2020) 19113–19132.

[75] R.R. Salunkhe, Y. Kamachi, N.L. Torad, S.M. Hwang, Z. Sun, S.X. Dou, J.H. Kim, Y. Yamauchi, Fabrication of symmetric supercapacitors based on MOF-derived nanoporous carbons, J. Mater. Chem. A 2 (2014) 19848–19854.

[76] Q. Jiang, N. Kurra, M. Alhabeb, Y. Gogotsi, H.N. Alshareef, All pseudocapacitive MXene-RuO_2 asymmetric supercapacitors, Adv. Energy Mater. 8 (2018) 1703043.

[77] Z. Yu, B. Duong, D. Abbitt, J. Thomas, Highly ordered MnO_2 nanopillars for enhanced supercapacitor performance, Adv. Mater. 25 (2013) 3302–3306.

[78] Y. Shi, L. Peng, Y. Ding, Y. Zhao, G. Yu, Nanostructured conductive polymers for advanced energy storage, Chem. Soc. Rev. 44 (2015) 6684–6696.

[79] M. Liu, B. Su, Y. Tang, X. Jiang, A. Yu, Recent advances in nanostructured vanadium oxides and composites for energy conversion, Adv. Energy Mater. 7 (2017) 1700885.

[80] H.C. Chen, S. Jiang, B. Xu, C. Huang, Y. Hu, Y. Qin, M. He, H. Cao, Sea-urchin-like nickel–cobalt phosphide/phosphate composites as advanced battery materials for hybrid supercapacitors, J. Mater. Chem. A 7 (2019) 6241–6249.

[81] W. Lu, J. Shen, P. Zhang, Y. Zhong, Y. Hu, X.W. Lou, Construction of CoO/Co-Cu-S hierarchical tubular heterostructures for hybrid supercapacitors, Angew. Chem. Int Ed. Engl. 58 (2019) 15441–15447.

[82] B. Zhao, L. Zhang, Q. Zhang, D. Chen, Y. Cheng, X. Deng, Y. Chen, R. Murphy, X. Xiong, B. Song, C.-P. Wong, M.-S. Wang, M. Liu, Rational design of nickel hydroxide-based nanocrystals on graphene for ultrafast energy storage, Adv. Energy Mater. 8 (2018) 1702247.

[83] B. Zhao, D. Chen, X. Xiong, B. Song, R. Hu, Q. Zhang, B.H. Rainwater, G.H. Waller, D. Zhen, Y. Ding, Y. Chen, C. Qu, D. Dang, C.-P. Wong, M. Liu, A high-energy, long cycle-life hybrid supercapacitor based on graphene composite electrodes, Energy Storage Mater. 7 (2017) 32–39.

[84] S.-W. Chou, J.-Y. Lin, Cathodic deposition of flaky nickel sulfide nanostructure as an electroactive material for high-performance supercapacitors, J. Electrochem. Soc. 160 (2013) D178–D182.

[85] Y. Yang, S. Li, W. Huang, H. Shangguan, C. Engelbrekt, S. Duan, L. Ci, P. Si, Effective synthetic strategy for $Zn_{0.76}Co_{0.24}S$ encapsulated in stabilized N-doped carbon nanoarchitecture towards ultra-long-life hybrid supercapacitors, J. Mater. Chem. A 7 (2019) 14670–14680.

[86] T. Deepalakshmi, T.T. Nguyen, N.H. Kim, K.T. Chong, J.H. Lee, Rational design of ultrathin 2D tin nickel selenide nanosheets for high-performance flexible supercapacitors, J. Mater. Chem. A 7 (2019) 24462–24476.

[87] G. Nagaraju, S.M. Cha, S.C. Sekhar, J.S. Yu, Metallic layered polyester fabric enabled nickel selenide nanostructures as highly conductive and binderless electrode with superior energy storage performance, Adv. Energy Mater. 7 (2017) 1601362.

[88] J. Cherusseri, N. Choudhary, K. Sambath Kumar, Y. Jung, J. Thomas, Recent trends in transition metal dichalcogenide based supercapacitor electrodes, Nanoscale Horiz. 4 (2019) 840–858.

[89] S. Carenco, D. Portehault, C. Boissiere, N. Mezailles, C. Sanchez, Nanoscaled metal borides and phosphides: recent developments and perspectives, Chem. Rev. 113 (2013) 7981–8065.

[90] S. Liu, K.V. Sankar, A. Kundu, M. Ma, J.Y. Kwon, S.C. Jun, Honeycomb-like interconnected network of nickel phosphide heteronanoparticles with superior electrochemical performance for supercapacitors, ACS Appl. Mater. Interfaces 9 (2017) 21829–21838.

[91] T.T. Nguyen, J. Balamurugan, N.H. Kim, J.H. Lee, Hierarchical 3D Zn–Ni–P nanosheet arrays as an advanced electrode for high-performance all-solid-state asymmetric supercapacitors, J. Mater. Chem. A 6 (2018) 8669–8681.

[92] S. Li, M. Hua, Y. Yang, W. Huang, X. Lin, L. Ci, J. Lou, P. Si, Self-supported multidimensional Ni–Fe phosphide networks with holey nanosheets for high-performance all-solid-state supercapacitors, J. Mater. Chem. A 7 (2019) 17386–17399.

[93] W. Song, J. Wu, G. Wang, S. Tang, G. Chen, M. Cui, X. Meng, Rich-mixed-valence $Ni_xCo_{3-x}P_y$ porous nanowires interwelded junction-free 3D network architectures for ultrahigh areal energy density supercapacitors, Adv. Funct. Mater. 28 (2018) 1804620.

[94] S.T. Oyama, T. Gott, H. Zhao, Y.-K. Lee, Transition metal phosphide hydroprocessing catalysts: a review, Catal. Today 143 (2009) 94–107.

[95] S. He, Z. Li, H. Mi, C. Ji, F. Guo, X. Zhang, Z. Li, Q. Du, J. Qiu, 3D nickel-cobalt phosphide heterostructure for high-performance solid-state hybrid supercapacitors, J. Power Sources 467 (2020) 228324.

[96] H. Liu, X. Liu, S. Wang, H.-K. Liu, L. Li, Transition metal based battery-type electrodes in hybrid supercapacitors: a review, Energy Storage Mater. 28 (2020) 122–145.

[97] T. Brousse, D. Bélanger, J.W. Long, To be or not to be pseudocapacitive, J. Electrochem. Soc. 162 (2015) A5185–A5189.

[98] X. Li, H. Wu, A.M. Elshahawy, L. Wang, S.J. Pennycook, C. Guan, J. Wang, Cactus-like NiCoP/NiCo-OH 3D architecture with tunable composition for high-performance electrochemical capacitors, Adv. Funct. Mater. 28 (2018) 1800036.

[99] Y. Lin, K. Sun, S. Liu, X. Chen, Y. Cheng, W.C. Cheong, Z. Chen, L. Zheng, J. Zhang, X. Li, Y. Pan, C. Chen, Construction of CoP/NiCoP nanotadpoles heterojunction interface for wide pH hydrogen evolution electrocatalysis and supercapacitor, Adv. Energy Mater. 9 (2019) 1901213.

[100] Y. Xu, S. Hou, G. Yang, X. Wang, T. Lu, L. Pan, Synthesis of bimetallic $Ni_xCo_{1-x}P$ hollow nanocages from metal-organic frameworks for high performance hybrid supercapacitors, Electrochim. Acta 285 (2018) 192–201.

[101] X. Cao, D. Jia, D. Li, L. Cui, J. Liu, One-step co-electrodeposition of hierarchical radial Ni_xP nanospheres on Ni foam as highly active flexible electrodes for hydrogen evolution reaction and supercapacitor, Chem. Eng. J. 348 (2018) 310–318.

[102] N. Zhao, H. Fan, J. Ma, M. Zhang, C. Wang, H. Li, X. Jiang, X. Cao, Entire synergistic contribution of electrodeposited battery-type $NiCo_2O_4$@$Ni_{4.5}Co_{4.5}S_8$ composite for high-performance supercapacitors, J. Power Sources 439 (2019) 227097.

[103] Y. Shi, M. Li, Y. Yu, B. Zhang, Recent advances in nanostructured transition metal phosphides: synthesis and energy-related applications, Energy Environ. Sci. 13 (2020) 4564–4582.

[104] Y. Li, Z. Dong, L. Jiao, Multifunctional transition metal-based phosphides in energy-related electrocatalysis, Adv. Energy Mater. 10 (2019) 1902104.

[105] J. Wang, Z. Liu, Y. Zheng, L. Cui, W. Yang, J. Liu, Recent advances in cobalt phosphide based materials for energy-related applications, J. Mater. Chem. A 5 (2017) 22913–22932.

[106] Y. Shi, B. Zhang, Recent advances in transition metal phosphide nanomaterials: synthesis and applications in hydrogen evolution reaction, Chem. Soc. Rev. 45 (2016) 1529–1541.

[107] N. Jiang, B. You, M. Sheng, Y. Sun, Electrodeposited cobalt-phosphorous-derived films as competent bifunctional catalysts for overall water splitting, Angew. Chem. Int Ed. Engl. 54 (2015) 6251–6254.

[108] M. Kong, H. Song, J. Zhou, Metal-organophosphine framework-derived N,P-codoped carbon-confined Cu_3P nanopaticles for superb Na-ion storage, Adv. Energy Mater. 8 (2018) 1801489.

[109] X. Wang, L. Chai, J. Ding, L. Zhong, Y. Du, T.-T. Li, Y. Hu, J. Qian, S. Huang, Chemical and morphological transformation of MOF-derived bimetallic phosphide for efficient oxygen evolution, Nano Energy 62 (2019) 745–753.

[110] G. Qu, P. Sun, G. Xiang, J. Yin, Q. Wei, C. Wang, X. Xu, Moss-like nickel-cobalt phosphide nanostructures for highly flexible all-solid-state hybrid supercapacitors with excellent electrochemical performances, Appl. Mater. Today 20 (2020) 100713.

[111] Y. Hu, M. Liu, Q. Yang, L. Kong, L. Kang, Facile synthesis of high electrical conductive CoP via solid-state synthetic routes for supercapacitors, J. Energy Chem. 26 (2017) 49–55.

[112] M. Cheng, H. Fan, Y. Xu, R. Wang, X. Zhang, Hollow Co_2P nanoflowers assembled from nanorods for ultralong cycle-life supercapacitors, Nanoscale 9 (2017) 14162–14171.

[113] K. Zhou, W. Zhou, L. Yang, J. Lu, S. Cheng, W. Mai, Z. Tang, L. Li, S. Chen, Ultrahigh-performance pseudocapacitor electrodes based on transition metal phosphide nanosheets array via phosphorization: a general and effective approach, Adv. Funct. Mater. 25 (2015) 7530–7538.

[114] Z. Zhang, S. Liu, J. Xiao, S. Wang, Fiber-based multifunctional nickel phosphide electrodes for flexible energy conversion and storage, J. Mater. Chem. A 4 (2016) 9691–9699.

[115] Y.-C. Chen, Z.-B. Chen, Y.-G. Lin, Y.-K. Hsu, Synthesis of copper phosphide nanotube arrays as electrodes for asymmetric supercapacitors, ACS Sustain. Chem. Eng. 5 (2017) 3863–3870.

[116] A. Jiang, Z. Wang, Q. Li, M. Dong, Ionic liquid-assisted synthesis of hierarchical one-dimensional MoP/NPC for high-performance supercapacitor and electrocatalysis, ACS Sustain. Chem. Eng. 8 (2020) 6343–6351.

[117] Z. Zheng, M. Retana, X. Hu, R. Luna, Y.H. Ikuhara, W. Zhou, Three-dimensional cobalt phosphide nanowire arrays as negative electrode material for flexible solid-state asymmetric supercapacitors, ACS Appl. Mater. Interfaces 9 (2017) 16986–16994.

[118] D. Wang, L.-B. Kong, M.-C. Liu, W.-B. Zhang, Y.-C. Luo, L. Kang, Amorphous Ni–P materials for high performance pseudocapacitors, J. Power Sources 274 (2015) 1107–1113.

[119] N. Zhang, M. Jia, Y. Dong, Y. Wang, J. Xu, Y. Liu, L. Jiao, F. Cheng, Hydrated layered vanadium oxide as a highly reversible cathode for rechargeable aqueous zinc batteries, Adv. Funct. Mater. 29 (2019) 1807331.

[120] G. Zhu, L. Yang, W. Wang, M. Ma, J. Zhang, H. Wen, D. Zheng, Y. Yao, Hierarchical three-dimensional manganese doped cobalt phosphide nanowire decorated nanosheet cluster arrays for high-performance electrochemical pseudocapacitor electrodes, Chem. Commun. 54 (2018) 9234–9237.

[121] J. Huang, J. Wei, Y. Xiao, Y. Xu, Y. Xiao, Y. Wang, L. Tan, K. Yuan, Y. Chen, When Al-doped cobalt sulfide nanosheets meet nickel nanotube arrays: a highly efficient and stable cathode for asymmetric supercapacitors, ACS Nano 12 (2018) 3030–3041.

[122] T. Wang, H.C. Chen, F. Yu, X.S. Zhao, H. Wang, Boosting the cycling stability of transition metal compounds-based supercapacitors, Energy Storage Mater. 16 (2019) 545–573.

[123] F. Wang, K. Ma, W. Tian, J. Dong, H. Han, H. Wang, K. Deng, H. Yue, Y.X. Zhang, W. Jiang, J. Ji, P-doped $NiMoO_4$ parallel arrays anchored on cobalt carbonate hydroxide with oxygen vacancies and mass transfer channels for supercapacitors and oxygen evolution, J. Mater. Chem. A 7 (2019) 19589–19596.

[124] S. Liu, Y. Yin, D. Ni, K.S. Hui, K.N. Hui, S. Lee, C.-Y. Ouyang, S.C. Jun, Phosphorous-containing oxygen-deficient cobalt molybdate as an advanced electrode material for supercapacitors, Energy Storage Mater. 19 (2019) 186–196.

[125] Q. Li, Q. Zhang, C. Liu, W. Gong, Z. Zhou, P. Man, J. Guo, B. He, K. Zhang, W. Lu, Y. Yao, Interface engineered and surface modulated electrode materials for ultrahigh-energy-density wearable NiCo//Fe batteries, Energy Storage Mater. 27 (2020) 316–326.

[126] Y. Lan, H. Zhao, Y. Zong, X. Li, Y. Sun, J. Feng, Y. Wang, X. Zheng, Y. Du, Phosphorization boosts the capacitance of mixed metal nanosheet arrays for high performance supercapacitor electrodes, Nanoscale 10 (2018) 11775–11781.

[127] H.C. Chen, Y. Qin, H. Cao, X. Song, C. Huang, H. Feng, X.S. Zhao, Synthesis of amorphous nickel–cobalt–manganese hydroxides for supercapacitor-battery hybrid energy storage system, Energy Storage Mater. 17 (2019) 194–203.

[128] X. Zhou, H. Dai, X. Huang, Y. Ren, Q. Wang, W. Wang, W. Huang, X. Dong, Porous trimetallic fluoride Ni-Co-M (M=Mn, Fe, Cu, Zn) nanoprisms as electrodes for asymmetric supercapacitors, Mater. Today Energy 17 (2020) 1000429.

[129] J. Li, Z. Liu, Q. Zhang, Y. Cheng, B. Zhao, S. Dai, H.-H. Wu, K. Zhang, D. Ding, Y. Wu, M. Liu, M.-S. Wang, Anion and cation substitution in transition-metal oxides nanosheets for high-performance hybrid supercapacitors, Nano Energy 57 (2019) 22–33.

[130] P. Bandyopadhyay, G. Saeed, N.H. Kim, J.H. Lee, Zinc-nickel-cobalt oxide@$NiMoO_4$ core-shell nanowire/nanosheet arrays for solid state asymmetric supercapacitors, Chem. Eng. J. 384 (2020) 123357.

[131] S. Kumar, G. Saeed, N.H. Kim, J.H. Lee, Fabrication of Co–Ni–Zn ternary Oxide@$NiWO_4$ core-shell nanowire arrays and Fe_2O_3-CNTs@GF for ultra-high-performance asymmetric supercapacitor, Compos. Part B: Eng. 176 (2019) 107223.

[132] Z.-H. Huang, F.-F. Sun, M. Batmunkh, W.-H. Li, H. Li, Y. Sun, Q. Zhao, X. Liu, T.-Y. Ma, Zinc–nickel–cobalt ternary hydroxide nanoarrays for high-performance supercapacitors, J. Mater. Chem. A 7 (2019) 11826–11835.

[133] X. Lei, S. Ge, Y. Tan, Z. Wang, J. Li, X. Li, G. Hu, X. Zhu, M. Huang, Y. Zhu, B. Xiang, High capacity and energy density of Zn-Ni-Co-P nanowire arrays as an advanced electrode for aqueous asymmetric supercapacitor, ACS Appl. Mater. Interfaces 12 (2020) 9158–9168.

[134] Y. Yang, Y. Zhou, Z. Hu, W. Wang, X. Zhang, L. Qiang, Q. Wang, 3D thin-wall cell structure nickel-cobalt-molybdenum ternary phosphides on carbon cloth as high-performance electrodes for asymmetric supercapacitors, J. Alloy. Compd. 772 (2019) 683–692.

[135] R. Niu, G. Wang, Y. Ding, S. Tang, X. Hu, J. Zhu, Hexagonal prism arrays constructed using ultrathin porous nanoflakes of carbon doped mixed-valence Co–Mn–Fe phosphides for ultrahigh areal capacitance and remarkable cycling stability, J. Mater. Chem. A 7 (2019) 4431–4437.

[136] Y. Yang, W. Huang, S. Li, L. Ci, P. Si, Surfactant-dependent flower- and grass-like $Zn_{0.76}Co_{0.24}S/Co_3S_4$ for high-performance all-solid-state asymmetric supercapacitors, J. Mater. Chem. A 6 (2018) 22830–22839.

[137] Q. Zhang, E. Uchaker, S.L. Candelaria, G. Cao, Nanomaterials for energy conversion and storage, Chem. Soc. Rev. 42 (2013) 3127–3171.

[138] C. Liu, R. Massé, X. Nan, G. Cao, A promising cathode for Li-ion batteries: $Li_3V_2(PO_4)_3$, Energy Storage Mater. 4 (2016) 15–58.

[139] G. Zhou, L. Xu, G. Hu, L. Mai, Y. Cui, Nanowires for electrochemical energy storage, Chem. Rev. 119 (2019) 11042–11109.

[140] J. Wang, Y. Cui, D. Wang, Design of hollow nanostructures for energy storage, conversion and production, Adv. Mater. 31 (2019) 1801993.

[141] L. Yu, B. Guan, W. Xiao, X.W.D. Lou, Formation of yolk-shelled Ni–Co mixed oxide nanoprisms with enhanced electrochemical performance for hybrid supercapacitors and lithium ion batteries, Adv. Energy Mater. 5 (2015) 1500891.

[142] B.Y. Guan, L. Yu, X. Wang, S. Song, X.W. Lou, Formation of onion-like $NiCo_2S_4$ particles via sequential ion-exchange for hybrid supercapacitors, Adv. Mater. 29 (2017) 1605051.

[143] L. Ding, L. Chen, Z. Ma, X. Zhang, K. Zhang, G. Zhu, Z. Yu, J. Deng, F. Chen, D. Yan, H. Xu, A. Yu, High-performance asymmetrical hybrid supercapacitor based on yolk-shell Ni_3P nanoparticles constructed by selective etching, Electrochim. Acta 357 (2020) 136875.

[144] S.E. Moosavifard, S.K. Kaverlavani, J. Shamsi, A. Bakouei, Hierarchical multi-shelled nanoporous mixed copper cobalt phosphide hollow microspheres as a novel advanced electrode for high-performance asymmetric supercapacitors, J. Mater. Chem. A 5 (2017) 18429–18433.

[145] K. Yu, X. Pan, G. Zhang, X. Liao, X. Zhou, M. Yan, L. Xu, L. Mai, Nanowires in energy storage devices: structures, synthesis, and applications, Adv. Energy Mater. 8 (2018) 1802369.

[146] Y. Gan, C. Wang, X. Chen, P. Liang, H. Wan, X. Liu, Q. Tan, H. Wu, H. Rao, H. Wang, J. Zhang, Y. Wang, P.A. van Aken, H. Wang, High conductivity $Ni_{12}P_5$ nanowires as high-rate electrode material for battery-supercapacitor hybrid devices, Chem. Eng. J. 392 (2020) 123661.

[147] Y. Ouyang, X. Xia, H. Ye, L. Wang, X. Jiao, W. Lei, Q. Hao, Three-dimensional hierarchical structure ZnO@C@NiO on carbon cloth for asymmetric supercapacitor with enhanced cycle stability, ACS Appl. Mater. Interfaces 10 (2018) 3549–3561.

[148] J. Hou, Y. Wu, B. Zhang, S. Cao, Z. Li, L. Sun, Rational design of nanoarray architectures for electrocatalytic water splitting, Adv. Funct. Mater. 29 (2019) 1808367.

[149] A. Mohammadi Zardkhoshoui, S.S. Hosseiny Davarani, A rational design of nanoporous Cu-Co-Ni-P nanotube arrays and $CoFe_2Se_4$ nanosheet arrays for flexible solid-state asymmetric devices, Dalton Trans. 49 (2020) 10028–10041.

[150] X. Wu, B. Huang, Q. Wang, Y. Wang, High energy density of two-dimensional MXene/NiCo-LDHs interstratification assembly electrode: understanding the role of interlayer ions and hydration, Chem. Eng. J. 380 (2020) 122456.

[151] R. Sahoo, A. Pal, T. Pal, 2D materials for renewable energy storage devices: outlook and challenges, Chem. Commun. 52 (2016) 13528–13542.

[152] X. Zhang, A. Wu, X. Wang, C. Tian, R. An, H. Fu, Porous NiCoP nanosheets as efficient and stable positive electrodes for advanced asymmetric supercapacitors, J. Mater. Chem. A 6 (2018) 17905–17914.

[153] H. Liang, C. Xia, Q. Jiang, A.N. Gandi, U. Schwingenschlögl, H.N. Alshareef, Low temperature synthesis of ternary metal phosphides using plasma for asymmetric supercapacitors, Nano Energy 35 (2017) 331–340.

[154] Y. Zhu, Q. Zong, Q. Zhang, H. Yang, Q. Wang, H. Wang, Three-dimensional core-shell NiCoP@NiCoP array on carbon cloth for high performance flexible asymmetric supercapacitor, Electrochim. Acta 299 (2019) 441–450.

[155] Y. Zhao, M. Zhao, X. Ding, Z. Liu, H. Tian, H. Shen, X. Zu, S. Li, L. Qiao, One-step colloid fabrication of nickel phosphides nanoplate/nickel foam hybrid electrode for high-performance asymmetric supercapacitors, Chem. Eng. J. 373 (2019) 1132–1143.

[156] J. Song, J. Xiang, C. Mu, B. Wang, F. Wen, C. Su, C. Wang, Z. Liu, Facile synthesis and excellent electrochemical performance of CoP nanowire on carbon cloth as bifunctional electrode for hydrogen evolution reaction and supercapacitor, Sci. China Mater. 60 (2017) 1179–1186.

[157] J. Jiang, Z. Li, X. He, Y. Hu, F. Li, P. Huang, C. Wang, Novel skutterudite CoP_3–based asymmetric supercapacitor with super high energy density, Small 16 (2020) 2000180.

[158] M. Kong, Z. Wang, W. Wang, M. Ma, D. Liu, S. Hao, R. Kong, G. Du, A.M. Asiri, Y. Yao, X. Sun, NiCoP nanoarray: a superior pseudocapacitor electrode with high areal capacitance, Chemistry 23 (2017) 4435–4441.

[159] X. Zhang, D. Su, A. Wu, H. Yan, X. Wang, D. Wang, L. Wang, C. Tian, L. Sun, H. Fu, Porous NiCoP nanowalls as promising electrode with high-area and mass capacitance for supercapacitors, Sci. China Mater. 62 (2019) 1115–1126.

[160] Z. Wang, H. Wang, S. Ji, X. Wang, P. Zhou, S. Huo, V. Linkov, R. Wang, Hollow-structured NiCoP nanorods as high-performance electrodes for asymmetric supercapacitors, Mater. Des. 193 (2020) 108807.

[161] M. Gao, W.-K. Wang, X. Zhang, J. Jiang, H.-Q. Yu, Fabrication of metallic nickel–cobalt phosphide hollow microspheres for high-rate supercapacitors, J. Phys. Chem. C. 122 (2018) 25174–25182.

[162] B. Zhang, Y.H. Lui, H. Ni, S. Hu, Bimetallic $(Fe_xNi_{1-x})_2P$ nanoarrays as exceptionally efficient electrocatalysts for oxygen evolution in alkaline and neutral media, Nano Energy 38 (2017) 553–560.

[163] J. Yang, Z. Wang, Z. Wang, J. Zhang, Q. Zhang, P.P. Shum, L. Wei, All-metal phosphide electrodes for high-performance quasi-solid-state fiber-shaped aqueous rechargeable Ni-Fe Batteries, ACS Appl. Mater. Interfaces 12 (2020) 12801–12808.

[164] Q. Zong, H. Yang, Q. Wang, Q. Zhang, J. Xu, Y. Zhu, H. Wang, H. Wang, F. Zhang, Q. Shen, $NiCo_2O_4$/NiCoP nanoflake-nanowire arrays: a homogeneous hetero-

structure for high performance asymmetric hybrid supercapacitors, Dalton Trans. 47 (2018) 16320–16328.
[165] B. Li, H.C. Zeng, Architecture and preparation of hollow catalytic devices, Adv. Mater. 31 (2019) 1801104.
[166] Y. Yang, F. Güder, M. Zacharias, Diffusion-induced void evolution in core–shell nanowires: Elaborated view on the nanoscale kirkendall effect, Isr. J. Chem. 50 (2010) 439–448.
[167] Z. Wang, L. Pan, H. Hu, S. Zhao, Modified Kirkendall effect for fabrication of magnetic nanotubes, Chem. Commun. 46 (2020) 1899–1901.
[168] Y. Zhang, L. Sun, L. Zhang, X. Li, J. Gu, H. Si, L. Wu, Y. Shi, C. Sun, Y. Zhang, Highly porous oxygen-doped NiCoP immobilized in reduced graphene oxide for supercapacitive energy storage, Compos. Part B: Eng. 182 (2020) 107611.
[169] J. Lin, Z. Zhong, H. Wang, X. Zheng, Y. Wang, J. Qi, J. Cao, W. Fei, Y. Huang, J. Feng, Rational constructing free-standing Se doped nickel-cobalt sulfides nanotubes as battery-type electrode for high-performance supercapattery, J. Power Sources 407 (2018) 6–13.
[170] X. Gao, X. Liu, D. Wu, B. Qian, Z. Kou, Z. Pan, Y. Pang, L. Miao, J. Wang, Significant role of Al in ternary layered double hydroxides for enhancing electrochemical performance of flexible asymmetric supercapacitor, Adv. Funct. Mater. 29 (2019) 1903879.
[171] A.M. Elshahawy, C. Guan, X. Li, H. Zhang, Y. Hu, H. Wu, S.J. Pennycook, J. Wang, Sulfur-doped cobalt phosphide nanotube arrays for highly stable hybrid supercapacitor, Nano Energy 39 (2017) 162–171.
[172] X. Lei, S. Ge, Y. Tan, J. Li, Z. Wang, P. Liu, C. Feng, B. Xiang, Bimetallic phosphosulfide Zn–Ni–P–S nanosheets as binder-free electrodes for aqueous asymmetric supercapacitors with impressive performance, J. Mater. Chem. A 7 (2019) 24908–24918.
[173] J. Balamurugan, T.T. Nguyen, V. Aravindan, N.H. Kim, S.H. Lee, J.H. Lee, All ternary metal selenide nanostructures for high energy flexible charge storage devices, Nano Energy 65 (2019) 103999.
[174] C. Mu, J. Song, Y. Zhang, L. Liu, B. Wang, J. Xiang, Three dimensional bimetallic phosphides nanoneedle arrays as electrode materials for symmetric all-solid-state supercapacitor, J. Alloys Compd. 787 (2019) 618–624.
[175] M. Zhou, Y. Xu, Y. Lei, Heterogeneous nanostructure array for electrochemical energy conversion and storage, Nano Today 20 (2018) 33–57.
[176] M. Zhi, C. Xiang, J. Li, M. Li, N. Wu, Nanostructured carbon-metal oxide composite electrodes for supercapacitors: a review, Nanoscale 5 (2013) 72–88.
[177] J. Gu, L. Sun, Y. Zhang, Q. Zhang, X. Li, H. Si, Y. Shi, C. Sun, Y. Gong, Y. Zhang, MOF-derived Ni-doped CoP@C grown on CNTs for high-performance supercapacitors, Chem. Eng. J. 385 (2020) 123454.
[178] Y. Shao, Y. Zhao, H. Li, C. Xu, Three-dimensional hierarchical Ni$_x$Co$_{1-x}$O/Ni$_y$Co$_{2-y}$P@C hybrids on nickel foam for excellent supercapacitors, ACS Appl. Mater. Interfaces 8 (2016) 35368–35376.
[179] D. Kong, C. Cheng, Y. Wang, J.I. Wong, Y. Yang, H.Y. Yang, Three-dimensional Co$_3$O$_4$@C@Ni$_3$S$_2$ sandwich-structured nanoneedle arrays: towards high-performance flexible all-solid-state asymmetric supercapacitors, J. Mater. Chem. A 3 (2015) 16150–16161.
[180] J. Lin, Y. Liu, Y. Wang, H. Jia, S. Chen, J. Qi, C. Qu, J. Cao, W. Fei, J. Feng, Rational construction of nickel cobalt sulfide nanoflakes on CoO nanosheets with the help of carbon layer as the battery-like electrode for supercapacitors, J. Power Sources 362 (2017) 64–72.
[181] Q. Zong, H. Yang, Q. Wang, Q. Zhang, Y. Zhu, H. Wang, Q. Shen, Three-dimensional coral-like NiCoP@C@Ni(OH)$_2$ core-shell nanoarrays as battery-type electrodes to enhance cycle stability and energy density for hybrid supercapacitors, Chem. Eng. J. 361 (2019) 1–11.
[182] P. Wu, S. Cheng, M. Yao, L. Yang, Y. Zhu, P. Liu, O. Xing, J. Zhou, M. Wang, H. Luo, M. Liu, A low-cost, self-standing NiCo$_2$O$_4$@CNT/CNT multilayer electrode for flexible asymmetric solid-state supercapacitors, Adv. Funct. Mater. 27 (2017) 1702160.
[183] G. Zhao, Y. Tang, G. Wan, X. Xu, X. Zhou, M. Zhou, C. Hao, S. Deng, G. Wang, High-performance and flexible all-solid-state hybrid supercapacitor constructed by NiCoP/CNT and N-doped carbon coated CNT nanoarrays, J. Colloid Interface Sci. 572 (2020) 151–159.
[184] C.Y. Foo, A. Sumboja, D.J.H. Tan, J. Wang, P.S. Lee, Flexible and highly scalable V$_2$O$_5$-rGO electrodes in an organic electrolyte for supercapacitor devices, Adv. Energy Mater. 4 (2014) 1400236.
[185] C. An, Y. Wang, L. Li, F. Qiu, Y. Xu, C. Xu, Y. Huang, L.J.H. Yuan, Effects of highly crumpled graphene nanosheets on the electrochemical performances of pseudocapacitor electrode materials, Electrochim. Acta 133 (2014) 180–187.
[186] S.M.S.P. Gnanasekaran G., P. Pazhamalai, S. Sahoo, M.M. Hossain, R.M. Bhattarai, S.-J. Kim, Y.S. Mok, Hierarchically porous nanostructured nickel phosphide with carbon particles embedded by dielectric barrier discharge plasma deposition as a binder-free electrode for hybrid supercapacitors, ACS Sustain. Chem. Eng. 7 (2019) 14805–14814.
[187] N. Jabeen, Q. Xia, M. Yang, H. Xia, Unique core-shell nanorod arrays with polyaniline deposited into mesoporous NiCo$_2$O$_4$ support for high-performance supercapacitor electrodes, ACS Appl. Mater. Interfaces 8 (2016) 6093–6100.
[188] Q. Wang, J. Wang, H. Wang, J. Zhan, Y. Zhu, Q. Zhang, Q. Shen, H. Yang, TiO$_2$-C nanowire arrays@polyaniline core-shell nanostructures on carbon cloth for high performance supercapacitors, Appl. Surf. Sci. 493 (2019) 1125–1133.
[189] J. Luo, Z. Zheng, A. Kumamoto, W.I. Unah, S. Yan, Y.H. Ikuhara, X. Xiang, X. Zu, W. Zhou, PEDOT coated iron phosphide nanorod arrays as high-performance supercapacitor negative electrodes, Chem. Commun. (Camb.) 54 (2018) 794–797.
[190] D. Zhao, H. Liu, X. Wu, Bi-interface induced multi-active MCo$_2$O$_4$@MCo$_2$S$_4$@PPy (M=Ni, Zn) sandwich structure for energy storage and electrocatalysis, Nano Energy 57 (2019) 363–370.
[191] S. Liu, Y. Chen, J. Ren, Y. Wang, W. Wei, An effective interaction in polypyrrole/nickel phosphide (PPy/Ni$_2$P) for high-performance supercapacitor, J. Solid State Electr. 23 (2019) 3409–3418.
[192] J. Lin, X. Zheng, Y. Wang, H. Liang, H. Jia, S. Chen, J. Qi, J. Cao, W. Fei, J. Feng, Rational construction of core–shell Ni$_3$S$_2$@Ni(OH)$_2$ nanostructures as battery-like electrodes for supercapacitors, Inorg. Chem. Front. 5 (2018) 1985–1991.
[193] F. Chen, H. Wang, S. Ji, V. Linkov, R. Wang, Core-shell structured Ni$_3$S$_2$@Co(OH)$_2$ nano-wires grown on Ni foam as binder-free electrode for asymmetric supercapacitors, Chem. Eng. J. 345 (2018) 48–57.
[194] H. Wang, Y. Zhu, Q. Zong, Q. Wang, H. Yang, Q. Zhang, Hierarchical NiCoP/Co(OH)$_2$ nanoarrays for high-performance asymmetric hybrid supercapacitors, Electrochim. Acta 321 (2019) 134746.
[195] J. Wen, S. Li, T. Chen, B. Li, L. Xiong, Y. Guo, G. Fang, Porous nanosheet network architecture of CoP@Ni(OH)$_2$ composites for high performance supercapacitors, Electrochim. Acta 258 (2017) 266–273.
[196] S. Liu, H. Zhu, B. Zhang, G. Li, H. Zhu, Y. Ren, H. Geng, Y. Yang, Q. Liu, C.C. Li, Tuning the kinetics of zinc-ion insertion/extraction in V$_2$O$_5$ by in situ polyaniline intercalation enables improved aqueous zinc-ion storage performance, Adv. Mater. 32 (2020) 2001113.
[197] S. Gao, Y. Sun, F. Lei, L. Liang, J. Liu, W. Bi, B. Pan, Y. Xie, Ultrahigh energy density realized by a single-layer β-Co(OH)$_2$ all-solid-state asymmetric supercapacitor, Angew. Chem. Int Ed. Engl. 53 (2014) 12789–12793.
[198] H. Jia, Z. Wang, X. Zheng, J. Lin, H. Liang, Y. Cai, J. Qi, J. Cao, J. Feng, W. Fei, Interlaced Ni-Co LDH nanosheets wrapped Co$_9$S$_8$ nanotube with hierarchical structure toward high performance supercapacitors, Chem. Eng. J. 351 (2018) 348–355.
[199] X. He, R. Li, J. Liu, Q. Liu, R. chen, D. Song, J. Wang, Hierarchical FeCo$_2$O$_4$@NiCo layered double hydroxide core/shell nanowires for high performance flexible all-solid-state asymmetric supercapacitors, Chem. Eng. J. 334 (2018) 1573–1583.
[200] Y. Zhao, X. He, R. Chen, Q. Liu, J. Liu, J. Yu, J. Li, H. Zhang, H. Dong, M. Zhang, J. Wang, A flexible all-solid-state asymmetric supercapacitors based on hierarchical carbon cloth@CoMoO$_4$@NiCo layered double hydroxide core-shell heterostructures, Chem. Eng. J. 352 (2018) 29–38.
[201] Q. Yang, Y. Liu, L. Xiao, M. Yan, H. Bai, F. Zhu, Y. Lei, W. Shi, Self-templated transformation of MOFs into layered double hydroxide nanoarrays with selectively formed Co$_9$S$_8$ for high-performance asymmetric supercapacitors, Chem. Eng. J. 354 (2018) 716–726.
[202] L. Wan, D. Chen, J. Liu, Y. Zhang, J. Chen, M. Xie, C. Du, Construction of FeNiP@CoNi-layered double hydroxide hybrid nanosheets on carbon cloth for high energy asymmetric supercapacitors, J. Power Sources 465 (2020) 228293.
[203] H. Liang, J. Lin, H. Jia, S. Chen, J. Qi, J. Cao, T. Lin, W. Fei, J. Feng, Hierarchical NiCo-LDH/NiCoP@NiMn-LDH hybrid electrodes on carbon cloth for excellent supercapacitors, J. Mater. Chem. A 6 (2018) 15040–15046.
[204] H. Zhang, X. Li, A. Hähnel, V. Naumann, C. Lin, S. Azimi, S.L. Schweizer, A.W. Maijenburg, R.B. Wehrspohn, Bifunctional heterostructure assembly of NiFe LDH nanosheets on NiCoP nanowires for highly efficient and stable overall water splitting, Adv. Funct. Mater. 28 (2018) 1706847.
[205] S. Wang, Z. Huang, R. Li, X. Zheng, F. Lu, T. He, Template-assisted synthesis of NiP@CoAl-LDH nanotube arrays with superior electrochemical performance for supercapacitors, Electrochim. Acta 204 (2016) 160–168.
[206] S. Kandula, K.R. Shrestha, G. Rajeshkhanna, N.H. Kim, J.H. Lee, Kirkendall growth and ostwald ripening induced hierarchical morphology of Ni-Co LDH/MMoS$_x$ (M = Co, Ni, and Zn) heteronanostructures as advanced electrode materials for asymmetric solid-state supercapacitors, ACS Appl. Mater. Interfaces 11 (2019) 11555–11567.
[207] F. Yu, Z. Chang, X. Yuan, F. Wang, Y. Zhu, L. Fu, Y. Chen, H. Wang, Y. Wu, W. Li, Ultrathin NiCo$_2$S$_4$@graphene with a core–shell structure as a high performance positive electrode for hybrid supercapacitors, J. Mater. Chem. A 6 (2018) 5856–5861.
[208] Y. Ouyang, H. Ye, X. Xia, X. Jiao, G. Li, S. Mutahir, L. Wang, D. Mandler, W. Lei, Q. Hao, Hierarchical electrodes of NiCo$_2$S$_4$ nanosheets-anchored sulfur-doped Co$_3$O$_4$ nanoneedles with advanced performance for battery-supercapacitor hybrid devices, J. Mater. Chem. A 7 (2019) 3228–3237.
[209] L. Wan, C. He, D. Chen, J. Liu, Y. Zhang, C. Du, M. Xie, J. Chen, In situ grown NiFeP@NiCo$_2$S$_4$ nanosheet arrays on carbon cloth for asymmetric supercapacitors, Chem. Eng. J. 399 (2020) 125778.
[210] L. Naderi, S. Shahrokhian, Nickel vanadium sulfide grown on nickel copper phosphide dendrites/Cu fibers for fabrication of all-solid-state wire-type micro-supercapacitors, Chem. Eng. J. 392 (2020) 124880.
[211] X. Gao, P. Wang, Z. Pan, J.P. Claverie, J. Wang, Recent progress in two-dimensional layered double hydroxides and their derivatives for supercapacitors, ChemSusChem 13 (2020) 1226–1254.

[212] M. Yousaf, Y. Wang, Y. Chen, Z. Wang, A. Firdous, Z. Ali, N. Mahmood, R. Zou, S. Guo, R.P.S. Han, A 3D trilayered CNT/$MoSe_2$/C heterostructure with an expanded MoSe2 interlayer spacing for an efficient sodium storage, Adv. Energy Mater. 9 (2019) 1900567.

[213] X. Gao, L. Yin, L. Zhang, Y. Zhao, B. Zhang, Decoration of NiCoP nanowires with interlayer-expanded few-layer $MoSe_2$ nanosheets: a novel electrode material for asymmetric supercapacitors, Chem. Eng. J. 395 (2020) 125058.

[214] Z. Huang, X. Li, X. Xiang, T. Gao, Y. Zhang, D. Xiao, Porous NiCoP in situ grown on Ni foam using molten-salt electrodeposition for asymmetric supercapacitors, J. Mater. Chem. A 6 (2018) 23746–23756.

[215] K. Chi, Z. Zhang, Q. Lv, C. Xie, J. Xiao, F. Xiao, S. Wang, Well-ordered oxygen-deficient $CoMoO_4$ and Fe_2O_3 nanoplate arrays on 3D graphene foam: toward flexible asymmetric supercapacitors with enhanced capacitive properties, ACS Appl. Mater. Interfaces 9 (2017) 6044–6053.

[216] Z. Chen, W. Ren, L. Gao, B. Liu, S. Pei, H.M. Cheng, Three-dimensional flexible and conductive interconnected graphene networks grown by chemical vapour deposition, Nat. Mater. 10 (2011) 424–428.

[217] F. Cui, Y. Huang, L. Xu, Y. Zhao, J. Lian, J. Bao, H. Li, Rational construction of a 3D hierarchical $NiCo_2O_4$/PANI/MF composite foam as a high-performance electrode for asymmetric supercapacitors, Chem. Commun. 54 (2018) 4160–4163.